Nanoparticle-Enabled *In Vivo* Photoacoustic Molecular Imaging of Cancer

by

Joel Tan

A dissertation submitted in partial fulfillment
of the requirements for the degree of
Doctor of Philosophy
(Biomedical Engineering)
in The University of Michigan
2020

Doctoral Committee:

Professor Xueding Wang, Chair
Professor Cheri Deng
Professor Raoul Kopelman
Assistant Professor Guan Xu

Joel Tan

tanjoel@umich.edu

ORCID iD: 0000-0002-9091-5217

DEDICATION

This dissertation is dedicated to my friends and family, whose support has made completion of this thesis possible.

ACKNOWLEDGMENTS

I would like to express my deepest gratitude to my graduate supervisor, Dr. Xueding Wang, for his patience and wisdom in guiding me throughout my PhD. Your supervision has given me an in-depth understanding on research and an appreciation for the importance of collaborations to achieve great breakthroughs in research. A special thank you as well to my committee members, Dr. Raoul Kopelman, Dr. Cheri Deng, and Dr. Guan Xu for your support, feedback, and advice throughout the years. Your guidance has been invaluable in helping me complete my PhD degree.

I would also like to thank my fellow lab members for all the help and knowledge that you have given to me throughout my time working here. Since the beginning, you have been supportive as I started from an inexperienced researcher into the scientist that I am today. To my close collaborators, Jeff, Chang, and Misha, thank you for the opportunity of working together and for putting up with me all these years. I have thoroughly enjoyed working with you and having the chance to learn about a different side of science.

To my family and friends, thank you for always being supportive of me through my ups and downs in pursuing this PhD. To my parents, for being willing to send me to an international country for my undergraduate degree, which eventually led directly to this PhD opportunity. To my brothers, for all their advice and help throughout the years. And finally, to my friends, for all your emotional support and for making my time in Ann Arbor an enjoyable one.

TABLE OF CONTENTS

LIST OF FIGURES

LIST OF ABBREVIATIONS

BOLD	Blood oxygenation level dependent
CFZ-HCL NP	Clofazimine hydrochloride nanoparticle
CNR	Contrast-to-noise ratio
DRE	Digital rectal exam
EPR	Enhanced permeability and retention
GNP	Gold nanoparticle
Hb	Deoxyhemoglobin
HbO_2	Oxyhemoglobin
HE	Hematoxylin and eosin
ICG	Indocyanine green
ICP-MS	Inductively coupled plasma mass spectrometry
ISC	Intersystem crossing
IV	Intravenous
K^+	Potassium ion
MBNP	Methylene blue nanoparticle
MPE	Maximum permissible exposure
MRI	Magnetic resonance imaging
O_2	Oxygen
PA	Photoacoustic

PACI	Photoacoustic chemical imaging
PBS	Phosphate buffered saline
PSA	Prostate specific antigen
ROI	Region of interest
SDKNP	Solvatochromic dye potassium nanoparticle
SNR	Signal-to-noise ratio
SO_2	Blood oxygenation
SU	Spectral unmixing
TAM	Tumor-associated macrophages
TAS	Transient absorption spectroscopy
TEM	Transmission electron microscopy
THb	Total hemoglobin
TME	Tumor microenvironment
TRAMP	Transgenic adenocarcinoma of the mouse prostate
TRUS	Transrectal ultrasound
TTD	Transient triplet differential
US	Ultrasound

ABSTRACT

Photoacoustic (PA) imaging is an emerging biomedical imaging modality that combines optical and ultrasound imaging technologies. PA imaging relies on the absorption of electromagnetic energy (usually in the form of visible or near-infrared light) leading to the generation of acoustic waves by thermoelastic expansion, which can be detected with an ultrasound detector. PA imaging can be used to detect endogenous chromophores such as deoxyhemoglobin and oxyhemoglobin, or can be used together with external nanosensors for added functionality. The former is used to measure things like blood oxygenation, while the latter opens up many possibilities for PA imaging, limited only to the availability of optical nanosensors. In this dissertation, I employ the use of PA nanosensors for contrast enhancement and molecular imaging in *in vivo* small animal cancer models.

In the first section, I introduce a novel PA background reduction technique called the transient triplet differential (TTD) method. The TTD method exploits the fact that phosphorescent dyes possess a triplet state with a unique red-shifted absorption wavelength, distinct from its ordinary singlet state absorption profile. By pumping these dyes into the triplet state and comparing the signal to the unpumped dyes, a differential signal can be obtained which solely originates from these dyes. Since intrinsic chromophores of biological tissue are not able to undergo intersystem crossing and enter

the triplet state, the TTD method can facilitate “true” background free molecular imaging by excluding the signals from every other chromophore outside the phosphorescent dye. Here, I demonstrate up to an order of magnitude better sensitivity of the TTD method compared to other existing contrast enhancement techniques in both *in vitro* experiments and *in vivo* cancer models.

In the second section, I explore the use of a nanoparticle formulation of a repurposed FDA-approved drug called clofazimine for diagnosis of prostate cancer. Clofazimine nanoparticles have a high optical absorbance at 495 nm and has been known to specifically accumulate in macrophages as they form stable crystal-like inclusions once they are uptaken by macrophages. Due to the presence of tumor associated macrophages, it is expected that clofazimine would accumulate in much higher quantities in the cancerous prostate compared to normal prostates. Here, I show that there was indeed a significantly higher accumulation of clofazimine nanoparticles in cancerous prostates compared to normal prostates in a transgenic mouse model, which was detectable both using histology and *ex vivo* PA imaging.

In the third and final section, I explore the use of a potassium (K^+) nanosensor together with PA imaging in measuring the *in vivo* K^+ distribution in the tumor microenvironment (TME). K^+ is the most abundant ion in the body and has recently been shown to be at a significantly higher concentration in the tumor. The reported 5-10 fold elevation (25-50 mM compared to 5mM) in the tumor has been shown to inhibit immune cell efficacy, and thus immunotherapy. Despite the abundance and importance of K^+ in the body, few ways exist to measure it *in vivo*. In this study, a solvatochromic dye K^+ nanoparticle (SDKNP) was used together with PA imaging to quantitatively measure the in vivo distribution of K^+

in the TME. Significantly elevated K^+ levels were found in the TME, with an average concentration of approximately 29 mM, matching the values found by the previous study. The results were then verified using mass spectrometry.

CHAPTER 1

Introduction

Photoacoustic (PA) imaging is a non-ionizing imaging technology that relies on the generation of acoustic waves from the absorption of electromagnetic energy due to the thermoelastic effect. Traditional photoacoustic imaging is usually performed using a combination of a nanosecond pulsed laser (to generate the electromagnetic energy) and an ultrasound transducer (to measure the thermoelastic waves that are generated). The nanosecond pulse width of the pulsed laser is important to satisfy the thermal and stress confinement parameters, which ensure that there is no significant heat diffusion or stress transmission away from the point of absorption [3]. Satisfying these two requirements ensure the efficient generation of PA signals. While other forms of electromagnetic energy can be used, visible and near-infrared light (550 nm - 900 nm) are the most commonly used optical wavelengths for PA imaging [4]. Excitation using the nanosecond light pulses in biological tissues generally results in a broadband acoustic signal (approximately tens of megahertz) with a low amplitude (< 10kPa) that can be picked up by the ultrasound transducer [4]. A schematic of a typical PA imaging setup is shown in Figure 1.1.

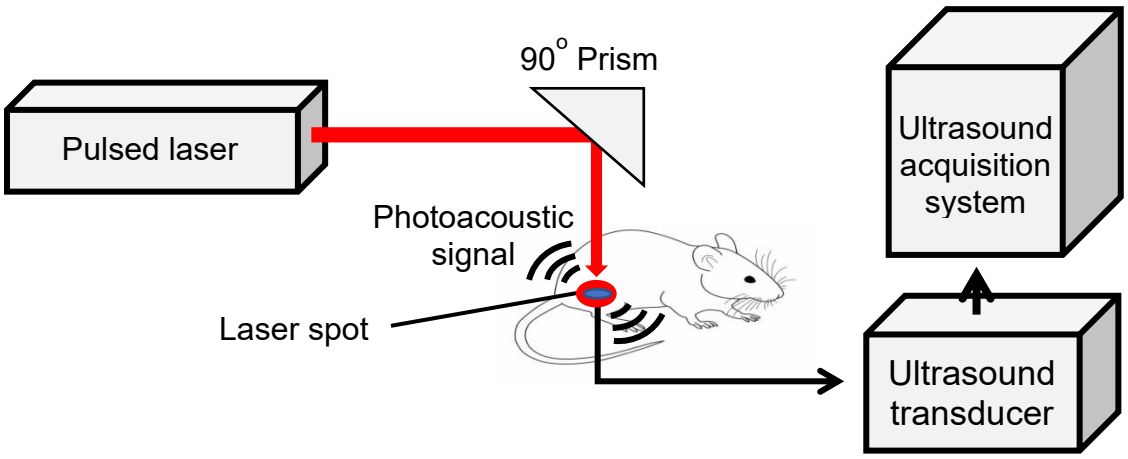

Figure 1.1 Typical photoacoustic imaging setup. An acoustic coupling medium (such as water or ultrasound gel) is typically used between the ultrasound transducer and the sample being imaged to ensure good acoustic coupling.

Traditional optical methods such as fluorescence, two-photon, and optical coherence tomography all require measuring the backscattered photons (or transmitted photons), which limits their *in vivo* imaging depth to several millimeters due to strong optical scattering in tissue. PA imaging, on the other hand, has been shown to be able to image structures/molecules centimeters deep in *in vivo* tissue [5]. This is due to PA imaging measuring the acoustic signal output (not photons), which has orders of magnitude less scattering than visible/near-infrared light. Additionally, PA imaging does not rely on the ballistic regime of light (with notable exception of optically-focused PA imaging), further increasing its imaging depth capabilities [4]. Hence, PA imaging has significantly more potential as an *in vivo* imaging tool than traditional optical approaches. PA imaging is said to provide optical contrast at the diffraction-limited high spatial resolution of ultrasound, with far superior imaging depths than other optical imaging technologies [6].

The magnitude of the PA signal that is generated is directly dependent on the absorption of the material and can be modelled with the following equation:

$$PA_\lambda = \gamma \varepsilon_\lambda \phi_\lambda C \qquad \textbf{(1.1)}$$

where λ is the wavelength in nm, γ is the Grüneisen parameter, ε is the extinction coefficient, Φ is the optical fluence, and C is the concentration of the chromophore (in the case of visible light absorption). The Grüneisen parameter is a dimensionless parameter that is affected by temperature and can usually be ignored unless significant temperature changes are expected. The extinction (or absorption) coefficient is a parameter that is unique to each chromophore, or light-absorbing region of a molecule. Optical fluence reflects the magnitude of the excitation laser. Concentration reflects the quantity of the molecule that is generating the PA signal. Each molecule possesses a unique absorption spectrum, which is the basis on which methods like spectral unmixing, and subsequently blood oxygenation measurements are made. An example of the absorption spectra of blood (deoxyhemoglobin and oxyhemoglobin) is shown in Figure 1.2, with blood being one of the most dominant signals in biological tissue. This will be discussed in detail further on in this thesis.

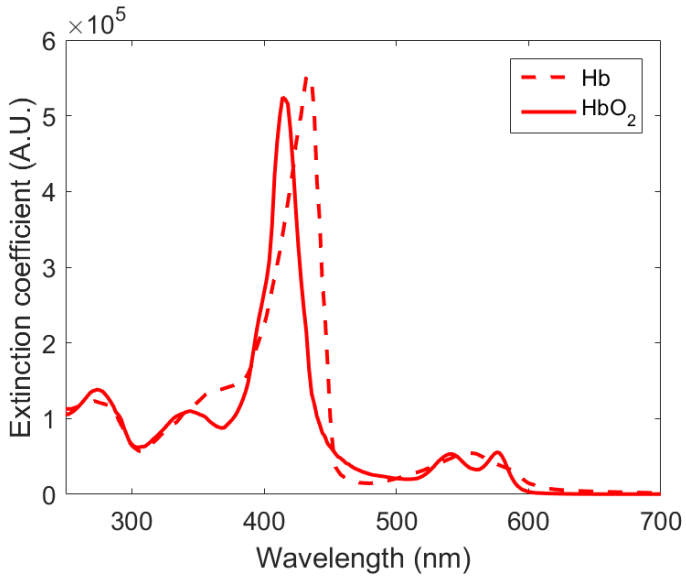

Figure 1.2 Absorption spectra of deoxyhemoglobin (Hb) and oxyhemoglobin (HbO_2). Most PA imaging is conducted in the "optical imaging window" from 500 – 900 nm where the absorption of blood is low, allowing for better imaging depth *in vivo*.

Photoacoustic imaging, in and of itself, is sensitive to several endogenous biological chromophores, such as deoxyhemoglobin, oxyhemoglobin, and melanin. The former two form an important application in photoacoustic imaging, where many studies have looked at quantifying blood oxygenation levels *in vivo*, with emphasis on both tumor and brain oxygenation measurements [6-11]. Blood oxygenation is an important indicator for both measuring tumor hypoxia (and can potentially be used as an indicator for tumor response to treatment), as well as measuring functional brain information, similar to that conducted by BOLD (blood oxygenation level dependent) MRI [12]. Blood oxygenation measurements are performed by exploiting the different absorption spectra of deoxyhemoglobin and oxyhemoglobin. By making at least two measurements at two different wavelengths, a ratio of the PA signal can be obtained which gives an indication of the blood oxygenation level.

That being said, endogenous chromophore information can only go so far. As is typical to other imaging modalities as well, contrast agents and functional nanoparticles have been used in PA imaging to broaden its potential applications [13-15]. Contrast agents such as indocyanine green (ICG), methylene blue, and gold nanoparticles have been used to increase the signal-to-noise ratio (SNR) of PA imaging. These contrast agents are usually localized or targeted to a cell/tissue/organ of interest (such as sentinel lymph nodes, tumors, targeted antigens on cells), which provide enhancement of the PA signal of the target of interest [14,15]. Alternatively, in addition to providing contrast, some of these nanoparticles have been used to provide molecular information *in vivo* [16,17], which forms a significant portion of this thesis research. For example, nanoparticle-enhanced PA

imaging has been used in the monitoring of lithium treatments for bipolar disorder [18], measuring of tissue oxygenation using a lifetime-based approach [17,19-22], and measuring of tumor pH [16].

In this thesis, I have employed the use of nanoparticles in PA imaging to achieve two broad purposes: (1) For contrast enhancement in cancer detection/diagnosis, and (2) For quantitative measurements of chemical parameters in the tumor microenvironment. This thesis is broken down into several chapters that will highlight my research into this field of nanoparticle-enabled photoacoustic imaging.

Chapter 2 enters a brief discussion on multi-wavelength (spectral) unmixing and its role in nanoparticle-enhanced photoacoustic imaging. Here, I enter a brief discussion into the mathematical equations governing multi-wavelength unmixing as well.

Chapter 3 discusses my development of a transient triplet differential method for background removal in photoacoustic imaging using phosphorescence-capable dyes. This technique showed significantly better signal-to-noise ratios and numerous other advantages over multi-wavelength unmixing. The technique was also demonstrated *in vivo* in a mouse tumor model to show its potential applications as a contrast enhancement technique in cancer research.

Chapter 4 discusses my research into using an FDA-approved drug called clofazimine for prostate cancer diagnosis. Clofazimine is a lipophilic drug that specifically accumulates in macrophages. We hypothesized that due to tumor associated macrophages, clofazimine will accumulate in larger quantities in cancerous prostates than in normal prostates. To demonstrate its potential application as a prostate cancer diagnostic

contrast agent, we showed that there was indeed a higher accumulation in the cancerous prostate than in a normal prostate, which was detectable using both histology and PA imaging in an *ex vivo* setting.

Chapter 5 discusses my contributions to the field of photoacoustic chemical imaging, specifically in that of *in vivo* potassium imaging. Photoacoustic chemical imaging focuses on the use of chemical nanosensors together with PA imaging for the purposes of *in vivo* measurements of chemical properties. Here, we demonstrated the ability to make quantitative measurements of potassium in an *in vivo* mouse tumor through the use of multi-wavelength unmixing.

The dissertation is then ended with a summary of my contributions in the field of nanoparticle-enabled PA cancer imaging, and proposes some future steps that could be taken in this field of study.

CHAPTER 2

Multi-Wavelength Unmixing

In this chapter, I will be taking a slight detour to explain an essential algorithm that is used extensively throughout my research. This method, known as multi-wavelength unmixing or spectral unmixing, is used to isolate the contributions of each identified chromophore from the PA signal as a whole [23,24]. This method is widely used for most forms of quantitative PA imaging, including that of blood oxygenation measurements. Multi-wavelength unmixing relies on an extension of equation 1.1, where instead of a single chromophore, we extend the contribution to the PA signal to take into account all the chromophores of interest. The extended equation is shown in equation 2.1.

$$PA_\lambda = \sum_{i=0}^{n} \gamma_i \varepsilon_{i,\lambda} \phi_\lambda C_i \qquad \textbf{(2.1)}$$

Making use of the difference in absorption spectra of each chromophore, equation 2.1 can be used to determine the concentrations of each of the chromophores of interest. An example of this is shown in equation 2.2, where we assume the PA signal to arise from 3 chromophores of interest, specifically Hb, HbO_2, and a contrast agent "x".

$$PA_\lambda = \gamma_{Hb} \varepsilon_{Hb,\lambda} \phi_\lambda C_{Hb} + \gamma_{HbO2} \varepsilon_{HbO2,\lambda} \phi_\lambda C_{HbO2} + \gamma_x \varepsilon_{x,\lambda} \phi_\lambda C_x \qquad \textbf{(2.2)}$$

To simplify this equation, we make the assumption that the Grüneisen parameter, γ, is constant and that optical fluence, Φ is also constant. The former assumption is generally

a good assumption assuming that the temperature of the sample remains constant. The later assumption, however, will affect the accuracy of the multi-wavelength unmixing with increasing errors at increasing depths due to the wavelength-dependent fluence attenuation of tissue. That being said, fluence compensation models are complex [25,26] and is outside the scope of this thesis. It has been shown, however, that within shorter imaging depths (< 1cm), such as within a subcutaneous tumor, the error is of sufficiently low magnitude, allowing for quantitative imaging [16]. Simplifying equation 2.2 based on these assumptions then yields equation 2.3.

$$PA_{\lambda} = k(\varepsilon_{Hb,\lambda}C_{Hb} + \varepsilon_{HbO2,\lambda}C_{HbO2} + \varepsilon_{x,\lambda}C_{x}) \qquad \textbf{(2.3)}$$

Here, k is the constant that includes the Grüneisen parameter and optical fluence. Based on equation 2.3, the extinction coefficients of Hb, HbO_2, and contrast agent x are all known and measurable quantities, leaving only the concentrations of the 3 chromophores as unknowns. By making at least 3 separate measurements at different wavelengths, the following matrix can be obtained.

$$\begin{bmatrix} PA_{\lambda 1} \\ PA_{\lambda 2} \\ PA_{\lambda 3} \end{bmatrix} = k \begin{bmatrix} \varepsilon_{Hb,\lambda 1} & \varepsilon_{HbO2,\lambda 1} & \varepsilon_{x,\lambda 1} \\ \varepsilon_{Hb,\lambda 2} & \varepsilon_{HbO2,\lambda 2} & \varepsilon_{x,\lambda 2} \\ \varepsilon_{Hb,\lambda 3} & \varepsilon_{HbO2,\lambda 3} & \varepsilon_{x,\lambda 3} \end{bmatrix} \begin{bmatrix} C_{Hb} \\ C_{HbO2} \\ C_{x} \end{bmatrix} \qquad \textbf{(2.4)}$$

The PA signals are the measured signals, while the matrix with the extinction coefficients are all known. This equation can then be rearranged to obtain the concentrations of each of the chromophores (relative concentrations as they are affected by the constant k).

$$\mathrm{k}\begin{bmatrix} C_{Hb} \\ C_{HbO2} \\ C_{x} \end{bmatrix} = \begin{bmatrix} \varepsilon_{Hb,\lambda 1} & \varepsilon_{HbO2,\lambda 1} & \varepsilon_{x,\lambda 1} \\ \varepsilon_{Hb,\lambda 2} & \varepsilon_{HbO2,\lambda 2} & \varepsilon_{x,\lambda 2} \\ \varepsilon_{Hb,\lambda 3} & \varepsilon_{HbO2,\lambda 3} & \varepsilon_{x,\lambda 3} \end{bmatrix}^{-1} \begin{bmatrix} PA_{\lambda 1} \\ PA_{\lambda 2} \\ PA_{\lambda 3} \end{bmatrix} \qquad \textbf{(2.5)}$$

Using these concentration values, determining things like quantitative blood oxygenation measurements are then possible, by taking the ratios of the unmixed concentrations. For example, a typical blood oxygenation (SO_2) measurement is as follows.

$$\%SO_2 = \frac{kC_{HbO2}}{kC_{HbO2}+kC_{Hb}}.100\% \qquad \textbf{(2.6)}$$

$$\%SO_2 = \frac{C_{HbO2}}{C_{HbO2}+C_{Hb}}.100\% \qquad \textbf{(2.7)}$$

As can be seen in equation 2.7, the constant k is then eliminated from equation 2.6, giving a quantitative measurement. It is of note that this is only possible with the assumptions on the Grüneisen parameter and optical fluence made earlier. This technique can then be extended for any number of chromophores, as long as an additional wavelength measurement is made for each additional unknown in equation 2.3**.** Notably, it is often the case that extra wavelength measurements (above what is strictly needed) are made to improve the accuracy of the multi-wavelength unmixing algorithm [23,27,28].

CHAPTER 3

Transient Triplet Differential Imaging for Background-Free Photoacoustic Imaging

3.1 Brief Foreword

This research work represents a method for PA contrast enhancement that relies on the use of phosphorescence dyes. The results have been published in the following article

"Tan, J. W. Y.; Lee, C. H.; Kopelman, R.; Wang, X., Transient Triplet Differential (TTD) Method for Background Free Photoacoustic Imaging. *Scientific Reports* **2018,** *8*, 9290."

and most of the following text and figures are quoted verbatim from the above-mentioned publication.

3.2 Abstract

With the capability of presenting endogenous tissue contrast or exogenous contrast agents in deep biological samples at high spatial resolution, photoacoustic (PA) imaging has shown significant potential for many preclinical and clinical applications. However, due to strong background signals from various intrinsic chromophores in biological tissue, such as hemoglobin, achieving highly sensitive PA imaging of targeting probes labeled by contrast agents has remained a challenge. In this study, we introduce a novel technique called transient triplet differential (TTD) imaging which allows for substantial

reduction of tissue background signals. TTD imaging detects directly the triplet state absorption, which is a special characteristic of phosphorescence capable dyes not normally present among intrinsic chromophores of biological tissue. Thus, these triplet state absorption PA images can facilitate “true” background free molecular imaging. We prepared a known phosphorescent dye probe, methylene blue conjugated polyacrylamide nanoparticles, with peak absorption at 660 nm and peak lowest triplet state absorption at 840 nm. We find, through studies on phantoms and on an *in vivo* tumor model, that TTD imaging can generate a superior contrast-to-noise ratio, compared to other image enhancement techniques, through the removal of noise generated by strongly absorbing intrinsic chromophores, regardless of their identity.

3.3 Background

Performed in a label-free manner, PA imaging can describe the morphological structures of biological samples based on the intrinsic optical absorption contrast among various tissues. As mentioned in the introduction, using optically absorbing contrast agents can make PA imaging more powerful and versatile. While PA imaging enhanced by such contrast agents has progressed significantly since its conception and has shown promise in probing not only structural but also molecular level information in biological samples *in vivo*, one of the main challenges is the presence of various intrinsic body chromophores that produce strong background signals [4,8]. Here, we introduce a new technique called transient triplet differential (TTD) imaging which enables significant reduction of the background signal, regardless of the background chromophores.

Ordinarily, when an organic molecule is excited, it enters an excited singlet state, followed by a decay back into its ground state. This can happen via one of four processes; release

of photons (fluorescence), release of heat (vibrational relaxation), product formation (photochemistry), and intersystem crossing (ISC) into the triplet state; the latter decays at a much slower rate, from microseconds to milliseconds, through phosphorescence [29]. In the context of this study, we are focusing on the triplet state because of the presence of the long-lived triplet absorption peak that is only accessible for phosphorescent dyes. The process of generating a TTD signal is demonstrated in Figure 3.1, where a “pump” beam is used to excite the molecule from the ground state to the excited singlet state, which will then transition into the triplet state via ISC. Usually, the triplet state has a triplet absorption peak (λ_2) that is spectrally well-shifted from the original singlet state absorption peak (λ_1). By using a “probe” beam at this triplet state absorption peak, a PA signal will be generated by molecules that are in the triplet state at that time. Hence, a PA differential signal can be generated by comparing the PA signal at λ_2 with and without a “pump” beam. Since only triplet state molecules of the phosphorescent dye will generate this PA signal, the differential signal will purely originate from the phosphorescent dye. This will allow for the removal of all background signals from any biological or other relevant chromophores, as these are non-phosphorescent. We define such a PA differential signal as the TTD signal. The technique introduced in this research work is similar to transient absorption spectroscopy (TAS), which uses both “pump” and “probe” beams, except that TAS is often concerned with the excited singlet state rather than the triplet state [30].

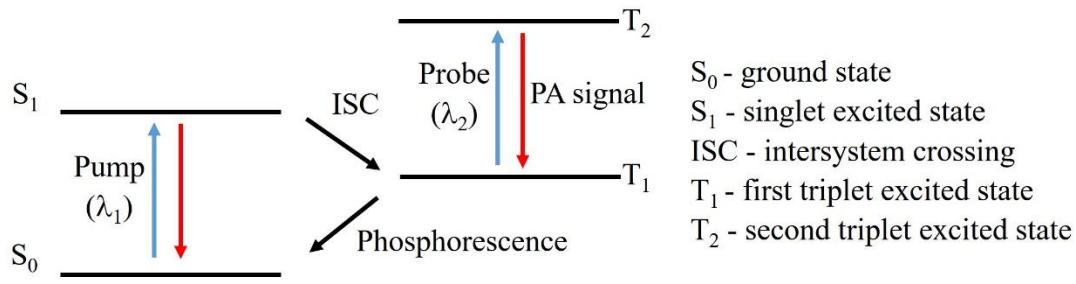

Figure 3.1 Diagram demonstrating the generation of a TTD signal. The pump is defined as the laser used to excite the molecules from the ground to the triplet state, while the probe is the laser excitation used to measure the PA signal generated from the transition between the T_2 and T_1 states.

Besides giving phosphorescence, molecules in the triplet state can also return to the ground state via quenching by other triplet state molecules, such as oxygen, which exist naturally in the triplet state [31]. This process further limits the lifetime of the phosphorescent dyes in the triplet state, where it has been shown that the triplet state molecules will decay near-exponentially in time for phosphorescent molecules such as methylene blue (MB) [20,32-34]. The decay curves are affected by the oxygen concentration and this is an area of active research, where studies, including some focusing on PA methods, are being conducted to classify and characterize the change in the decay curves with respect to the oxygen concentration, with the end goal of mapping oxygenation levels in tissue [19,21,22,31-35].

In this study, we used methylene blue conjugated polyacrylamide nanoparticles (MBNP) by using the advantages from this nano-platform that has been developed extensively [36,37]. MB is known to have a high quantum yield for ISC into the triplet state [1,38]. MB can exist in two states, a monomer and a dimer state, with different ISC efficiencies. The dimer state has a triplet excited state lifetime (10^{-8} s) that is much shorter than that of the monomer state (10^{-6} - 10^{-4} s) [1]. The relative monomer and dimer state populations are

dependent on the concentration of the MB in the media and it is very challenging to approximate correctly the optimal concentration of free MB molecules *in vivo* (maximal monomer signal with minimal dimer signal). On the other hand, the monomer/dimer ratio in MBNP is not affected by the concentrations of the nanoparticles (NPs) because the MB to NP matrix ratio is always constant [39]. As shown in Figure 3.2, the monomer/dimer ratio in MBNP was measured to be approximately 1:1. A constant monomer/dimer ratio facilitated by the polyacrylamide NPs makes the lifetime-based functional measurement quite robust, even in a complex *in vivo* environment. In addition, MB is known to degrade into colorless "leuko-methylene blue" through enzyme reductions occurring in the bloodstream; while the NP matrix can effectively protect the MB from degradation in the presence of those enzymes [36]. The nanoparticle matrix can be surface modified with a targeting moiety, such as an F3-peptide or other peptides [16,39-41]. This allows the delivery of the NPs to specific tissues, or cells, *in vivo* [16,39,42,43]. Besides that, certain sizes of NPs (50-100 nm), and specifically of these hydrogel NPs, are also known to accumulate well in tumors, due to the enhanced permeability and retention (EPR) effect [44]. All these advantages associated with the use of the polyacrylamide nano-platform could be highly valuable for future translation of the proposed technique to preclinical or clinical settings.

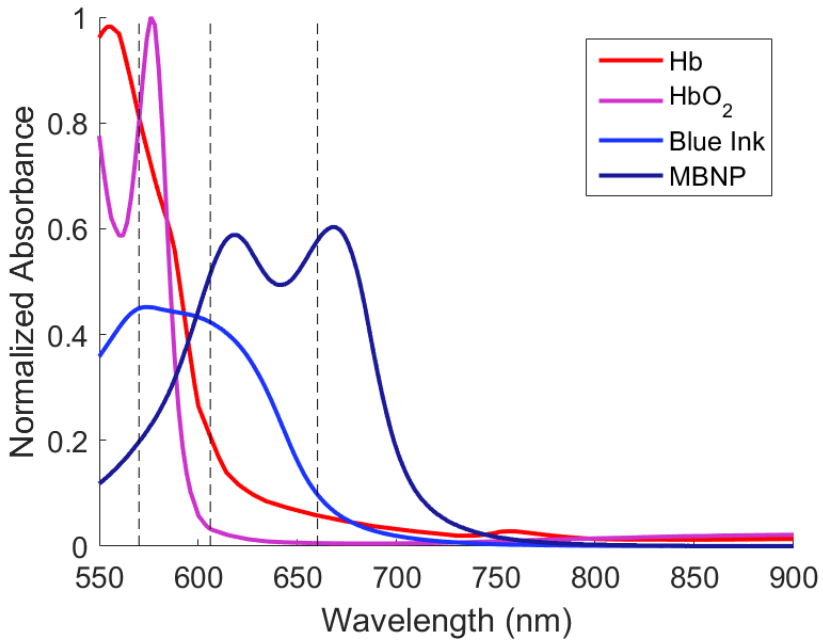

Figure 3.2 Absorption spectra of deoxyhemoglobin (Hb), oxyhemoglobin (HbO_2), MBNP, and the blue ink as measured by a UV-VIS spectrophotometer. The approximately 660 nm peak corresponds to the monomer state while the 620 nm peak corresponds to the dimer state, with both states having an approximately equal absorption. The dashed black lines correspond to the three wavelengths used for spectral unmixing. The blue ink and the MBNP have a similar absorption profile in the sense that they show the same trend as compared to Hb and HbO_2, that is they both have a higher absorption at 606 nm and 660 nm and a lower absorption at 570 nm than Hb and HbO_2.

While triplet state imaging has been used as a method for measuring oxygen levels [19,21,22,31-35], its application was not focused on producing background free PA imaging. We compare both a single wavelength contrast-agent enhanced image, and one of the more current PA background reduction techniques, called *spectral unmixing* or *multi-wavelength imaging* [24,45,46], with our newly developed TTD imaging, for both phantom and an *in vivo* study. Our results suggest that the TTD imaging technique can produce background free PA images even in the presence of strongly competing chromophore signals, which has not been achieved by the other two contrast enhancement techniques.

3.4 Methods

3.4.1 MBNP Preparation

All chemicals were purchased from Sigma-Aldrich unless otherwise noted. The MBNPs were prepared as in a previously reported method [38]. All reactions were performed in the dark. The monomer solution was prepared as follows. DCMB-SE (European Molecular Precision Biotech, 5 mg dissolved in 100 µL of DMSO) was added into 0.93 mL of Phosphate Buffered Saline (PBS, pH 7.4) containing acrylamide (368 mg) and N-(3-aminopropyl)-methacrylamide hydrochloride (Polysciences, 28 mg). The monomer solution was stirred for 2 hours at room temperature. Then, sodium dioctylsulfosuccinate (1.07 g) and Brij 30 (2.2 mL) were added into 30 mL of Hexane in a round bottom flask equipped with a stirring bar. After 30 min of argon flushing, the monomer solution was injected and flushed with argon for another 15 min. The radical polymerization was initiated by addition of 100 µL of N,N,N′,N′-tetramethylethylenediamine and 100 µL of ammonium persulfate (15 mg/100 µL in water), while stirring. After 2 hours, the hexane was evaporated with a rotary evaporator and the resulting MBNP NPs were suspended in Ethanol and transferred into an Amicon Stirred Ultrafiltration Cell equipped with a Biomax 300 kDa membrane. The solution was washed with ethanol and water several times to remove any unreacted monomers and surfactants. Then, the MBNP NPs water suspension was freeze-dried and stored at -20 ^{o}C.

For surface modifications, the MBNP solution (50 mg/2.5 mL of PBS pH 7.4) was mixed with 4 mg of bifunctional Polyethylene glycol (MAL-PEG-SCM, 2kDa, Creative PEGWorks). After 30 minutes of stirring, it was washed with PBS (4 times) using Amicon Ultra Centrifugal Filter (100 kDa) and 11 mg of F3 Peptide

(KDEPQRRSARLSAKPAPPKPEPKPKKAPAKKC, RS Synthesis) was added and stirred overnight. Then, cysteine (0.63 mg) was added and stirred for 2 hours to deactivate unreacted maleimide groups. The MBNP solution was washed with water and lyophilized. The MBNP was characterized by UV-VIS spectrometer (Shimadzu), fluorescence spectrometer (Horiba FluoroMax-3), and dynamic light scattering (Beckman Coulter).

3.4.2 General PA Imaging Setup

In all the experiments, the TTD signal was obtained by taking 3 separate PA signal measurements, specifically with a pump only laser, probe only laser, and a pump plus probe laser separated by a delay. The TTD signal is then obtained by subtracting the pump only and probe only measurements from the pump plus probe measurement. The general experimental setup for all the *in vitro* experiments is shown in Figure 3.3.

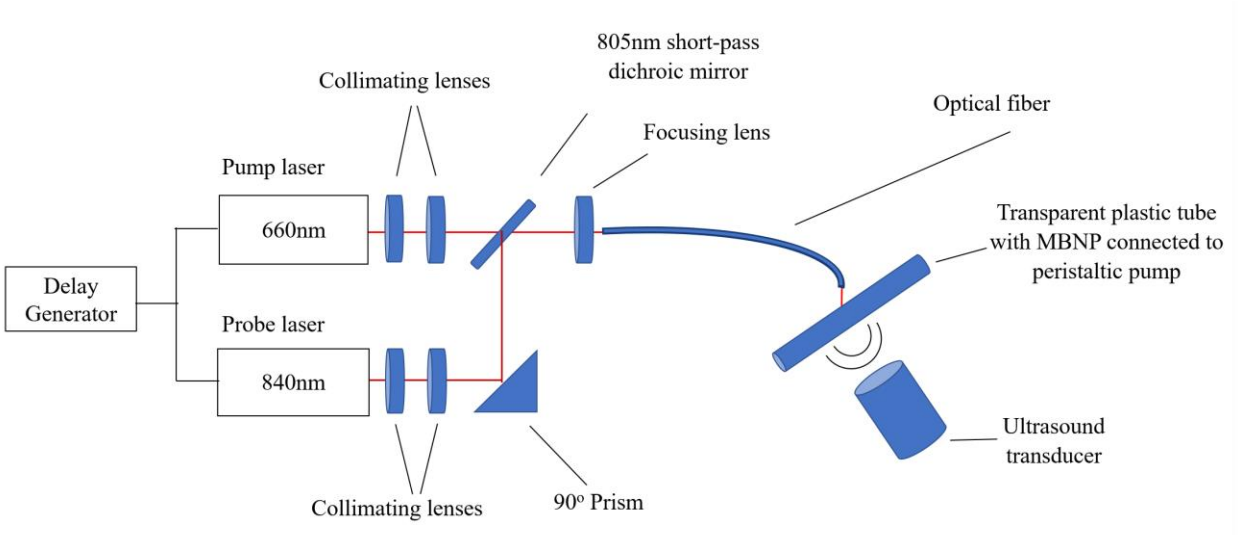

Figure 3.3 General experimental setup for PA imaging experiments.

3.4.3 Factors Affecting TTD Signal

1) Delay time

Using the setup shown in Figure 3.3, the TTD signal was measured for various delay times. The pump laser used was a tunable pulsed laser (Surelite OPO Plus, Continuum) pumped by the third harmonic of an Nd:YAG laser (Surelite, Continuum), with pulse duration of 5 ns, and tunable wavelengths in the range of 410-680 nm and 710-2500 nm. The probe laser was produced by an optical parametric oscillator (Vibrant B, Opotek, Carlsbad, CA, USA) pumped by the second harmonic output of a Nd:YAG pulsed laser (Brilliant B, Quantel, Bozeman, MT, USA), with pulse duration of 5.84 ns, and tunable wavelengths in the range of 680-950 nm and 1200-2400 nm. The transparent PVC tube was filled with 3.9 mg/mL MBNP and circulated using a peristaltic pump to ensure a continuous fresh supply of dye. An air pump was connected to the MBNP reservoir to maintain a constant level of oxygen. A section of the tubing was immersed in water to enable acoustic coupling with the ultrasound (US) transducer. A V312 cylindrically focused US transducer (Panametrics), with a central bandwidth of 10 MHz and focal length of 0.75 inch was used to detect the PA signal from the MBNP. The transducer was connected to an oscilloscope (TDS 540, Tektronix Inc) with a sampling rate of 250 MSa/s. The pump and probe wavelengths were fixed at 660 nm and 840 nm, respectively, while the delay time between the pump and the probe laser pulses was set to 0.02, 0.04, 0.06, 0.08, 0.10, 0.15, 0.20, 0.25, 0.30, 0.35, 0.40, 0.50, 0.60, 0.70, 0.80, 0.90, 1.00, 1.20, 1.40, 1.60, 1.80, 2.00, 2.50, 3.00, 3.50, 4.00, 5.00, 6.00, 7.00, 8.00, 9.00, and 10.00 µs using a delay generator (DG535, Stanford Research). Each measurement was recorded five

times, and the mean of the recordings were taken to minimize the noise due to the random fluctuations in the signal. The data was processed using Matlab.

2) Oxygen

To alter the oxygen concentrations, an additional tube connected to a gas (oxygen or nitrogen) tank was added to the peristaltic pump reservoir. Additionally, an oxygen meter (Microx TX3, Presens) was immersed into the reservoir to continually monitor the oxygen levels during the experiment. Three different oxygen levels were maintained, specifically at low oxygen (5-10%), air oxygen (21%), and medium oxygen (45%) concentrations. The low oxygen level was maintained by continually adding nitrogen gas into the reservoir, which resulted in an oxygen level of approximately 5-10%. The air oxygen level was maintained by continuously pumping air into the reservoir using the air pump. The medium oxygen level was maintained by adding both air using the air pump and oxygen using the oxygen tank and balancing the gas pressures to form a stable oxygen level. The TTD signals for 7 delay times of 0.1, 0.2, 0.5, 1.0, 2.0, 3.0, and 5.0 μs were measured at each oxygen level for a MBNP concentration of 2.0 mg/ml.

3) MBNP concentration

The delay time was fixed at 0.2 μs. The MBNP concentration was varied between 0.005 mg/ml and 3.5 mg/ml.

4) Pump and probe laser energy

The concentration of MBNP was diluted to 0.6125 mg/ml in order to attempt saturation of the TTD signal within the maximum permissible exposure (MPE) limit. The energy of the pump laser was varied in the range of 0.5-18.2 mJ/cm^2 on the sample surface while the

energy of the probe laser was varied in the range of 1.6-9.5 mJ/cm^2. The simulated energy vs penetration depth at each wavelength for each tissue was calculated using the effective attenuation coefficient, μ_{eff}, and Beer's law, as shown in equations **(3.1)** and **(3.2)**.

$$\mu_{eff} = \sqrt{3\mu_a(\mu_a + \mu_s')} \qquad \textbf{(3.1)}$$

$$\phi(z) = \phi(0)e^{-\mu_{eff}z} \qquad \textbf{(3.2)}$$

where μ_a is the absorption coefficient (cm^{-1}), μ_s' is the reduced scattering coefficient (cm^{-1}), and $\mu(z)$ is the energy at depth z. The values for μ_a and μ_s' were obtained from previously published results [2,47-49].

3.4.4 CNR and Sensitivity

To examine CNR and sensitivity, the concentration was varied in the range of 0.001-2.0 mg/ml for the MBNP with the same conditions as before. Two sets of concentration measurements were conducted, one with the MBNP suspended in distilled water, and the other with the MBNP suspended in 5% human blood to act as biological noise. The PA signals were compared between the three different methods, including 1) the single-wavelength (660 nm) PA amplitude increase due to the increasing MBNP concentration, 2) the spectrally unmixed signal, and 3) the TTD signal. The 660 nm PA amplitude increase was measured by subtracting the PA signal for a given MBNP concentration by the PA signal for a control sample where the concentration of MBNP is zero. The spectrally unmixed signal was calculated by measuring the PA signals at the three wavelengths of 570 nm, 606 nm, and 660 nm, respectively. In this case, the spectrally unmixed signal only considered Hb, HbO_2, and MBNP. From the available absorption

spectra of Hb and HbO_2, the relative concentration of the MBNP in the PA image can be calculated using the simultaneous equations **(3.3) - (3.5)**.

$$k\left([Hb]a_{Hb@570nm} + [HbO_2]a_{HbO_2@570nm} + [MBNP]a_{MBNP@570nm}\right) = PA_{570nm} \quad \textbf{(3.3)}$$

$$k([Hb]a_{Hb@606nm} + [HbO_2]a_{HbO_2@606nm} + [MBNP]a_{MBNP@606nm}) = PA_{606nm} \quad \textbf{(3.4)}$$

$$k([Hb]a_{Hb@660nm} + [HbO_2]a_{HbO_2@660nm} + [MBNP]a_{MBNP@660nm}) = PA_{660nm} \quad \textbf{(3.5)}$$

where k is a constant depending on the Grüneisen parameter of the tissue, the light fluence, and the sensitivity of the imaging system, [x] is the concentration of chromophore x, $a_{x@\lambda}$ is the absorption coefficient of chromophore x at wavelength λ, PA_λ is the photoacoustic signal at wavelength λ nm.

A constraint where the estimated concentrations had to hold positive values was imposed on the spectral unmixing algorithm. These equations also assumed a constant fluence level at the different laser wavelengths.

The TTD signal is obtained using the method specified in the beginning of the methods section. The CNR was measured by taking the PA signal for the given MBNP concentration and subtracting it from the PA signal at zero MBNP concentration, and dividing it by the standard deviation of the five measurements made for each concentration. The sensitivity was classified as the MBNP concentration before which the PA signal fell below the noise level.

3.4.5 Effectiveness in Different Background Noises

To study the effects of background noise, various samples were prepared, specifically, 2.0 mg/ml MBNP, 2.0 mg/ml MBNP in 5% blood, 2.0 mg/ml MBNP in 5% blood and 0.1%

blue ink, 2.0 mg/ml MBNP in 5% blood and 5% GNP, 5% blood, and distilled water. The GNP was obtained from IMRA America, Inc. The percentages listed are all measured by volume. The samples were prepared by taking a stock solution of 25 mg/mL MBNP and diluting it in PBS together with the other solutions to get the required concentrations. The PA measurements at the five separate wavelengths, 570 nm, 606 nm, 660 nm, 840 nm, and 660 nm + 840 nm, were obtained. The TTD and SU signal were obtained in the same way as previously mentioned.

3.4.6 Validation on an *In Vivo* Mouse Tumor Model

All procedures on live animals were performed in accordance with institutional guidelines and approved by the Institutional Animal Care and Use Committee (IACUC) at the University of Michigan. 9L glioma cells (ATCC) were cultured in RPMI 1640 media and supplemented with 10% fetal bovine serum and 1% antibiotic-antimycotic. 5-week old athymic nude fox/NU (Envigo) were subcutaneously injected with approximately 10^6 glioma cells (ATCC) in a 100 µL suspension of culture media. The tumor was allowed to grow for 2-3 weeks until it reached approximately 1 cm in diameter. For imaging, a setup similar to Figure 3.3 was used, where instead of coupling the beam to an optical fiber, a freely propagating beam was used. A commercially available research ultrasound platform (V1, Verasonics, Kirkland, WA) using a high frequency linear array transducer with central frequency of 11.25 MHz (CL15-7, Philips, Andover, MA) was used to acquire the ultrasound and PA images from the mice. A delay time of 0.5 µs between the pump and the probe lasers was used. The mouse was placed under anesthesia using 1-2% isoflurane mixed with oxygen for the duration of the experiment and intravenously injected with 0.3 mL of 20 mg/mL of F3-MBNP. The PA measurements at the five separate

wavelengths, i.e. 570 nm, 606 nm, 660 nm, 840 nm, and at 660 nm + 840 nm, were obtained for time points 0 (before the injection), 1 (right after the injection), 30, 60, and 90 minutes. To improve the SNR of the images, the images were averaged 50 times. The TTD and SU signals were obtained in the same way as previously mentioned.

3.5 Results and Discussion

3.5.1 TTD Signal for MBNP

Figure 3.4 demonstrates the process of obtaining the TTD signal. Figure 3.4A shows the superimposed waveforms (PA signals) obtained for the pump (660 nm), probe (840 nm), and pump plus probe (660 nm + 840 nm) excitations. Here, there is a noticeable increase in the signal amplitude for the second peak in the pump plus probe waveform, which corresponds to the waveform shown in Figure 3.4B. This *increase in signal* is the TTD signal. The used wavelengths of 660 nm and 840 nm are the peak singlet and triplet state absorption wavelengths, respectively, for the MBNP, which is shown in Figure 3.5. Since the delay time used is on the order of 1 µs, the TTD signal is solely due to MB in the monomeric state as all the MB in the dimer state would have returned to the ground state due to their much shorter triplet state lifetime (10^{-8} s). Previous works have identified the monomeric MB absorption peak at 660 nm and the triplet absorption peak at 840 nm [1], which matches with what was experimentally found in Figure 3.5.

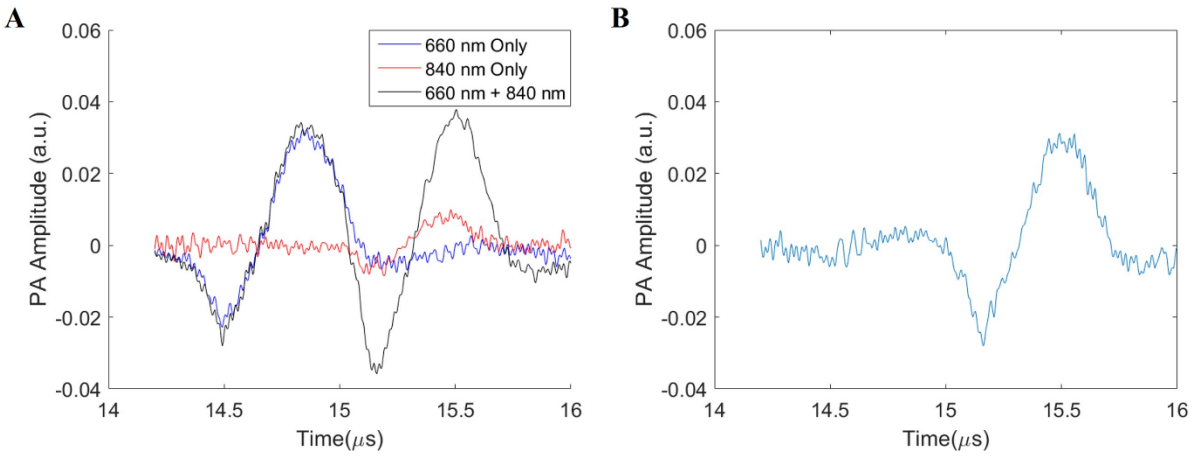

Figure 3.4 Generation of the TTD PA signal. (**A**) Superimposed PA signals from the individual wavelength measurements for the pump (660 nm), probe (840 nm), and from the pump plus probe (660 nm + 840 nm) wavelengths. (**B**) TTD signal obtained by subtracting the individual 660 nm and 840 nm signals from the 660 nm + 840 nm signal for a 2.0 mg/mL MBNP sample in a visible-light transparent tube with a 0.5 µs delay time.

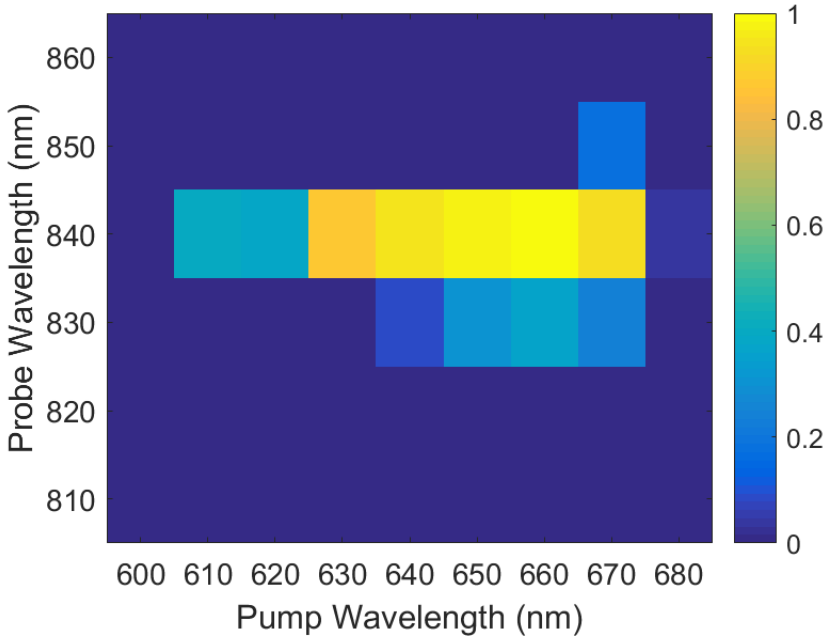

Figure 3.5 Wavelength dependence of the MBNP as measured by PA imaging. Colorbar indicates the normalized TTD signal. The peak TTD signal occurs at 660 nm (pump) and 840 nm (probe) which are the same as the result previously reported in the literature for monomeric MB [1].

3.5.2 Factors Affecting TTD Imaging

We looked at the effects of multiple parameters on the TTD signal of MBNP, specifically the delay time between the pump and probe lasers, oxygen level, MBNP concentration, and the pump and probe laser energy. Two other factors that also affect the TTD signal, that of the laser wavelengths and the monomeric-dimer ratio of the MBNP, are not discussed in Figures 3.6 and 3.7 as the former has already been determined for monomeric MB, while the latter is fixed in the case of the MBNP.

Figure 3.6A demonstrates the relationship between the TTD amplitude and the delay time for MBNP from 0.02 µs to 10 µs. The TTD amplitude follows a decaying exponential relationship with increasing delay time as reported in previous studies [21,33]. From Figure 3.6B, we see that the slope of the exponential decay of the TTD amplitude increases as the oxygen concentration increases. As mentioned previously, since oxygen exists naturally in the triplet state, the higher the concentration of oxygen, the more triplet oxygen molecules are available to quench the triplet state MB molecules. This leads to a faster decay in the TTD amplitude as the concentration of oxygen increases. At low oxygen levels (5-10%), we see an almost linear relationship between the TTD amplitude and the delay time, which has been previously reported [22]. Figure 3.6C shows that the TTD amplitude has a linear relationship with the concentration of MBNP, as expected.

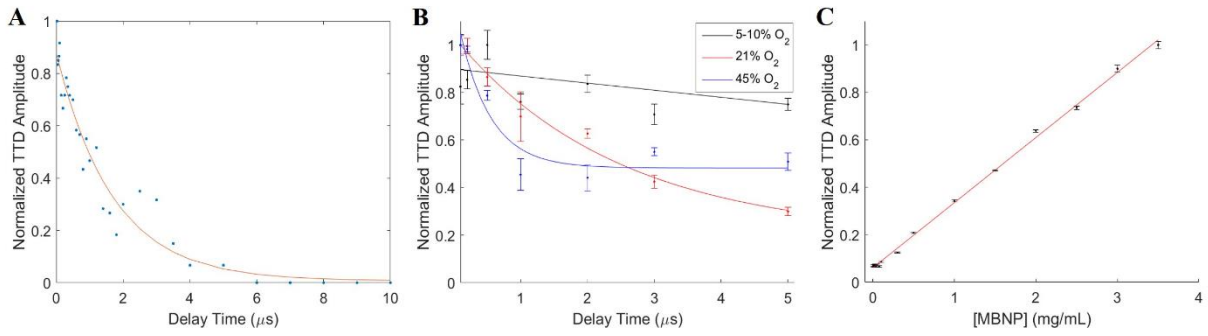

Figure 3.6 Normalized TD signal for (**A**) Varying delay times, with exponential decay curve fit of $r^2 = 0.9485$, (**B**) Low (5-10%), air (21%), and medium (45%) oxygen levels of the MBNP sample solution, and (**C**) Varying [MBNP] in PBS. Error bars indicate the standard deviation of the signal for 5 repeated measurements.

Theoretically, we expect the TTD amplitude to vary linearly with pump and probe energy. The greater the pump energy, the greater the amount of MB molecules that are pumped into the triplet state, and hence the greater the TTD amplitude. Similarly, the greater the probe energy, the greater the amount of triplet state molecules that are excited, and hence the greater the TTD amplitude. This linear relationship only holds until saturation, since the maximum TTD amplitude is dependent on both pump and probe energies, and one or the other will act as a limiting factor. In the case of excess probe energy, the limitation factor becomes the number of triplet state molecules that are available to be excited, which is determined by the pump energy. In the case of excess pump energy, the limitation factor becomes the energy available to excite the triplet state molecules, which is determined by the probe energy.

Figure 3.7A shows the general trend: As the pump and probe energy increases, the TTD amplitude increases. Figure 3.7B shows the relationship between the TTD amplitude and probe energy for various fixed pump energies. For low probe energies, the TTD amplitude increases approximately linearly with pump power before reaching a plateau. As the probe energy increases, the pump energy level at which the TTD amplitude plateaus increases. At the highest probe energy used, the TTD amplitude never reaches a plateau within the experimental range of pump energy values used. This means that within the experimental values used, the MBNP is never fully saturated. Looking at the two plateau values for 4.3 mJ/cm^2 and 6.4 mJ/cm^2 probe energies, the TTD amplitude decreases by 29% for a 33% decrease in probe energy, which supports the linear relationship between

the TTD amplitude and the probe energy. Figure 3.7C shows a similar relationship between the TTD amplitude and probe energy for various fixed pump energies. Looking at the two plateau values for 5.7 mJ/cm^2 and 7.7 mJ/cm^2 pump energies, the TTD amplitude decreases by 32% for a 26% decrease in pump energy. Figure 3.7D shows the simulated penetration depth for TTD imaging in the skin and breast using available optical absorption and scattering information from literature [2,47-49]. These two tissue types are shown to demonstrate the feasibility of using TTD imaging in, for example, skin and breast cancer related diseases. Here, the estimated maximum penetration distance for TTD imaging (based on the maximum permission exposure limit of 20 mJ/cm^2) is approximately 3.9 mm for the skin and 12 mm for breast tissue, where, in both cases, the pump wavelength (660 nm) acts as the limiting energy factor, due to the fact that 660 nm light cannot penetrate as well as 840 nm light in optically scattering biological tissues.

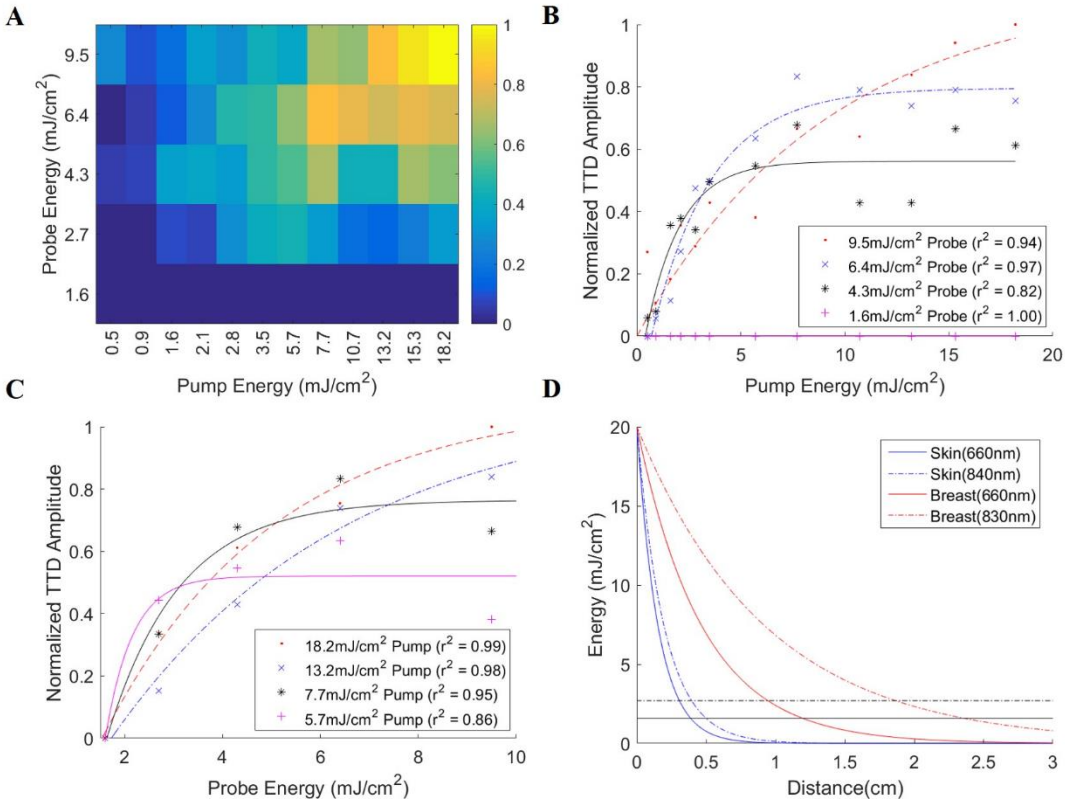

Figure 3.7 Energy dependence of the TTD amplitude, with **(A)** showing the normalized TTD amplitude 2-D plot vs pump and probe energy, **(B, C)** showing the normalized TTD amplitude vs pump/probe energy at 4 fixed probe/pump energy levels respectively, and **(D)** showing the simulated energy vs penetration depth for skin and breast tissue with initial fluence of 20 mJ/cm^2 (maximum permissible exposure limit). Colorbar in **(A)** shows the normalized intensity based on the maximum TTD intensity. The black lines (solid – 660 nm, dashed – 840 nm) in **(D)** indicate the minimum energy required for TTD imaging for the respective wavelengths, derived from **(A)** where the minimum pump energy is taken as 1.6 mJ/cm^2 and the minimum probe energy as 2.7 mJ/cm^2.

3.5.3 Contrast-to-Noise Ratio and Sensitivity

In terms of contrast-to-noise ratio (CNR), Figures 3.8A-C show that TTD imaging clearly has the superior CNR at all detectable concentration levels, followed by spectral unmixing (SU), and subsequently by the MBNP contrast agent at 660 nm. The CNR for TTD imaging is approximately double that of SU at all concentrations, and triple that of the MBNP contrast agent alone. Figures 3.8D-F show the sensitivity of the various imaging techniques for MBNP in the presence of 5% blood, while Figures 3.8G and 3.8H show the sensitivity of MBNP in the presence of water. Here, we found that TTD imaging has approximately the same sensitivity levels in *both* blood and water, being able to detect up to 0.05 mg/mL of MBNP. This high sensitivity level is significant as it allows for its potential use *in vivo*, where this concentration would involve a 400 times dilution of a typical injection volume using 20 mg/mL MBNP. This means that even if the target area receives a concentration of only 1/400 of the injected MBNP, the sensitivity offered by TTD imaging will still be high enough to detect it. In addition, TTD imaging demonstrates a 10x superior detection sensitivity compared to that of just using the MBNP contrast agent, and shows detection sensitivity similar to that of SU. The TTD amplitude itself is also unaffected by the blood, as can be seen from having similar PA amplitudes for the various concentrations in blood and in water (Figures 3.8F and 3.8H). While TTD imaging seems to have a similar sensitivity to SU, the body has many more additional chromophores beyond the two chromophores accounted for of deoxyhemoglobin (Hb) and

oxyhemoglobin (HbO_2), such as melanin, lipids, etc., which will make SU significantly more challenging *in vivo*.

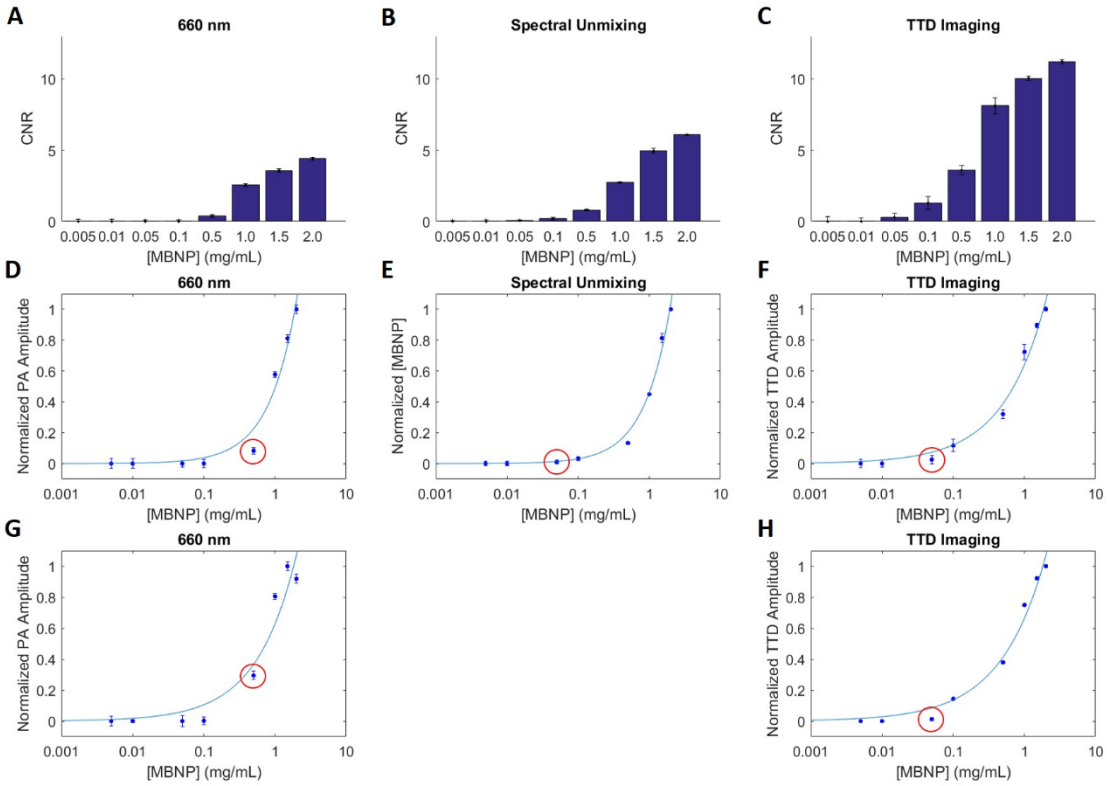

Figure 3.8 CNR and sensitivity measurements comparing 3 methods; MBNP, as a contrast agent, taken at its absorption peak of 660 nm (**A, D, G**), spectral unmixing (SU) (**B, E**), and TTD imaging (**C, F, H**). The CNR in (**A-C**) where measured by taking the difference between the PA signal at a given concentration and the PA signal at zero concentration of MBNP, divided by the maximum noise fluctuation. Figures **(D-H)** show the minimum detectable concentration of MBNP (sensitivity) which are labeled by the red circles. Figures (**A-F**) corresponds to MBNP suspended in 5% blood to mimic physiological conditions, while (**G, H**) are suspended in water. 5% blood was used as most biological tissues contain between 0-5% of blood by volume [2]. Spectral unmixing was not conducted for the MBNP in water due to the absence of deoxyhemoglobin and oxyhemoglobin in the sample. Error bars indicate the standard deviation of the signal for 5 repeated measurements.

3.5.4 Effectiveness in Different Background Noises

Figure 3.9A shows the PA amplitudes of the six different samples at the 5 chosen wavelengths reflecting the spectroscopic absorption property of each sample. As expected, samples with 2.0 mg/ml MBNP show a higher absorption at 660 nm as compared to the controls. The blue ink (0.1%) acts as an unknown chromophore which

significantly increases the absorption at 570 nm, 606 nm, and 660 nm and acts as an increased background noise at those wavelengths. Samples containing 5% whole blood show a higher absorption at all the wavelengths except at 660 nm which is dominated by the MBNP signal. The sample containing 5% gold nanoparticles (GNP) with a peak absorption wavelength at 532 nm acts as the second unknown chromophore, showing a small increase in PA amplitude at the 570 nm and the 606 nm wavelengths due to residual optical absorbance. Figure 3.9B shows that there is no statistical difference between the TTD amplitude obtained for the four samples containing MBNP, which suggests that the TTD amplitude is independent of the background chromophores present in the sample. Importantly, the two control samples did not show any TTD signal, which demonstrates the potential of TTD imaging for removing background noise. This is contrasted with the SU method in Figure 3.9C, which shows a baseline signal even in the absence of any MBNP. Furthermore, the SU method shows a significantly increased error in the estimated MBNP concentration for the sample containing the blue dye, as it was indistinguishable by the SU algorithm from the MBNP, since the blue dye and the MBNP have similar absorption profiles for the chosen wavelengths, as shown in Figure 3.2. The SU method also shows a significant difference for the 2.0 mg/mL MBNP in 5% blood sample, which is probably due to errors in the unmixing algorithm, arising from ignoring all other chromophores beyond the MBNP, Hb, and HbO_2. These unaccounted-for chromophores include water as well as the transparent PVC tubing used to hold the sample. This result on phantoms demonstrates the ability of TTD imaging to isolate the MBNP signal from those of both known and unknown background chromophores. The

presence of these chromophores is almost inevitable for any *in vivo* imaging application.

A similar example in the presence of a muscle tissue background is shown in Figure 3.10.

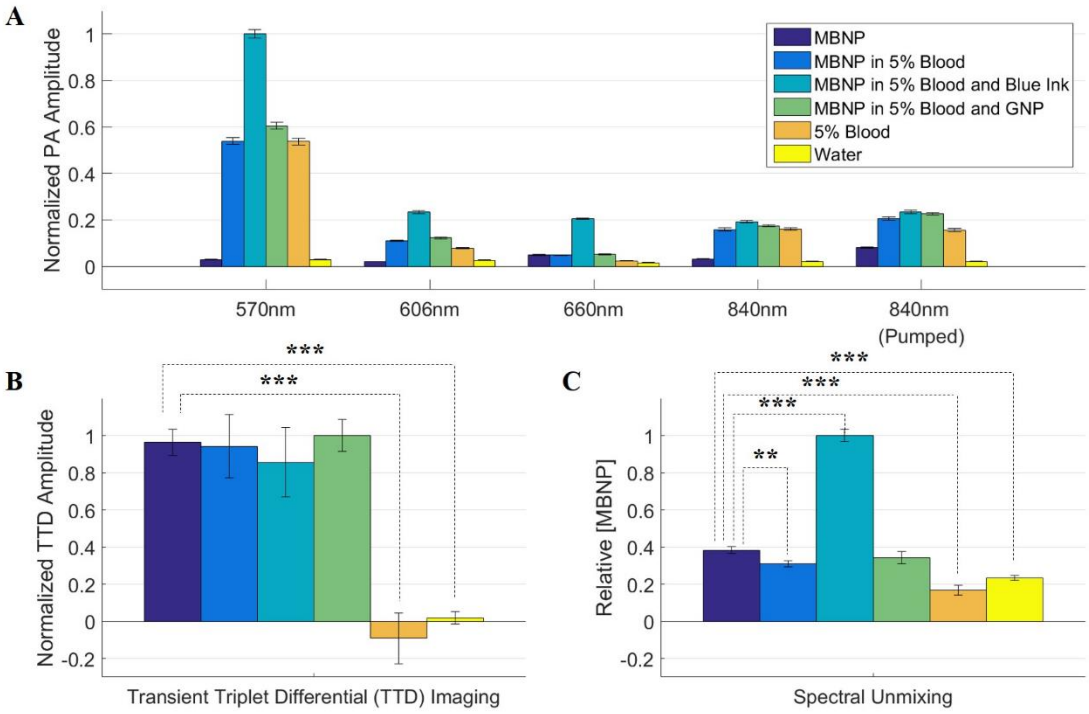

Figure 3.9 Data comparing the TTD imaging method and SU for six different samples, including 2.0 mg/ml MBNP, 2.0 mg/ml MBNP in 5% whole blood, 2.0 mg/ml MBNP in 5% whole blood plus 0.1% blue ink, 2.0 mg/ml MBNP in 5% whole blood and 5% gold nanoparticles (GNP), 5% whole blood, and water. Both the 5% blood and the water samples act as the controls. (**A**) Normalized PA amplitude at 5 separate wavelengths. (**B**) Normalized TTD amplitude. (**C**) Relative MBNP concentration measured by spectral unmixing. Error bars indicate the standard deviation of the signal for 5 repeated measurements. ** represents $p<0.01$, and *** represents $p<0.001$ for a t-test with hypothesis that the normalized TTD amplitude/relative [MBNP] of the sample is equal to that of the MBNP only sample.

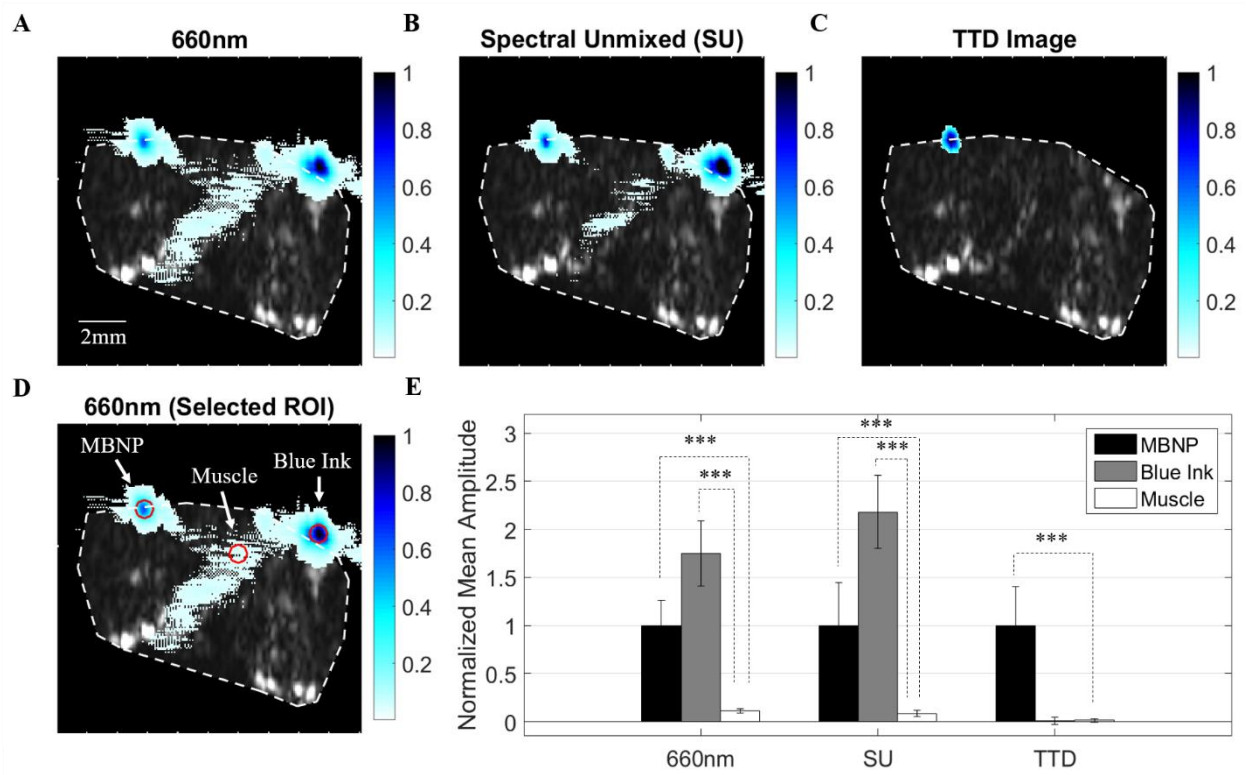

Figure 3.10 PA imaging results on a rat muscle where a drop of MBNP and a drop of blue ink were added to the top surface of the muscle tissue (MBNP at the left; blue ink at the right). Here, the PA images superimposed on a gray-scale ultrasound image are shown for **(A)** the raw MBNP signal taken at its absorption peak of 660 nm, **(B)** the spectral unmixed signal detailing the estimated concentration of MBNP, and **(C)** the TTD image. The white dotted line details the muscle tissue outline. **(D)** shows the region-of-interest (ROI) selected for quantitative analysis (outlined in red), centered at the maximum intensity with size chosen to match expected sample drop size. Colorbar shows the normalized intensity based on the maximum intensity within each imaging method. **(E)** shows the normalized signal amplitude for the selected ROI for the three different methods. Error bars indicate the standard deviation within each selected ROI. *** represents $p<0.001$ for a t-test with hypothesis that the normalized signal amplitude for the selected ROI is equal to that of the muscle (control) ROI.

3.5.5 Validation on an *In Vivo* Mouse Tumor Model

To demonstrate the applicability of the TTD technique *in vivo*, we show time-lapse images of a subcutaneous mouse tumor model. F3-conjugated MBNPs were injected intraveneously and preferentially accumulate in the tumor through both F3-targeting [42,43] and the EPR effect. Figures 3.11A-C show the superimposed, time-lapsed ultrasound and PA images of the tumor at a single wavelength of 660 nm (Figure 3.11A), MBNP concentration as determined via SU (Figure 3.11B), and TTD imaging (Figure 3.11C).

The image at time 0 shows the tumor before the MBNP injection, while the image at time 1 shows the tumor immediately after injection, while 30, 60, 90 mins designate the times after the injection, respectively. Here, we see that at time 0, the TTD image shows an almost zero signal, with increasing signals as time progresses, due to accumulation of the MBNP in the tumor. In contrast, we see some baseline signal at time 0 for both the 660 nm and SU image, although it is significantly smaller in the case of the SU image, and a similar increase in signal as time progresses. There is peak accumulation of the MBNP in the tumor at around 30-90 mins, where the signals in all 3 imaging methods are relatively consistent. It should be noted that most of the TTD signal is localized within the tumor, while there are background signals for the other two methods. However, the majority of the TTD signal is located towards the upper region of the tumor, which is most likely an indicator of the energy constraints of this technique. Figure 3.11D shows the normalized mean tumor signal based on the region-of-interest (ROI) shown in Figure 3.11A. Figure 3.11E shows the change in the mean tumor signal with respect to the mean tumor signal at time 0 min. Figures 3.11D and 3.11E together show the superiority of the TTD imaging method in removing background signals compared to the other two methods, as demonstrated by the low signal in the tumor at times 0 and 1 min, and the corresponding order of magnitude increase in tumor signal after MBNP accumulation.

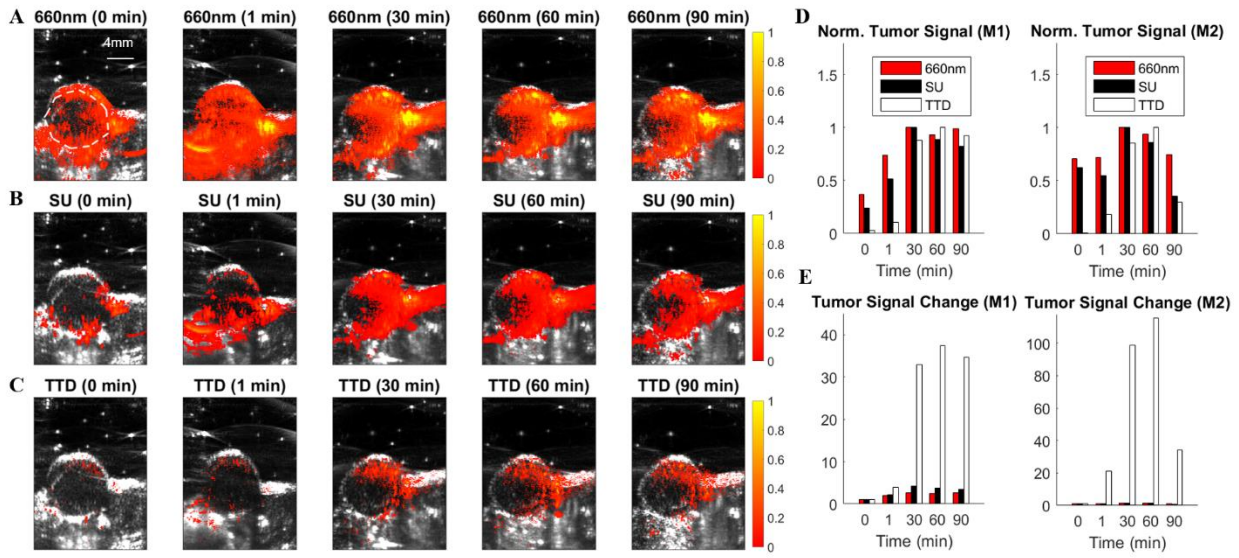

Figure 3.11 *In vivo* time-lapse images of a mouse subcutaneous tumor model using: (**A**) a single wavelength at 660nm, (**B**) MBNP concentration as determined via SU, and (**C**) TTD imaging. Each PA image is superimposed on the B-scan ultrasound image in gray scale. Time scales indicate the time after MBNP injection, with 0 min being just before the injection. The ROI shown at time 0 min in (**A**) was chosen to encapsulate the whole tumor except the tumor boundaries, which typically generate a much larger PA signal compared to the rest of the tumor. The colorbar shows the normalized intensity based on the maximum intensity within each imaging method. (**D**) Normalized mean tumor signal as a function of time within the ROI indicated in (**A**). (**E**) Mean tumor signal change based on the mean tumor signal at time 0 min. M1 and M2 indicates two separate animal experiments that were conducted. The figures shown in panels **(A-C)** are from M1.

3.6 Discussion

While TTD imaging is dependent on many different parameters, most of the parameters can be controlled or accounted for so as to ensure a consistent TTD signal. The pump and probe laser wavelengths, delay times, and monomer/dimer ratio of the MBNP can be controlled and optimized so as to maximize the TTD signal. The first two are modifiable parameters of the lasers while the monomer/dimer ratio can be controlled by modifying the composition of the MBNPs. The oxygen dependence of the TTD signal can be reduced by using a short delay time, during which the TTD signal can be assumed to be approximately invariant to oxygen, as demonstrated in Figure 3.6. That being said, the oxygen dependence of this method can also be exploited to measure oxygen saturation

[19,33], enabling both contrast enhancement and oxygen measurements. The energy dependence of the TTD signal is harder to control, due to effects such as light scattering and absorption. To minimize energy effects on the TTD signal, an energy level that saturates the TTD contrast agent should be used, if possible. If a TTD contrast agent can be designed such that it has a lower saturation energy, it could potentially minimize the energy dependence of the TTD signal. In addition, since the TTD signal follows a linear relationship with concentration, the amplitude of the TTD signal should be a direct indicator of the concentration of the MBNP, with deviations only resulting from differences in energy and oxygen levels. Despite the TTD imaging being limited by its energy requirements, the effective imaging depths offered by the current design of the MBNP are estimated as 3.9 mm for skin and 12 mm for breast tissue. In addition, we have demonstrated that we can obtain the TTD signal for an imaging depth of at least 5 mm in an *in vivo* mouse model.

It should be noted that the microsecond scale of the delay time between the pump and the probe light pulses can potentially lead to an overlap of the PA signals from the two pulses, since acoustic waves travel at a much slower velocity than light waves. This could potentially cause problems such as a reduction in the dynamic range of the system due to the increase in the maximum amplitude of the combined signal. In addition, interference between the pump and the probe PA signals could occur. A potential solution to this would be to design a TTD contrast agent with a longer delay time such that the two PA signals do no overlap. An example of a TTD contrast agent such as this would be the oxyphor G2 dye which has a lifetime of up to 250 µs [21]. It should be noted, however, that while this might solve the above-mentioned issues, it could potentially lead to other problems. A

longer lifetime also means a longer image acquisition time which could be a problem for time variant systems, for example when the body motion of the imaging subject cannot be ignored. The above-mentioned dynamic range issue can also be solved by calculating the TTD signal in an analog circuit before conversion into a digital system, so as to maximize the dynamic range of the system in detecting the TTD signal.

While we have used MBNP for this proof-of-concept study, there are in fact many other organic dyes capable of phosphorescence that are available for use [29]. Organic dyes, while only forming a subset of PA contrast agents, hold a better chance for clinical translation due to their better biocompatibility and potentially less toxicity. In fact, we chose to use MB for this study as it is both an FDA-approved dye, and a very commonly used contrast agent. That being said, there has been research into triplet states for inorganic dyes, such as gold nanoclusters, although their triplet state absorption was not studied extensively [50]. This TTD technique is unique in the sense that it enhances contrast agents that are already widely used in PA imaging to realize molecular level studies of cancer and a variety of other diseases (with MB itself being a common PA contrast agent). In particular, we expect this method to be widely applicable and to have a broad impact in the cancer imaging field, especially for the targeted imaging of superficial or quasi-superficial cancers, such as skin, head and neck, gastrointestinal track, and urethral track cancers. In this study, we have demonstrated the feasibility of achieving this, using our tumor-targeting F3-peptide conjugated MBNP for subcutaneous tumor imaging. However, since this TTD technique relies on triplet state absorption, there could be potential damage to the cells if the concentration of the phosphorescent dye and the laser energy is high enough. This happens because there is interaction between the triplet state dye

and the triplet state oxygen, leading to the formation of reactive oxygen species. Because the main application that we are envisioning for this method is in targeted imaging of cancer, this potential biological damage to the surrounding cancer cells during TTD imaging could actually be beneficial. In other words, the TTD-based PA imaging powered by MBNP could be a theranostic platform for both diagnosis and treatment of cancer.

3.7 Conclusion and Future Steps

In summary, the experimental results on MBNP demonstrate the ability of TTD imaging to provide background free PA images in a way that was not achieved by the other two previously established image enhancement methods. TTD imaging has a 3x superior CNR and 10x higher sensitivity than the method using a single-wavelength contrast agent enhanced image. Furthermore, TTD is independent of the background chromophores, while SU is significantly affected by background chromophores with optical absorption spectra similar to those of the chromophore of interest. Unlike SU, TTD imaging does not require knowledge of the spectra of the background chromophores in order to remove them from the image signal. In addition, there will be a non-zero baseline signal for SU, if additional wavelength measurements are not performed to account for all the chromophores present in the sample. While not shown in the results, in theory, the TTD method will allow for the use of multiple contrast agents without having to worry about spectral overlapping. As long as one of the parameters (pump wavelength, probe wavelength, or lifetime) are different, the signals from each respective dye can be isolated. Lastly, SU also takes a significantly longer post-processing time due to the calculations needed to be performed, and can also potentially take a longer acquisition time, depending on the number of wavelength measurements needed to be performed.

While SU is an established processing tool for most optical imaging techniques, TTD imaging could prove more useful in complicated biological systems with many different competing chromophores, where the above ability to remove the contributions of all these chromophores and isolate the TTD signal from the phosphorescence dye can be highly valuable in applications such as in molecular imaging of cancerous tissue, in which we have demonstrated the feasibility of accomplishing using our F3-conjugated MBNP in an *in vivo* subcutaneous tumor mouse model.

CHAPTER 4

Photoacoustic Imaging of Clofazimine Hydrochloride Nanoparticle Accumulation in Cancerous vs Normal Prostates

4.1 Brief Foreword

This research work represents a method for PA contrast enhancement of prostate cancer using a macrophage-targeting FDA approved drug called clofazimine. The results have been published in the following article:

"Tan, J. W. Y., Murashov, M. D., Rosania, G. R. & Wang, X. Photoacoustic imaging of clofazimine hydrochloride nanoparticle accumulation in cancerous vs normal prostates. *PLOS ONE* **14**, e0219655, doi:10.1371/journal.pone.0219655 (2019)"

and most of the following text and figures are quoted verbatim from the above-mentioned publication.

4.2 Abstract

Prostate cancer was the most common form and had the second highest death rate of male cancer in the United States in 2015. Current diagnosis techniques, such as prostate-specific antigen tests, transrectal ultrasound scans, and biopsies, are often inconclusive, and in the latter case, invasive. Here, we explore the use of clofazimine hydrochloride nanoparticles (CFZ-HCl NPs), a repurposed formulation from an FDA-approved antimycobacterial agent, as a photoacoustic contrast agent for the evaluation of prostate

cancer due to its macrophage-targeting capabilities and high optical absorbance at 495 nm. Using a transgenic adenocarcinoma of the mouse prostate (TRAMP) mouse model, our results indicate a preferential accumulation of intravenously injected CFZ-HCl NPs in cancerous prostates over normal prostates. Differences in accumulation of CFZ-HCl NPs between cancerous and normal prostates were determined using a two-wavelength unmixing technique via *ex vivo* photoacoustic imaging. Thus, intravenous injection of CFZ-HCl NPs leads to differences in the interactions of the particles with cancerous vs normal prostates, while allowing for photoacoustic detection and analysis of prostate cancer. These findings could lead to the development of a new noninvasive technique for the detection and monitoring of prostate cancer progression in an animal model that can potentially be translated to human patients.

4.3 Introduction

Prostate cancer was the leading form of cancer among men (183,529 new cases) and had the second highest death rate for cancer among men in the United States (28,848 deaths), as reported in 2015 [51]. For many years, prostate-specific antigen (PSA) blood tests and digital rectal examinations (DREs) have been the first line of detection for prostate cancer. While PSA tests act as an indicator for the stage and prognosis of the prostate cancer, PSA levels can vary significantly depending on factors such as age, lifestyle, and other medication [52-54]. Therefore, this test is rarely used on its own as a definitive indicator of prostate cancer. Abnormal readings in the PSA levels or suspicious nodules found through DREs will usually be followed up with a transrectal ultrasound scan (TRUS), which is usually complimented with a biopsy due to the fact that TRUS by itself has a low sensitivity and specificity [55,56]. However, prostate biopsies are invasive

procedures that can cause potential complications and have significant false-negative rates (e.g. 15% - 31% for the traditional sextant core biopsies) [57-63]. Magnetic resonance imaging (MRI) has also been used in the assessment of prostate cancer [64-67]. However, patients with prostates that are suspected of being cancerous through MRI assessment still typically require a biopsy for confirmation of the prostate cancer [64,65,68]. Thus, there is a need to develop novel techniques for detecting prostate cancers through noninvasive means.

In this study, we explored the differences in the interaction of clofazimine hydrochloride nanoparticles (CFZ-HCl NPs) [69] with normal and tumor bearing prostates, using the transgenic adenocarcinoma of the mouse prostate (TRAMP) animal model [70]. CFZ is a red-pigmented dye and a weakly basic, FDA-approved, orally administered, antimycobacterial agent that is recommended by the World Health Organization as a treatment for leprosy and multidrug resistant tuberculosis [71-79]. In patients, CFZ exhibits atypical pharmacokinetic properties that result in accumulation and stabilization in tissue macrophages of solid drug biocrystals that resemble a hydrochloride (HCl) salt form of the drug [80-85]. These CFZ-HCl biocrystals were determined to be biocompatible, stable, long-lived, relatively non-toxic, and anti-inflammatory [86,87], which led to the development of a biomimetic formulation of CFZ-HCl NPs for parenteral administration [69]. Importantly, Murashov et al. demonstrated that these CFZ-HCl NPs preserved the majority of characteristics of CFZ-HCl biocrystals, including targeting and accumulating inside macrophages *in vitro* and *in vivo* [69]. Thus, the presence of tumor associated macrophages (TAM), including those in prostate tumors [88,89], makes CFZ-HCl NPs a potentially useful targeting agent for prostate cancer detection.

In addition to the functional and therapeutic properties, CFZ-HCl NPs have also been shown to exhibit a strong signal in the Cy5 fluorescence range (650 nm excitation/670 nm emission) and peak optical absorbance at 495 nm [69,90]. In contrast to the free dye CFZ, CFZ-HCl NPs have a redshifted peak optical absorbance at 495 nm (compared to 450 nm for free dye CFZ), making it more suitable for biological optical applications due to the reduced interference from endogenous chromophores, such as blood at this longer wavelength [91]. This strong optical absorbance makes it a suitable contrast agent to be used with photoacoustic (PA) imaging. Notably, we have previously demonstrated the capabilities of CFZ as a PA contrast agent for potential applications in arthritis [91].

In this study, we hypothesized that intravenous (IV) administration of the biomimetic formulation of CFZ-HCl NPs will result in differences in distribution of the particles in cancerous prostates and in normal prostates, which will be measurable via PA imaging. By correlating the PA signals with histopathology and quantitative drug analysis of nanoparticle distribution in the prostates, our results clearly showed a higher accumulation of CFZ-HCl NPs in cancerous prostates over normal prostates, which led to greater PA signals using a multiple wavelength PA image analysis technique. Thus, CFZ-HCl NPs may offer a noninvasive probe using PA imaging for the detection and longitudinal assessment of prostate cancer progression in an animal model with potential biomedical relevance in humans.

4.4 Methods

4.4.1 IV Injection of CFZ-HCl NP in Mice

Animal care was provided by the Unit for Laboratory Animal Medicine (ULAM) and all procedures on live animals were performed in accordance with institutional guidelines and approved by the Institutional Animal Care and Use Committee (IACUC) at the University of Michigan (PRO00007593; 5 May 2017). Euthanasia was performed with carbon dioxide, followed by removal of the heart.

A total of 9 mice were divided into the following 3 groups of mice (n = 3 per group): (1) Diluent injected TRAMP mice (19 weeks, Strain 008215, Jackson Laboratory, Bar Harbor, ME, USA), (2) CFZ-HCl NP injected normal mice (19 weeks, C57BL/6, Jackson Laboratory, Bar Harbor, ME, USA), and (3) CFZ-HCl NP injected TRAMP mice (19 weeks, Strain 008215, Jackson Laboratory, Bar Harbor, ME, USA). The time indicated was the age of the mice at the point of euthanasia. For the diluent injected mice (Group 1), a total of 0.3 mL of diluent with 0 mg/mL CFZ-HCl NP was IV injected into each mouse. Briefly, the diluent for the IV injectable formulation was made using polysorbate 80 (0.5% w/v, 59924 Sigma-Aldrich, St. Louis, MO, USA); sodium chloride (BP358, Fisher Scientific, Fair Lawn, NJ, USA) for isotonicity; and Milli-Q water. The pH was adjusted to pH 5 using 0.01 M HCl or 0.01 M NaOH to ensure the stability of CFZ-HCl NPs in the formulation. The diluent was sterilized by sterile filtration with a syringe filter (09-719A; 0.22 µm, MCE, Sterile; Fisher Scientific, Fair Lawn, NJ, USA). The full details of the diluent formulation have been published previously [69].

For the CFZ-HCl NP injected mice (Groups 2 and 3), a total of 0.3 mL of 19 - 23 mg/mL CFZ-HCl NP was IV injected into each mouse, with the concentration of CFZ-HCl NP scaled according to the weight of the individual mice (a total CFZ-HCl NP dose of 200 mg/kg). The full details of the CFZ-HCl NP formulation have been published previously [69]. This dose was selected as it represents an equivalent amount to 3-4 weeks of oral feeding performed in previous studies which allowed for sufficient accumulation of the drug in the organs [90]. After 24 hours, the mice were sacrificed, and the prostates were harvested. Each prostate was separated into two halves: one half was snap frozen in liquid nitrogen for drug quantification, and the other half was embedded in Tissue-Plus Optimal Cutting Temperature (OCT) compound (4585, Fisher HealthCare, Houston, TX, USA) for histopathology.

4.4.2 Quantification of CFZ-HCl NP in Tissues

Quantification of CFZ-HCl NPs in tissues was performed using a previously published protocol with some modifications [90]. Briefly, the harvested prostate was thawed, weighed, cut, and homogenized by sonication and mechanical homogenizer (Pro200; Pro Scientific, Oxford, CT) in Pierce® radioimmunoprecipitation assay (RIPA) buffer (89900; Thermo Scientific, Rockford, IL, USA). Homogenates were then filtered through Pierce® tissue strainers (87791; 250 µm, Thermo Scientific, Rockford, IL, USA) utilizing the gentle centrifugation (200 x g at 4°C for 5 min). The lipophilic tissue fraction was extracted with xylenes (CAS 1330-20-7/100-41-4; Fisher Chemical, Fair Lawn, NJ, USA) in triplicates, followed by the second extraction in triplicates with 9 M H_2SO_4 of diprotonated CFZ from the xylenes extract. Samples were centrifuged (2,000 x g at 4°C for 10 minutes) to facilitate layer separation during extractions. After acid fractions were collected, the

volumes were recorded, and CFZ-HCl NP concentrations were determined spectrophotometrically. The absorbance of the supernatants was measured at λ = 540 nm (A_{540}) and 750 nm (A_{750}) using a Synergy-2 plate reader (Biotek Instruments). Corrected absorbance (A_{540} - A_{750}) was used to determine CFZ-HCl NP content via a standard curve of standards in 9 M H_2SO_4, and the concentration values were corrected for organ weight. To correct for extraction yield, known amounts of CFZ were added to the prostate sample before extractions; these samples were processed and analyzed concurrently with the test samples. For prostate tissues, the extraction yield averaged 83%.

4.4.3 Histopathology

Histopathology was performed using a previously published protocol with some modifications [69]. In brief, the frozen tissue blocks were sectioned (6 µm thick) using a Leica 3050S cryostat, and fixed in 4% paraformaldehyde (15710, Electron Microscopy Sciences, Hatfield, PA, USA) for 10 min. The samples were incubated with Hoechst 33342 solution (H3570; 1 µM stock; 1:10,000 dilution in PBS; Life Technologies, Carlsbad, CA, USA) for 10 min at room temperature for nuclear detection. After staining was complete, sections were mounted with a drop of ProLong® Gold antifade reagent (P36930, Life Technologies, Carlsbad, CA, USA) and sealed with a cover slip. For the hematoxylin and eosin (HE) staining, the sectioning and staining were performed by the In-Vivo Animal Core of ULAM at the University of Michigan. Brightfield and fluorescence images were acquired as described in the section “Brightfield and Fluorescence Microscopy”.

4.4.4 Brightfield and Fluorescence Microscopy

Microscopy was performed using a Nikon Eclipse Ti inverted microscope (Nikon Instruments, Melville, NY, USA) as previously described [69,90,92]. Briefly, brightfield images were captured using the Nikon DS-3 camera (Nikon Instruments, Melville, NY, USA), and fluorescence imaging in DAPI channel (350/405 nm, blue) and Cy5 channel (640/670 nm, far-red) was performed with the Photometrics CoolSnap MYO camera system (Photometrics, Tuscon, AZ, USA) under the control of Nikon NIS-Elements AR software (Nikon Instruments, Melville, NY, USA). Illumination for fluorescence imaging was provided by the X-Cite 120Q Widefield Fluorescence Microscope Excitation Light Source (Excelitas Technology, Waltham, MA, USA).

4.4.5 Sensitivity of PA Imaging of CFZ-HCl NP

The CFZ-HCl NPs were prepared for concentrations of 0, 0.001, 0.003, 0.01, 0.03, 0.1, 0.3, and 1 mg/mL. Each concentration was mixed with whole blood to generate a total of 10% blood by volume. 100 µL of each concentration was injected into a polyvinyl chloride tubing (*Z280348*, Sigma Aldrich, St. Louis, MO, USA). The portion of the tubing containing the CFZ-HCl NPs were submerged under water to allow for acoustic coupling with a 128-element ultrasound probe with frequency range of 7 to 15 MHz (CL15-7, Philips, Andover, MA, USA). The ultrasound probe was placed parallel to the longitudinal section of the tube and connected to a commercially available research ultrasound platform (Vantage 256, Verasonics, Redmond, WA, USA) for data acquisition. A tunable pulsed laser (Surelite OPO Plus, Continuum, Santa Clara, CA, USA) pumped by the third harmonic of an Nd:YAG laser (Surelite, Continuum, Santa Clara, CA, USA) was used to generate the PA signal. The laser has tunable wavelengths between 410–680 nm and 710–2500 nm,

a pulse duration of 5 ns, and a firing frequency of 10 Hz. The tube samples were imaged at a wavelength of 500 nm and averaged 20 times, with a total of 3 replicates performed.

4.4.6 CFZ-HCl NP Imaging via PA Multiple Wavelength Unmixing

The CFZ-HCl NPs were prepared for concentrations of 0, 0.003, 0.03, and 0.3 mg/mL, with the concentrations chosen based on the PA sensitivity results. An identical setup to the previous section was used with the exception that the tube samples were imaged at two wavelengths of 500 nm and 584 nm, and averaged 50 times. The wavelengths of 500 nm and 584 nm were chosen as these are the known isosbestic points of oxyhemoglobin (HbO_2) and deoxyhemoglobin (Hb), the two main chromophores in blood. The selection of the isosbestic points of blood prevented the need to distinguish between HbO_2 and Hb, allowing for the analysis of the total hemoglobin (THb) concentration instead. If blood and CFZ-HCl NPs are assumed to be the main chromophores generating the PA signal, the following matrix equation can be used to determine the concentrations of CFZ-HCl NPs and THb.

$$k\begin{bmatrix}\varepsilon_{THb@500nm} & \varepsilon_{CFZ-HCl\ NP@500nm}\\ \varepsilon_{THb@584nm} & \varepsilon_{CFZ-HCl\ NP@584nm}\end{bmatrix}\begin{bmatrix}[THb]\\ [CFZ-HCl\ NP]\end{bmatrix}=\begin{bmatrix}PA_{500nm}\\ PA_{584nm}\end{bmatrix} \quad \textbf{(4.1)}$$

Here, k is a constant dependent on the light fluence, the Grüneisen parameter of the sample, and the sensitivity of the imaging system. It is assumed that the light fluence, and subsequently k, is wavelength independent after calibration of the laser output energy. $PA_{\lambda nm}$ is the photoacoustic signal at λ nm, [THb] and [CFZ-HCl NP] are the concentrations of the total hemoglobin and CFZ-HCl NPs respectively, $\varepsilon_{THb@\lambda nm}$ and $\varepsilon_{CFZ\text{-}HCL\ NP@\lambda nm}$ are the optical extinction coefficients of hemoglobin and CFZ-HCl NPs at a wavelength of λ

nm respectively. Matrix equation 4.1 can then be rearranged to obtain the following matrix equation.

$$k\begin{bmatrix}[THb]\\[CFZ-HCl\ NP]\end{bmatrix}=\begin{bmatrix}\varepsilon_{THb@500nm} & \varepsilon_{CFZ-HCl\ NP@500nm}\\ \varepsilon_{THb@584nm} & \varepsilon_{CFZ-HCl\ NP@584nm}\end{bmatrix}^{-1}\begin{bmatrix}PA_{500nm}\\PA_{584nm}\end{bmatrix} \quad \textbf{(4.2)}$$

With the optical extinction coefficients being known, and $PA_{\lambda nm}$ being the PA signal measured, the right side of the matrix equation is completely known, allowing for the concentrations of [THb] and [CFZ-HCl NP] to be separately identified, albeit modified by the constant k. Hence, it should be noted that the concentrations measured are only relative concentrations, as an absolute concentration measurement would require a calibration measurement and the value of k to be identified, the latter of which is not a trivial task.

4.4.7 *Ex vivo* PA Imaging of Prostate Samples

The PA imaging setup is shown in Figure 4.1. The gelatin phantom was made using a concentration of 8 g/mL of gelatin from porcine skin (G2500, Sigma-Aldrich, St. Louis, MO, USA). The gelatin was poured into a mold to form a hollow cylindrical center and allowed to solidify. The prostate was placed in the center of the phantom, and 300 µL of PBS (pH 7.4) was added to submerge the prostate for acoustic coupling with the transducer. The gelatin phantom was placed on a calibrated rotating stage that allows for precise rotations of the gelatin phantom. The ultrasound transducer (CL15-7, Philips, Andover, MA, USA) was then placed perpendicular to the gelatin phantom at the height of the prostate sample. Ultrasound gel was added in between the transducer and the gelatin phantom for complete acoustic coupling. The ultrasound transducer was connected to a commercially available research ultrasound platform (Vantage 256,

Verasonics, Redmond, WA, USA) for data acquisition. A tunable pulsed laser (Surelite OPO Plus, Continuum, Santa Clara, CA, USA) pumped by the third harmonic of an Nd:YAG laser (Surelite, Continuum, Santa Clara, CA, USA) was used to generate the PA signal. A top illumination approach was used as the prostate sample was thinner on its z-axis, allowing for a more uniform laser energy distribution throughout the prostate sample. Fifty PA images were obtained at each angle, for two wavelengths of 500 nm and 584 nm, respectively. This was repeated for 9 angles, for a total of 180^{o} of rotation. The 50 images were then averaged, and a simple back-projection reconstruction was performed to obtain the final image at each wavelength. The PA imaging system's resolution is determined by the ultrasound transducer (CL15-7), with an approximately 226 μm lateral and 166 μm axial resolution at a depth of 6mm. However, due to the multiple angle imaging, the resolution is improved to the better of the two resolutions, at approximately 166 μm for both lateral and axial resolutions.

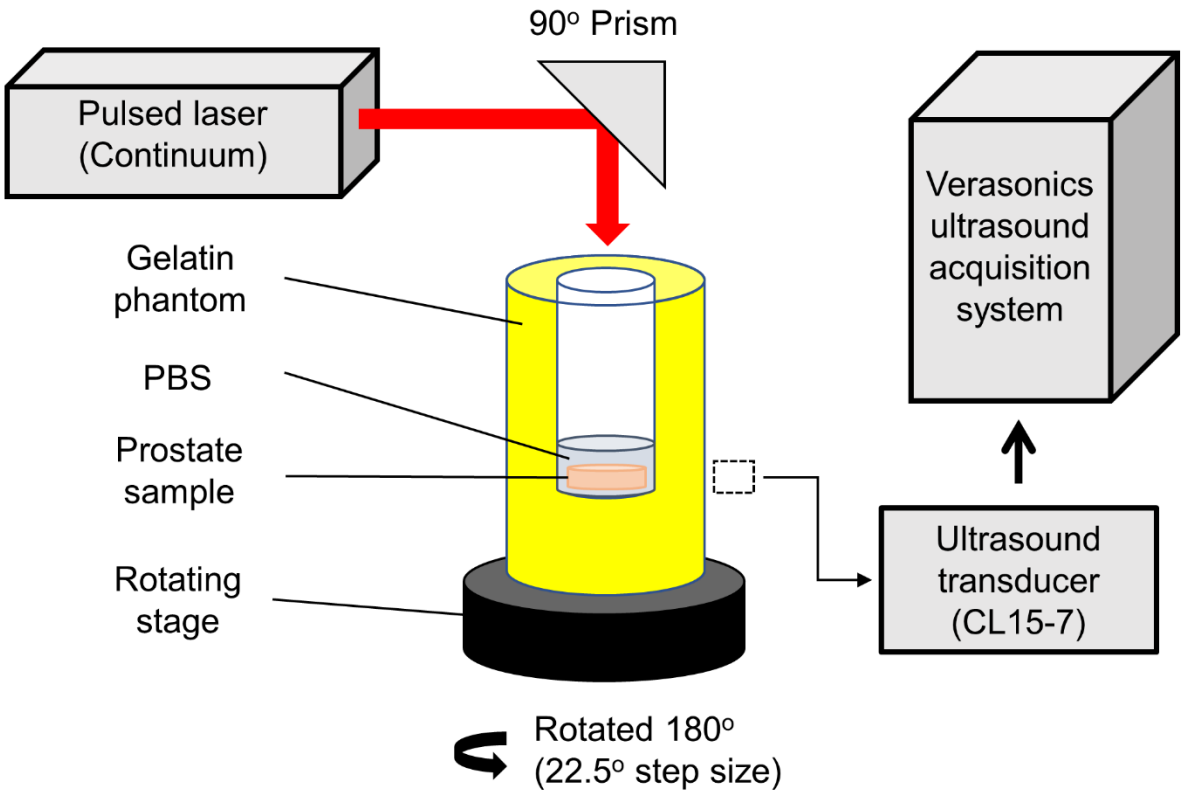

Figure 4.1 PA imaging setup for *ex vivo* prostate imaging. Dashed box indicates placement location of the ultrasound transducer (CL15-7).

The multiple wavelength unmixing algorithm previously specified was then performed to obtain the THb and CFZ-HCl NP relative concentrations. The CFZ-HCl NP signal was then normalized to the THb signal. This step was necessary as the prostate samples had different thicknesses and geometries, leading to different laser fluence distributions in the prostate samples depending on the imaging plane being measured. Mathematically, the constant "k" in matrix equations 4.1 and 4.2 is affected by this difference in laser fluences. However, by taking the ratio of CFZ-HCl NP/THb concentration, this constant is eliminated (with the assumption that k is wavelength-independent). This ensures that accurate comparisons can be made between prostate samples independent of their sizes. To obtain the final images, a number of image processing steps were taken. First, any

normalized CFZ-HCl NP signal with a corresponding THb signal below the background signal of the THb image was removed. Next, an upper threshold was applied to the normalized CFZ-HCl NP signal. These two steps were performed to remove any extreme normalized signals (i.e. very low THb signals results in extremely high normalized CFZ-HCl NP signals). A lower threshold was also applied to the normalized CFZ-HCl NP signal to remove the background CFZ-HCl NP signal and enhance the dynamic range of the images. Finally, the image was then smoothed with a Gaussian filter. The thresholds and filters applied were identical for all images.

4.4.8 Statistics

All statistical analysis was performed using Matlab R2015b (MathWorks, Natick, MA, USA). Where relevant, the data are expressed as the mean +/- standard deviation. Significant differences were determined using two-tailed two sample t-tests (ttest2 function) and a one-way analysis of variance (ANOVA) with Tukey's honest significant difference criterion (anova1 followed by multcompare function).

4.5 Results

4.5.1 CFZ-HCl NP Accumulation in Prostates

To determine CFZ-HCl NP accumulation in the prostates, the mice were divided into 3 groups. The first group consisted of TRAMP mice that were IV injected with the nanoparticle diluent to act as a negative control, and the second and third groups consisted of normal and TRAMP mice, respectively, that were IV injected with CFZ-HCl NPs. While CFZ is traditionally an orally fed drug, it requires several weeks of oral CFZ free base administration for a sufficient amount of drug to accumulate in the tissue

macrophages of various organs [90]. However, as a diagnosis technique, a shorter time frame would make it a more promising method for diagnosis of prostate cancer. Thus, a biomimetic formulation of CFZ-HCl NPs, which has been previously determined to be suitable for IV administration [69], allowed us to achieve a high accumulation of CFZ-HCl NPs in the cancerous prostates within 24 hours post injection.

HE stained sections of the TRAMP prostate (Figure 4.2A) showed that the mouse prostates were most likely in between the initial and advanced stages of adenocarcinoma, as the acinar lumens and interductal spaces were almost completely lost, even though the structure of each acinus remained intact [70]. The normal prostate showed a normal physiology with a uniform layer of epithelial cells comprising the glands (Figure 4.2B). From a quantitative drug analysis of the prostates from CFZ-HCl NP injected animals, we observed that there was a much larger CFZ-HCl NP accumulation in the TRAMP prostates than in the normal prostates (Figure 4.2C), verified by histopathology and fluorescence images. Furthermore, we did not observe any CFZ-HCl NP accumulation in the prostates of diluent injected TRAMP mice (Figure 4.2D) or in the prostates of CFZ-HCl NP injected normal mice (Figure 4.2E). However, there was clear accumulation of the CFZ-HCl NPs in the prostates of CFZ-HCl NP injected TRAMP (Figure 4.2F). These results supported the hypothesis that the IV injected CFZ-HCl NP has a greater accumulation in the TRAMP prostates than in the normal prostates.

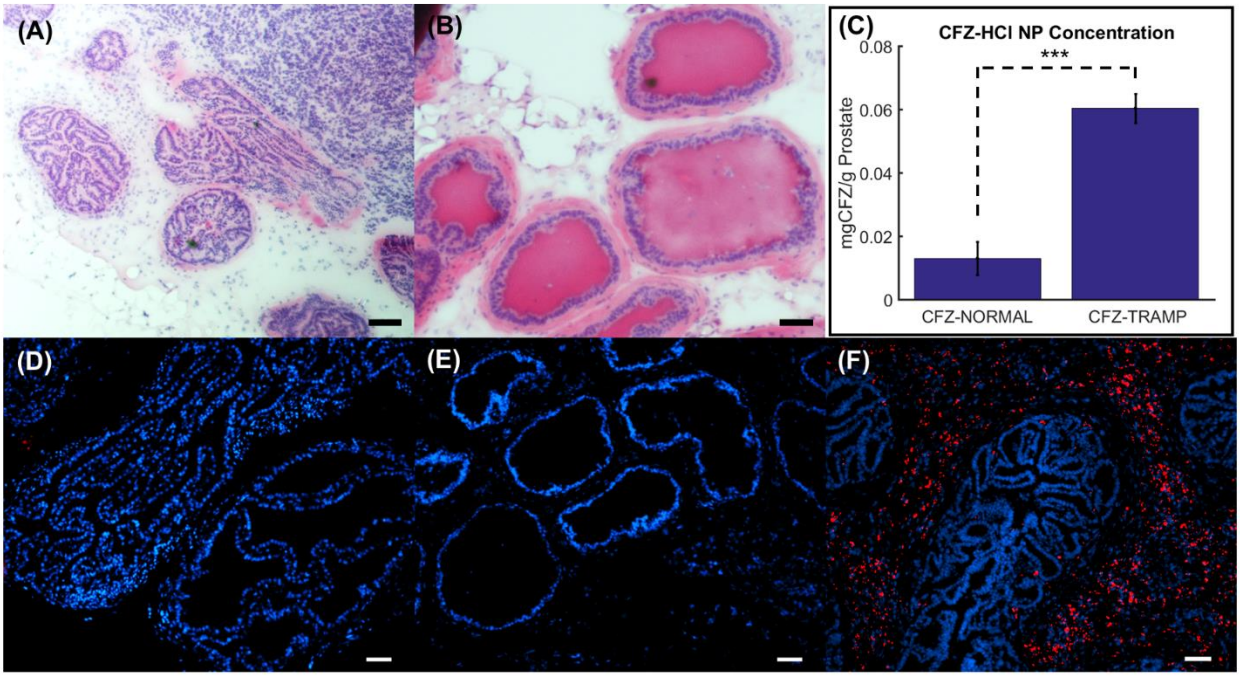

Figure 4.2 Histopathology and CFZ-HCl NP quantification in prostates. HE stained sections of the prostate for (A) TRAMP mice, and (B) Normal mice at 19 weeks. (C) Quantified concentrations of CFZ-HCl NPs in the two CFZ-HCl NP injected groups. Co-registered fluorescence images of the prostate with a nuclear stain (DAPI) in blue and CFZ-HCl NPs (Cy5) in red for (D) diluent injected TRAMP mice, (E) CFZ-HCl NP injected normal mice, and (F) CFZ-HCl NP injected TRAMP mice. Scale bar = 50 µm. *** p-value < 0.001.

4.5.2 Sensitivity of PA Imaging of CFZ-HCl NP

After confirming that the CFZ-HCl NP accumulated at a higher concentration in the prostates of TRAMP mice, we identified if this increased accumulation could be detected via PA imaging. Since one of the main concerns for detecting the CFZ-HCl NP was its potential overlap in absorption spectra with blood, specifically with HbO_2 and Hb (Figure 4.3A), we first tested the minimum detectable concentration of CFZ-HCl NP in the presence of blood. Here, a concentration of 10% blood by volume was used to mimic physiological conditions [2]. A wavelength of 500 nm was used because it was close to the peak absorption of CFZ-HCl NP, and it is also at a trough and isosbestic point of HbO_2 and Hb. By looking at the increase in PA signal amplitude at 500 nm with increasing CFZ-HCl NP concentrations, we were able to detect a change in PA signal with a concentration

of up to 3 µg/mL of CFZ-HCl NP (Figure 4.3B). Assuming that 1 g of the prostate organ has a volume of approximately 1 mL (with 1 g/mL being the density of water), CFZ-HCl NP was found to accumulate in the prostates of TRAMP mice with an average concentration of 60 µg/mL, as determined from the result in Figure 4.2C. This accumulation concentration is more than an order of magnitude above the detection threshold of 3 µg/mL. Hence, we concluded that the accumulation of CFZ-HCl NP in the prostates of TRAMP mice will be detectable via PA imaging.

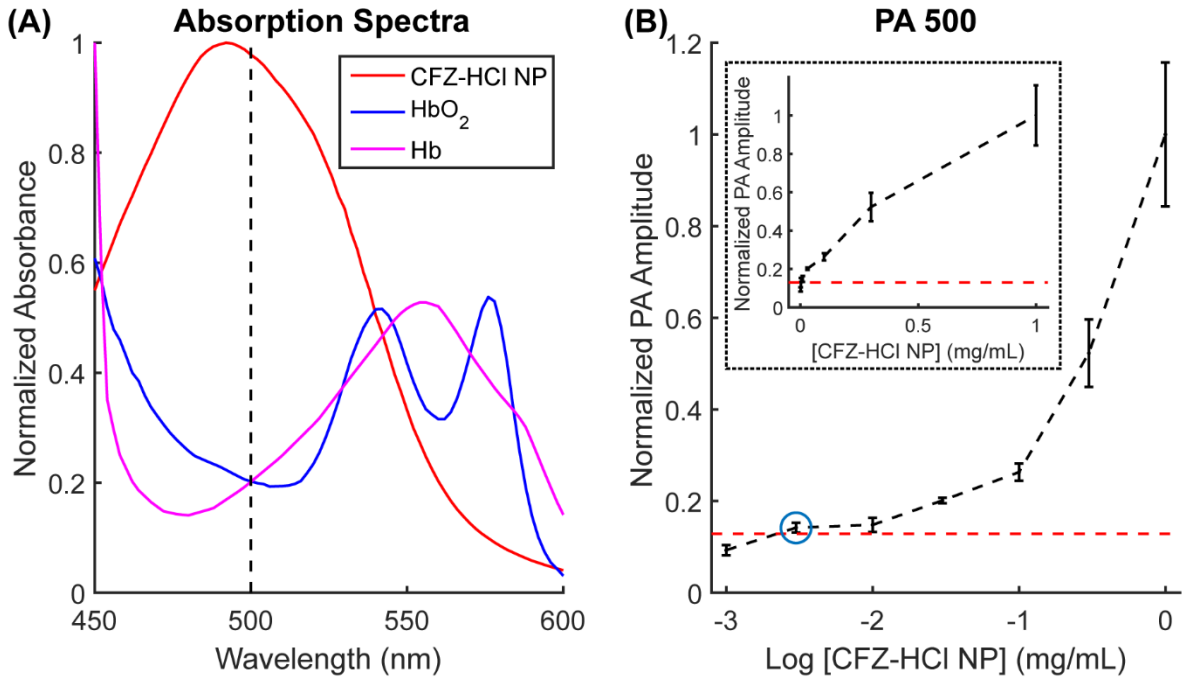

Figure 4.3 Absorption spectra and single-wavelength PA sensitivity of CFZ-HCl NP in the presence of 10% blood. (A) Overlaid absorption spectra of CFZ-HCl NP, HbO_2, and Hb. (B) Normalized PA amplitude at 500 nm for a sample with increasing [CFZ-HCl NP] in the presence of 10% blood on a logarithmic scale. Red dotted line indicates the minimum detection threshold based on the PA measurement on a sample of 10% blood in the absence of CFZ-HCl NP. Blue circle indicates the minimum detectable CFZ-HCL NP concentration of 3 µg/mL. (Inset) Normalized PA amplitude at 500 nm with increasing [CFZ-HCl NP] on a normal scale to show the approximate linearity between [CFZ-HCl NP] and the PA amplitude, at least up to a concentration of 0.3 mg/mL when signal saturation starts to occur.

4.5.3 CFZ-HCl NP Imaging via PA Multiple Wavelength Unmixing

Next, we verified if we would be able to distinguish the CFZ-HCl NP signal from the blood signal. To do this, we used the multiple wavelength unmixing method to decouple the CFZ-HCl NP signal from that of the blood. This method involves using multiple measurements at different laser wavelengths to isolate the contributions of each chromophore to the PA signal [16,46]. In this study, only two wavelengths were used to identify the individual contributions of CFZ-HCl NP and total hemoglobin. Here, we observed that the CFZ-HCl NP signal could be distinguished from the THb signal (Figure 4.4). This was demonstrated by the fact that we saw no change in the measured THb concentration after the deconvolution while the measured concentration of CFZ-HCl NP increased as expected. The blank solution (water) also showed very low THb and CFZ-HCl NP signals. However, there was a difference in the background relative signal of THb and CFZ-HCl NP which was attributed to the fact that the tubing used to hold the samples generates a small PA signal on its own, leading to some small systematic errors in the measurement. Hence, we demonstrated that the multiple wavelength unmixing method worked as intended.

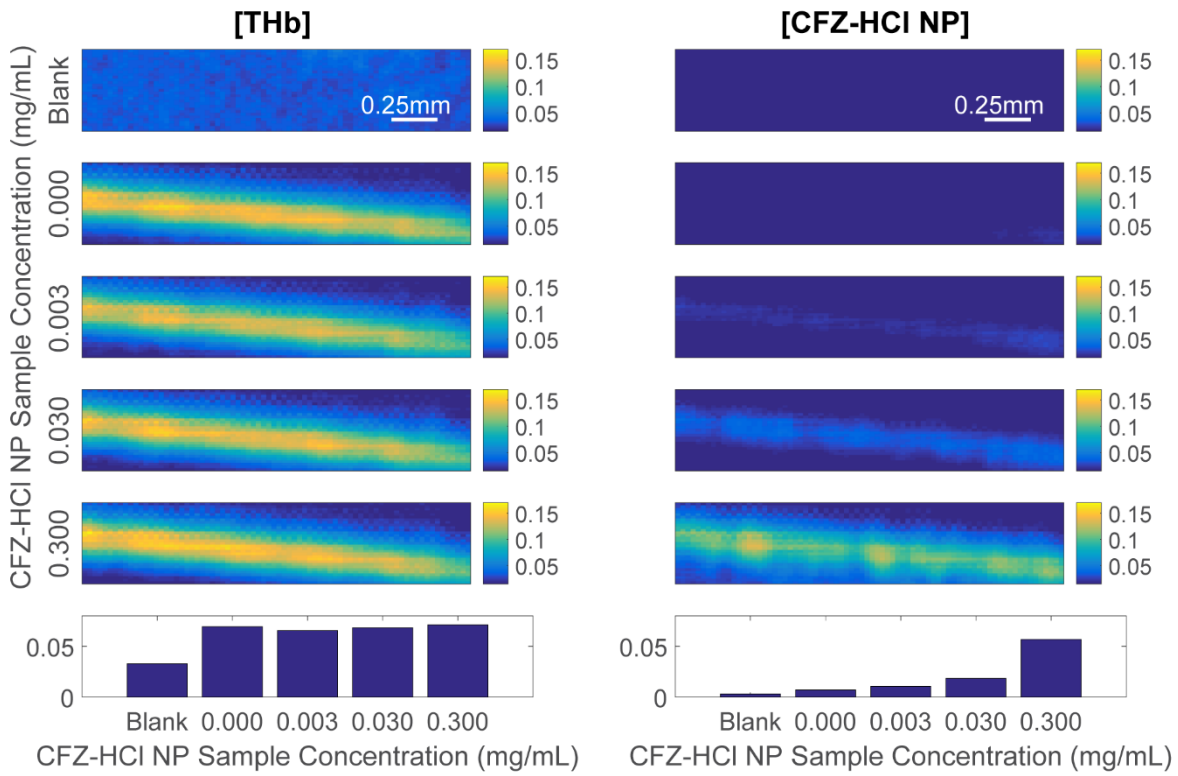

Figure 4.4 Two-wavelength unmixing of CFZ-HCl NP from blood. A mixture of different concentrations of CFZ-HCl NP (shown on the y-axis) with 10% blood by volume in a tube was used. The two columns indicate the isolated contributions of THb and CFZ-HCl NP to the PA signal for each sample. Color bars only indicate the relative concentrations and not the actual concentrations. The last row shows the quantified relative concentrations for all the samples. “Blank” indicates a tube filled with water.

4.5.4 *Ex vivo* PA Imaging of Prostate Samples

After validating that decoupling the contributions of CFZ-HCl NP and blood could be achieved by multiple wavelength unmixing via the experiment on tube samples, we then performed ex vivo PA imaging of the mouse prostates. Here, we compared the same 3 groups of mice shown in Figure 4.2. Figures 4.5A-C show the normalized CFZ-HCl NP signal over the blood signal for representative prostates in the 3 separate groups. The CFZ-HCl NP signal was normalized to the blood signal to help reduce any inaccuracies due to the difference in size of the prostates, as detailed in the methods. Figure 4.5D shows the normalized mean CFZ-HCl NP signal to the mean THb signal for all the

prostates in each of the 3 groups. We observed that there was a significantly higher CFZ-HCl NP signal in the prostates of CFZ-HCl NP injected TRAMP mice compared to the other two groups, which matched the results shown in Figure 4.2. Furthermore, there was no significant difference between the diluent injected TRAMP prostates and the CFZ-HCl NP injected normal prostates. Thus, we demonstrated that PA imaging can be used to detect the differences in accumulation of CFZ-HCL NPs in the prostates in an ex vivo setting.

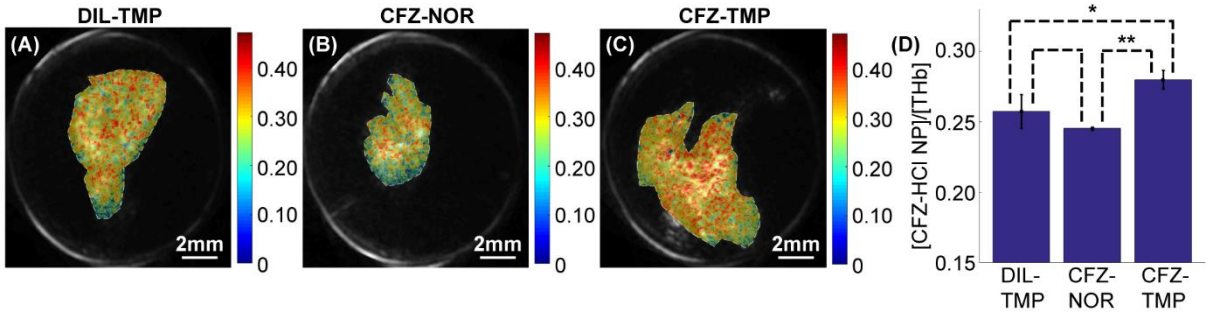

Figure 4.5. Ex vivo PA imaging results. CFZ-HCl NP signal normalized to the THb signal for prostates of (A) diluent injected TRAMP mice (DIL-TMP), (B) CFZ-HCl NP injected normal mice (CFZ-NOR), and (C) CFZ-HCl NP injected TRAMP mice (CFZ-TMP). Color bars indicates the CFZ-HCl NP signal normalized to the THb signal as determined by the two-wavelength unmixing. (D) Mean normalized CFZ-HCl NP signal for each group within the organ boundaries as delineated by the US image (shown in the representative images as a white dotted line). * p-value < 0.05, ** p-value < 0.01.

4.6 Discussion

While the multiple wavelength unmixing technique helps to mitigate the interference of endogenous chromophores, it is not a perfect technique, and there will always be background noise from chromophores that are not accounted for in the algorithm. For example, the imaging results in Figure 4.5 showed a strong background signal for CFZ-HCl NP in the absence or low concentration of the drug. In addition, there appeared to be a slightly higher CFZ-HCl NP signal in the DIL-TMP group compared to the CFZ-NOR group, in contrast with the histology results where the reverse was true. Unlike the

samples used in Figure 4.4, other chromophores such as myoglobin (and its many different forms) could also be present in the prostate, contributing to some inaccuracies in the CFZ-HCl NP signal. If these chromophores could be identified and accounted for, with more PA measurements made at additional wavelengths, the sensitivity of the PA imaging technique towards CFZ-HCl NP could be improved. In addition, the fluence distribution in the prostate tissues is assumed to be wavelength-independent, which is typically a good assumption for near-surface PA imaging, less so with increasing imaging depth [16,25]. Addressing these two limitations in the current approach would improve the sensitivity of PA imaging towards the detection of CFZ-HCl NP, allowing for even more precise and accurate detection. The ability to detect and distinguish smaller concentrations of CFZ-HCl NP will allow for many new possibilities using this technique, such as the study of prostate cancer progression in its early stages, where CFZ-HCl NP accumulation in the prostate is expected to be small. Additionally, there are concerns that normalization of the CFZ-HCl NP to the THb signal would reduce the sensitivity of PA imaging to detect CFZ-HCl NPs due to increasing vasculature in the prostate tumor with cancer progression. While this may be true, we believe that the difference in accumulation of CFZ-HCl NPs between cancerous and non-cancerous prostates (as shown in Figure 4.2C) will far outweigh any variations in tumor vasculature.

It should also be noted that there are other PA contrast agents that can be used in the near-infrared spectrum range (e.g. indocyanine-green and gold nanorods) [14,15], which would lead to less endogenous chromophore interference. However, none of them come with the intrinsic benefit of CFZ-HCl NP, which specifically accumulates in tissue macrophages without the need for external targeting agents. Since TAMs are prevalent

in most forms of cancer, this drug could potentially be used in the diagnosis of other forms of cancer as well. Furthermore, most of the other contrast agents are not clinically approved and are still limited to the research field [14]. CFZ, on the other hand, is an FDA-approved drug with minimal harmful side-effects [90], which makes it more likely to be translated for clinical use. Therefore, we expect the benefits of using CFZ-HCl NP as a diagnostic contrast agent to outweigh the higher signal interference with endogenous chromophores compared to other known contrast agents.

Besides the limitations mentioned above, there are also other challenges for translating this into a practical probe for in vivo monitoring of prostate cancer development and staging, such as the imaging depth needed for imaging prostates in vivo due to the prostate's anatomical location both in animals and humans. Due to the CFZ-HCl NPs low absorption wavelength, deep imaging depths with the nanoparticle may be limited. However, there is ongoing research in this field, where potential solutions to this include the development of a minimally invasive needle-based PA imaging system that can be inserted close to the prostate [68,93-95]. This helps to bring both the light source and ultrasound transducer close to the prostate, significantly reducing the absorption of the light signal from other chromophores as well as the attenuation of the ultrasound signal in the body.

In conclusion, we have shown that IV injected CFZ-HCl NP accumulates at a higher concentration in cancerous prostates than in normal prostates within 24 hours post injection in a TRAMP mouse model. In the presence of blood, one of the main endogenous chromophores in the body, we were able to isolate the signal of CFZ-HCl NP using two-wavelength unmixing PA imaging. Furthermore, we were able to apply this

technique in PA imaging to detect the higher accumulation of CFZ-HCl NP in the cancerous prostates compared to the normal prostates. Hence, we believe that differences in the interaction of CFZ-HCl NP with normal vs cancerous prostates, together with PA imaging, could lead to the development of a noninvasive technique for the detection and monitoring of prostate tumor induction and progression in an animal model of the disease, while providing useful information to facilitate the design of next generation imaging probes for the development of noninvasive diagnosis and staging of prostate cancer in humans.

CHAPTER 5

In Vivo Photoacoustic Potassium Imaging of the Tumor Microenvironment

5.1 Brief Foreword

This chapter focuses on the photoacoustic chemical imaging method for potassium imaging in *in vivo* small animal models. At the time of writing, the work shown here is currently being submitted for publication in a peer-reviewed journal.

5.2 Abstract

The accumulation of potassium (K^+) in the tumor microenvironment (TME) has been recently shown to inhibit immune cell efficacy, and thus immunotherapy. Despite the abundance of K^+ in the body, few ways exist to measure it *in vivo*. To address this technology gap, we combine an optical K^+ nanosensor with photoacoustic (PA) imaging. The nanosensor is based on a solvatochromic dye whose absorption spectrum shifts as a function of K^+ concentration. Using multi-wavelength deconvolution, we are able to separate this nanosensor's signals from those of the background chromophores, allowing for quantitative evaluation of K^+ concentration. We imaged K^+ concentrations in healthy muscle vs. tumor tissue in a mouse model. Significantly elevated K^+ levels were found in the TME, with an average concentration of approximately 29 mM, compared to 19 mM

found in muscle. These PA measurements were confirmed by extraction of the tumor interstitial fluid and subsequent measurement via mass spectrometry.

5.3 Introduction

Potassium (K^+) is the most abundant cation in the body [96]. The evolution of live cells started by keeping Na^+ out of and K^+ inside the cell [97,98]. Steep gradients exist in its distribution as intracellular K^+ concentrations are typically greater than 100 mM [96,99], while extracellular K^+ concentrations are approximately 5 mM [96], It has long been known that the tumor microenvironment (TME) can have suppressive effects on T cells [100]. However, this suppression was only recently attributed to disruptions in the K^+ concentration [101]. Notably, necrotic cell death in the nutrient-starved core of tumors leads to the release of vast quantities of intracellular K^+. The release of this K^+ induces local *hyperkalemia* in the TME with a reported 5-10 fold increase in K^+ concentration [101]. In two seminal studies, Eil and colleagues determined that elevated K^+ suppresses T cell effector function and prevents immune cells from maturing [101,102].

Despite the importance of K^+ in the body, there exist only a few ways to measure K^+ concentrations *in vivo*. Magnetic resonance imaging (MRI) has been used in the past to measure *in vivo* K^+ concentrations [103-105]. However, the ^{39}K MRI imaging is an expensive technique, and is limited by availability and especially by poor resolution (voxel size of ~1 mL) [103]. Few commercially available potassium-sensitive dyes exist (PBFI, asante-green series), and of these none are excitable in either the near- or far-infrared. Visible wavelength dyes for fluorescence imaging are ill-suited for *in vivo* experiments due to the severe scattering of light in biological tissue. Miniaturized electrodes, the gold standard in ion measurement, are inherently invasive and unable to capture finely resolved spatial

and temporal ion distribution images. It is of note that, in the previously mentioned immunological studies, K^+ was measured by centrifuging *ex vivo* tumors to collect tumor interstitial fluid [101,106], which was then measured via electrode, thus losing any spatiotemporal resolution.

To generate structural images that contain the chemical information in biological samples, we recently developed photoacoustic chemical imaging (PACI). PACI benefits on one hand from the good sensitivity of the optical detection techniques and on the other hand from the lower tissue scattering and thus excellent penetration and spatial resolution of ultrasound imaging [107,108]. PACI utilizes exogenous contrast agents, typically nanosensors, whose optical absorption properties change in response to some analyte of interest. The advantages of PACI have already allowed the monitoring of lithium treatments for bipolar disorder [18], measuring of tissue oxygenation using a lifetime-based approach [17,19-22], and measuring of tumor pH [16].

In this study, we extend PACI through the use of an ionophore-based optical K^+ nanosensor. While we have previously developed a K^+ sensor for PACI, it had a cross-sensitivity with pH due to its reliance on a pH dye as part of its sensing mechanism [41]. Hence, its accuracy would be affected by the acidic tumor microenvironment. As such, we adopted a pH-insensitive K^+ sensor for *in vivo* PACI measurements of K^+. Invented by Eric Bakker's group, this optode formulation utilizes positively charged, solvatochromic dyes which are pushed from the hydrophobic interior of the nanoparticle to its hydrophilic surface [109]. The transition between the interior and exterior of the nanoparticle forces a change in the dye's optical absorption spectrum which can be measured by PA imaging. The solvatochromic dye based K^+-sensing nanoparticle (SDKNP) is directly injected into

subcutaneous tumors in mice, where its signal is deconvoluted from that of blood. This method could be extended to measuring other ions, such as Na^+ and Cl^- [110-112]. Specifically, here we demonstrate its utility by documenting *in vivo* the high overall concentration of K^+ in tumor tissue compared to that in healthy muscle, and quantitatively verifying PACI results using mass spectroscopy measurements on the interstitial fluid harvested from each tumor.

5.4 Methods

5.4.1 Materials

Millipore water was used for all syntheses and buffer preparations. Chemicals purchased from Sigma-Aldrich (St. Louis, Mississippi, USA) include Pluronic F-127, valinomycin, dioctyl sebacate, sodium tetrakis[3,5-bis(trifluoromethyl)phenyl]borate, potassium chloride, sodium chloride, calcium chloride dihydrate, magnesium chloride, 3-(N-morpholino)propanesulfonic acid, acetonitrile, acetic anhydride, 1-iodooctadecane, 2-methylbenzothiazole, (dimethylamino)cinnamaldehyde, sodium iodide, and methanol.

5.4.2 SD2 Synthesis

Synthesis of SD2 was first reported by Eric Bakker's group, and few changes were made to the original protocol [109]. Briefly, 1.5 g 2-methylbenzothiazole and 3.8 g 1-iodooctadecane were dissolved and refluxed in acetonitrile for 24 hours. The solution was removed from heat and allowed to solidify. The crude product was precipitated in diethyl ether, collected, and washed several times in diethyl ether. 265 mg of this product, along with 122 mg (dimethylamino)cinnamaldehyde, was then dissolved in acetic anhydride and refluxed for 20 minutes. The reaction solution was then poured into a warm solution of 10

mM sodium iodide (in Millipore water). The dark purple precipitate was washed several times with water, dried, and collected.

5.4.3 Nanoparticle Synthesis

The protocol for the synthesis of the SDKNP was developed by Eric Bakker's group.[109] To generate a concentrated solution of nanoparticles, the following protocol was used. 0.2 mg SD2 (synthesized in house, see above), 0.9 mg sodium tetrakis[3,5-bis(trifluoromethyl)phenyl]borate, 1.2 mg valinomycin, 5 mg Pluronic F-127, and 8.75 μL (8 mg) dioctyl sebacate were dissolved in 3 mL of methanol. The methanol cocktail was then injected into 30 mL of Millipore water under vigorous stirring. The surface of the methanol-water mixture was blasted with nitrogen gas for 1 hour to remove the methanol. The nanoparticle solution was concentrated to the desired concentration using an Amicon Ultra-15 centrifuge filter (100k Da).

5.4.4 Mass Spectrometry – Solvatochromic Dye Characterization

Electrospray ionization mass spectrometry was performed by the University of Michigan's Mass Spectrometry Core.

5.4.5 DLS and Zeta-Potential

Dynamic Light Scattering and Zeta-Potential measurements were performed at a nanosensor concentration of 1 mg/mL using a Beckman Coulter analyzer.

5.4.6 MTT

HeLa cells (ATCC authenticated) were cultured in Dulbecco's Modified Eagle Media with 10% fetal bovine serum and 1% penicillin/streptomycin. 100,000 cells were plated on a

24 well plate and allowed to grow over night in 1 mL of growth media. SDKNPs were incubated for various times at a concentration of 1 mg/mL. Following incubation, 500 μL of incubation media was replaced with 500 μL of MTT solution (5 mg/mL in PBS) and incubated for 4 hours. Once finished, all media was removed from the wells and replaced with 1 mL of DMSO. This solution was then incubated for 1 hour at which point the solution was removed and its absorption spectrum measured in a UV-Vis spectrophotometer. Absorption peaks at 590 nm were compared, and all samples were repeated 4 times.

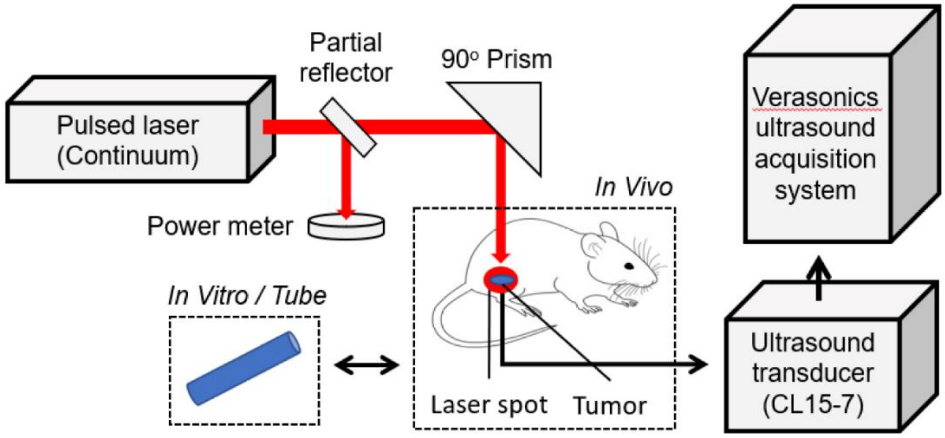

Figure 5.1 General PA setup for *in vitro* and *in vivo* imaging. For acoustic coupling, *in vitro* tube experiments were conducted in water, while *in vivo* mice experiments were conducted using ultrasound gel. A partial reflector (glass slide) was used to reflect part (<20%) of the laser beam energy to the power meter for energy monitoring. The PA signal was acquired using an ultrasound transducer (CL15-7) connected to a research ultrasound acquisition system (Vantage 256, Verasonics, Kirkland, WA, USA).

5.4.7 PA and UV Calibration

For the UV calibration, K^+ calibration samples of 0, 1, 5, 10, 20, 30, 50, 70, 100, and 150 mM K^+ with 1 mg/mL of SDKNP were prepared. Samples were prepared in pH 7.4 MOPS-buffered saline solution containing physiologically relevant concentrations of interfering cations: sodium (150mM), magnesium (1mM), and calcium (2.6mM). The absorption spectrum for each sample was obtained for a range of 400-800 nm using a Shimadzu

1600 UV-Vis Spectrophotometer (Shimadzu, Kyoto, Kyoto, Japan). For the PA calibration, K^+ calibration samples of 0, 1, 5, 10, 20, 30, 40, 50, 70, 100, and 150 mM K^+ with 10 mg/mL of SDKNP were prepared. 75 µL of each sample was added into a transparent PVC tubing. The tube samples were submerged in water for acoustic coupling. The tube samples were then imaged using a PACI system consisting of a tunable pulsed laser (Continuum, Santa Clara, CA, USA) and a 128-element ultrasound probe with frequency range of 7 to 15 MHz (CL15-7, Philips, Andover, MA, USA). The tunable pulsed laser pumped by the third harmonic of an Nd:YAG laser (Continuum, Santa Clara, CA, USA), has a pulse duration of 5 ns, a firing frequency of 10 Hz, and is capable of achieving wavelength tuning in the range of 410-680 nm and 710-2500 nm. The ultrasound probe was then connected to a commercially available research ultrasound platform (Vantage 256, Verasonics, Kirkland, WA, USA) for data acquisition. The general PA imaging setup is shown in Figure 5.1. The PA signal was obtained for 6 wavelengths of 545, 560, 576, 584, 605, and 625 nm, chosen based on the absorption spectra obtained. Each PA signal was averaged 20 times, with a total of 4 replicates performed for each sample. A simple light fluence correction was performed where the PA signal was normalized to the average energy measured for each wavelength using a power meter (Newport, Irvine, CA, USA).

5.4.8 PA Multi-Wavelength Unmixing

An identical setup to the PA calibration experiment was performed. K^+ samples of 2, 5, 20, 40, 50, and 150 mM were prepared in the presence of 1% blood v/v and 10 mg/mL of SDKNP as well as a blank sample which only contained saline solution. PA imaging was conducted for 6 wavelengths of 545, 560, 576, 584, 605, and 625 nm. The wavelengths

were chosen based on the isosbestic points and maximal difference in the extinction coefficients of SDKNP and hemoglobin. Multi-wavelength unmixing was performed according to the following steps. Firstly, at each wavelength, the PA signal can be modelled as shown in Eq. 5.1.

$$PA_{\lambda} = k([SDKNP]\varepsilon_{SDKNP}(\lambda, K^{+}) + [HbO_2]\varepsilon_{HbO_2}(\lambda) + [Hb]\varepsilon_{Hb}(\lambda)) \quad \textbf{(5.1)}$$

where λ is the wavelength in nm, [SDKNP] is the SDKNP concentration, [HbO_2] is the oxyhemoglobin concentration, [Hb] is the deoxyhemoglobin concentration, ε is the extinction coefficient, and k is a constant associated with multiple parameters such as light fluence, the Grüneisen parameter of the sample, and the sensitivity of the imaging system. It should be noted that ε_{SDKNP} is dependent on both λ and the K^+ concentration.

The extinction coefficients of Hb and HbO_2 for each λ are known values, while the extinction coefficient of SDKNP can be measured at each λ and for a range of K^+ values. Here, we measured the value of ε_{SDKNP} for K^+ values of 0, 1, 5, 10, 20, 30, 40, 50, 60, 70, 80, 90, 100, 125, 150, and 200 mM using a UV-VIS spectrophotometer. This left only 4 unknowns in the above equation, specifically [SDKNP], [HbO_2], [Hb], and [K^+]. Using simple linear algebra, the 4 unknowns can be solved by making at least 4 separate measurements at different wavelengths. Here, we used 6 wavelengths to solve the linear equations for increased accuracy, as it is widely known that additional measurements can help to improve the accuracy of the unmixed results [23,27,28]. A notable limitation to this technique is that the estimation of the [K^+] is based on measurements of the extinction coefficient of the SDKNP at discrete K^+ values, meaning that the values of the measured K^+ are always limited to those discrete K^+ values. An alternative to this is to model the

ε_{SDKNP} response to K^+ by using an equation-based approach. This approach, while allowing for continuous K^+ estimates, has its own drawbacks in that no simple equation model can perfectly capture the ε_{SDKNP} response to K^+, meaning that approximations will have to be made, reducing the accuracy of the measurements.

5.4.9 *In Vivo* PACI of K^+

Animal care was provided by the Unit for Laboratory Animal Medicine (ULAM), and all procedures on live animals were performed in accordance with institutional guidelines and approved by the Institutional Animal Care and Use Committee (IACUC) at the University of Michigan. A total of 6 mice were used in the *in vivo* imaging experiment. To generate the subcutaneous tumors, approximately $1x10^6$ 9L glioma cells (ATCC, Manassas, VA, USA) in 0.1 mL of RPMI 1640 (Gibco, Waltham, MA, USA) was subcutaneously injected into the right flank of 5-week old nude mice (Envigo, Huntingdon, Cambridgeshire, UK). The tumors were allowed to grow till a size of approximately 1 cm in diameter. 0.05 mL of 10 mg/mL SDKNP was then locally injected into the tumor, followed by PA imaging immediately after the injection. This was repeated with the thigh muscle on the opposite flank, where 0.05 mL of 10 mg/mL SDKNP was locally injected in the thigh muscle, followed by PA imaging immediately after the injection. All PA imaging was conducted for the same 6 wavelengths of 545, 560, 576, 584, 605, and 625 nm, with a total of 80 averages per image. A simple light fluence correction was performed where the PA signal was normalized to the average energy measured for each wavelength using the power meter. Multi-wavelength unmixing was conducted according to the same protocol as previously mentioned with the exception that only K^+ values between 0-125 mM were analyzed. This range was chosen to reflect the expected biological range of the

extracellular tumor K^+. After the imaging, the mice were euthanized, and the tumor harvested. An adaptation of the protocol performed by Eil *et al*. was conducted to collect the extracellular fluid from the tumor. Briefly, the tumor was first flushed with saline to remove surface blood and blotted gently with Kimwipe (Kimberly-Clark, Irving, TX, USA) to dry. The tumor then was placed in a SpinX centrifuge tube filter (Corning, New York, NY, USA) and centrifuged at increasing speeds of 1000, 2000, 4000, and 8000 RPM for 10 minutes each [106]. Approximately 4-10 µL of extracellular fluid was collected per tumor. The extracellular fluid was then sent for inductively coupled plasma mass spectroscopy.

5.4.10 Inductively Coupled Plasma Mass Spectroscopy

Tumor interstitial fluid was diluted with Millipore water by a factor of 5000 prior to measurement with a Perkin-Elmer Nexion 2000 ICP-MS (Perkin-Elmer, Waltham, MA, USA). The machine was calibrated using standards prepared at 50, 100, 250, 500, and 750 PPB K^+ using potassium chloride as a source for K^+ ions.

5.4.11 Statistical Analysis

All statistical analysis was performed using Matlab 2016a (MathWorks, Natick, MA, USA). Where relevant, the data are expressed as the mean +/- standard deviation. Significant differences were determined using two-tailed two sample t-tests (*ttest2* function).

5.5 Results

To test the capabilities of the SDKNP for PACI of K^+, we first compared the response of the SDKNP to K^+ using both PACI and UV-Vis spectrophotometry. Figure 5.2a shows the absorption spectra obtained for SDKNP at various K^+ levels. The largest absorption change occurred at 605 nm for the changing K^+ concentrations, with a small opposite

trend at around 545 nm. The isosbestic point of the SDKNP is at approximately 560 nm. Making use of these wavelength ranges, the PA and UV-Vis calibration ratios were plotted in Figures 5.2b-f. These calibration ratios show the changes in the PA and the UV-Vis signals with respect to the isosbestic point for increasing concentrations of K^+. As the PA signal of a molecule is directly proportional to its absorption, the PA calibration is expected to match that of the UV-Vis calibration. To show the good agreement between the PA and UV-Vis measurements, the ratios are co-plotted in Figures 5.2b-f to show the similarity between the ratios measured by both modalities. These ratios generally showed a signal decrease with increasing K^+ concentration, with exception of the 545nm/560nm ratio. The SDKNP is most sensitive between 0-50 mM K^+, an ideal range for the expected *in vivo* tumor K^+ concentration. Based on these results, we used the UV-Vis spectrophotometer measurements for later calibrations, as they generally provided measurements with very low noise levels.

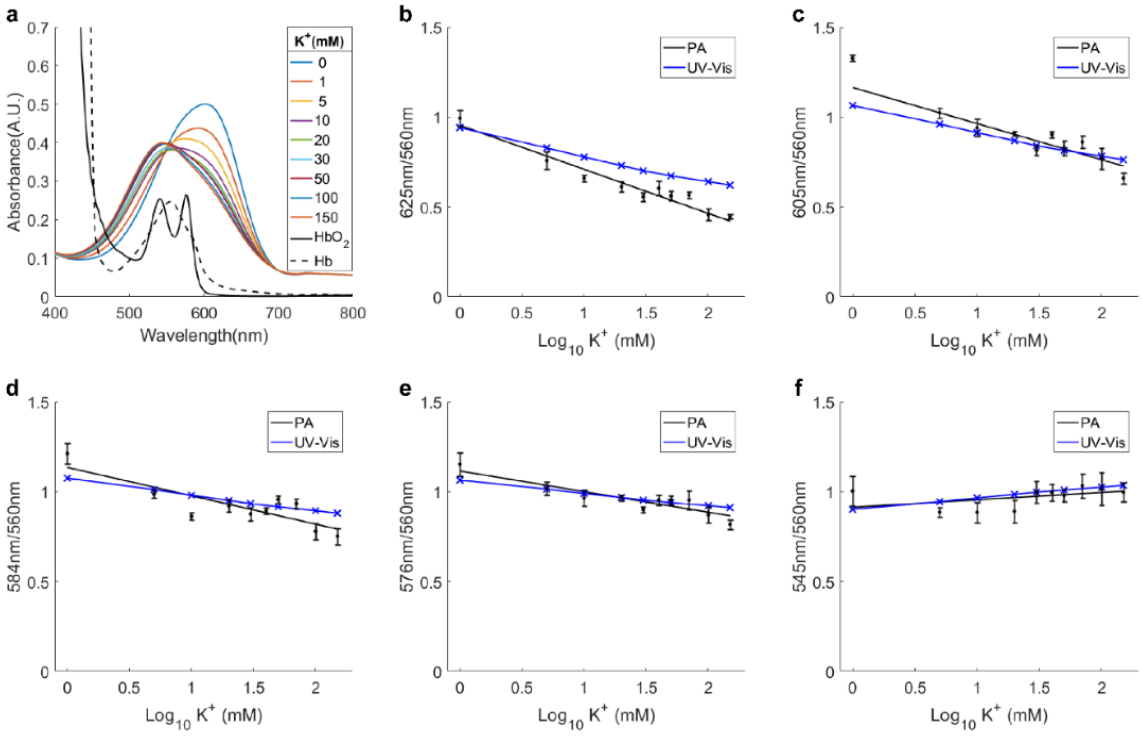

Figure 5.2 Absorption spectra and PA K^+ calibrations compared to UV-Vis K^+ calibrations. (a) Absorption spectra of SDKNP for various K+ concentrations, oxyhemoglobin (HbO_2), and deoxyhemoglobin (Hb). PA and UV-Vis ratio measurements for (b) 625nm/560nm, (c) 605nm/560nm, (d) 584nm/560nm, (e) 576nm/560nm, and (f) 545nm/560nm. There is excellent agreement between the PA and UV-Vis calibrations.

Next, we analyzed the capability of separating the SDKNP signal from the expected *in vivo* endogenous chromophores of deoxyhemoglobin (Hb) and oxyhemoglobin (HbO_2). While other chromophores such as melanin and water are also present in biological tissue, Hb and HbO_2 are expected to be the major PA signal contributors within the 545-625 nm wavelength range in the tumor. Using a similar setup as the calibration experiment, multi-wavelength unmixing was performed for various K^+ samples in the presence of 1% blood v/v. This volume of blood was used as it is close to the estimated blood volume fraction in a tumor tissue (for breast cancer) [2]. Using a 6-wavelength unmixing technique, the concentrations of K^+, SDKNP, Hb, and HbO_2 were identified with the results shown in Figure 5.3. The Hb and HbO_2 concentrations were then combined,

as the oxygenation of the sample was not controlled and the total hemoglobin (THb) concentration was expected to serve as a more precise measurement. Within the SDKNP's sensitivity range of 0-50 mM, the unmixed measurements of K^+ concentration showed good accuracy levels (+/- 5 mM), with exception of the 20 mM sample. Outside this range, the measurement accuracy drops rapidly, although qualitative increases can be observed, as is shown by the significantly lower PACI estimate of 76 mM for the 150 mM K^+ sample. There is also some noticeable bleed through of the SDKNP and blood signals at higher K^+ concentrations. This is most likely due to the absorption spectra of the SDKNP being more similar to blood at higher K^+ concentrations, especially that of deoxyhemoglobin (Figure 5.2a). It should be noted that this does not affect the K^+ measurement significantly, as most of the error is localized in the [SDKNP] and [THb] measurements. Finally, the blank sample showed almost no detectable signal throughout, as expected.

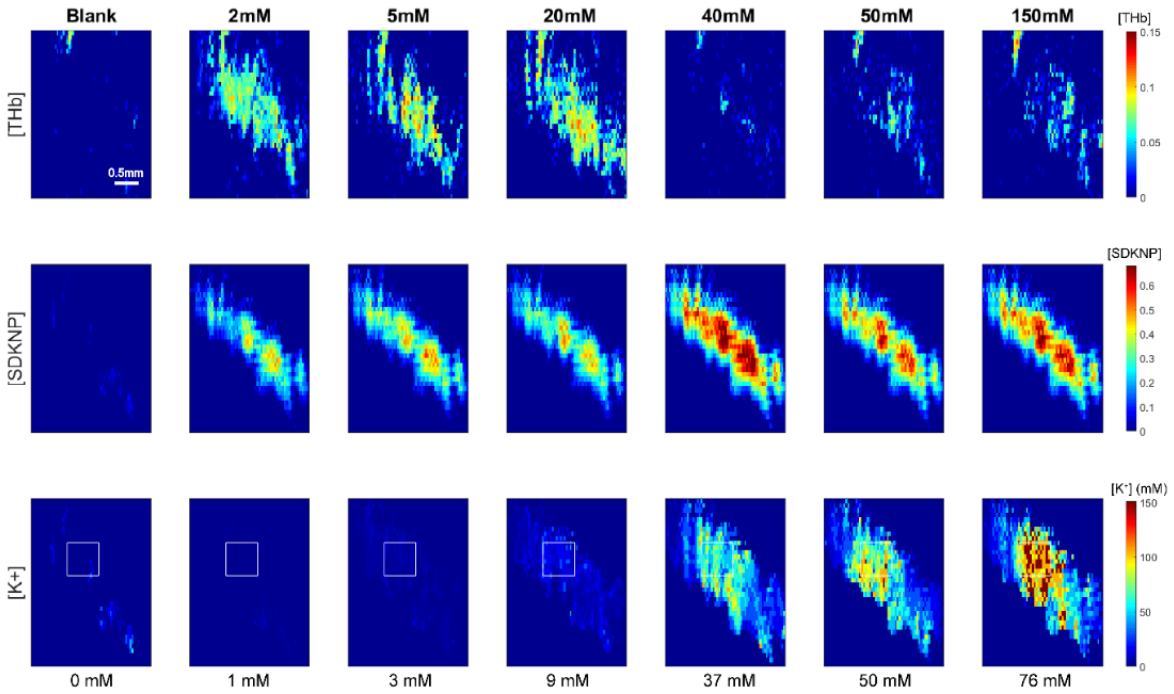

Figure 5.3 PA multi-wavelength unmixing for SDKNP samples in a tube for determining total hemoglobin concentration ([THb]), SDKNP concentration ([SDKNP]), and K^+ concentration ($[K^+]$). All samples contain SDKNP and 1% blood v/v at the specified K^+ concentrations, with exception of "Blank", which only contains saline solution. Sample values of K^+ are provided at the top of the figure, while the measured values obtained via deconvolution are given at the bottom of the figure. Measured values pertain to the average K^+ in the region of interest outlined by the white box.

After verifying the ability to measure the K^+ signal *in vitro* in the presence of blood, we then tested the ability to perform *in vivo* measurement of K^+ in a subcutaneous tumor mouse model. We locally injected 0.05 mL of 10 mg/mL SDKNP into the tumor and the thigh muscle of the mice before conducting PACI at the 6 wavelengths. Figure 5.4a shows an example of the map of oxygen saturation, SDKNP concentration, and K^+ concentration in the tumor and the muscle as measured by PA multi-wavelength unmixing for an individual mouse. Figure 5.4b shows the average hemoglobin oxygen saturation across all mice (n=6). While there is a slight decrease in the average tumor hemoglobin oxygen saturation compared to the muscle (47.5% compared to 52.3%), it was not statistically significant in this study. Figure 5.4c shows the average SDKNP concentration across all mice, where there was no significant difference detected between the tumor and the muscle (0.024 vs 0.024 A.U.). As equal concentrations of SDKNP were injected into the tumor and the muscle, this result was expected. Figure 5.4d shows the average K^+ concentration between the tumor and the muscle, where the tumor K^+ was significantly higher than the muscle K^+. We observe an average K^+ concentration of 29 mM (range of 22-49 mM) in the TME, as expected from the predicted 5-10 fold increase report by Eil *et al* [101]. In the muscle samples, we see an average concentration of 19 mM (range of 14-24 mM), which is higher than naively expected.

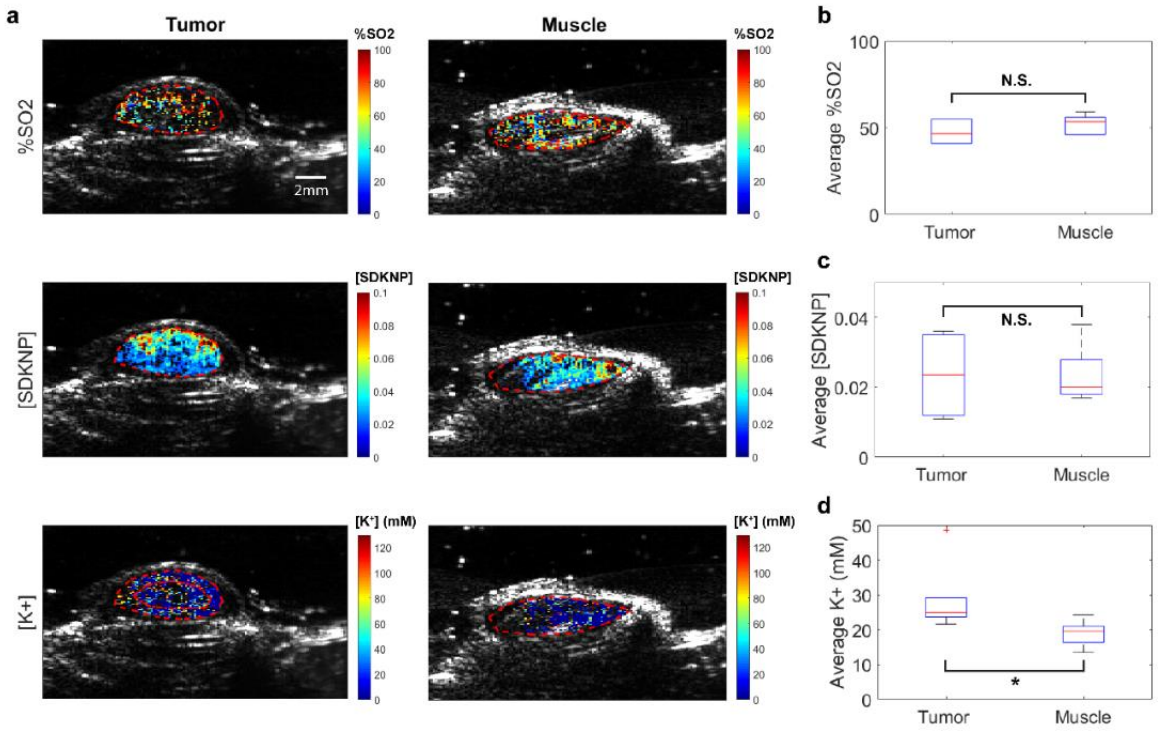

Figure 5.4 *In vivo* PA imaging with overlaid ultrasound images of subcutaneous tumors and thigh muscles (control) in nude mice. (a) Multi-wavelength unmixing performed to identify the hemoglobin oxygenation saturation (%SO2), SDKNP concentration ([SDKNP]), and K^+ concentration ($[K^+]$). The average value across all mice (n=6) in the tumor and the muscle for (b) %SO2, (c) [SDKNP], and (d) $[K^+]$, as determined by multi-wavelength unmixing. 'N.S.' indicates no significance, '*' indicates $p < 0.05$.

To validate the accuracy of the K^+ measurements *in vivo*, we then measured the average K^+ within the tumor via a method involving centrifugation to extract the interstitial fluid of the tumor, followed by inductively coupled plasma mass spectroscopy (ICP-MS) to measure the K^+ concentration of the extracted fluid. The centrifugation method was used by Eil *et al*. to measure the K^+ concentration of the tumor [101]. The results of the ICP measurements are compared to the PACI measurements in Figure 5.5. Figure 5.5a shows the average K^+ concentration measured by PACI vs ICP for each of the individual mouse tumors. Figure 5.5b shows a box plot of the distribution of average K^+ measurements for PA imaging and ICP. Here, the mean value of K^+ measured using PACI was 29 mM (range of 22-49 mM), identical to the ICP value of 29 mM (range of 15-

48 mM). Figure 5.5c shows the correlation between the average K^+ measurements made by PACI as compared to the ICP measurements. Generally, there was good agreement between the two K^+ measurements, with a correlation value of r^2=0.70.

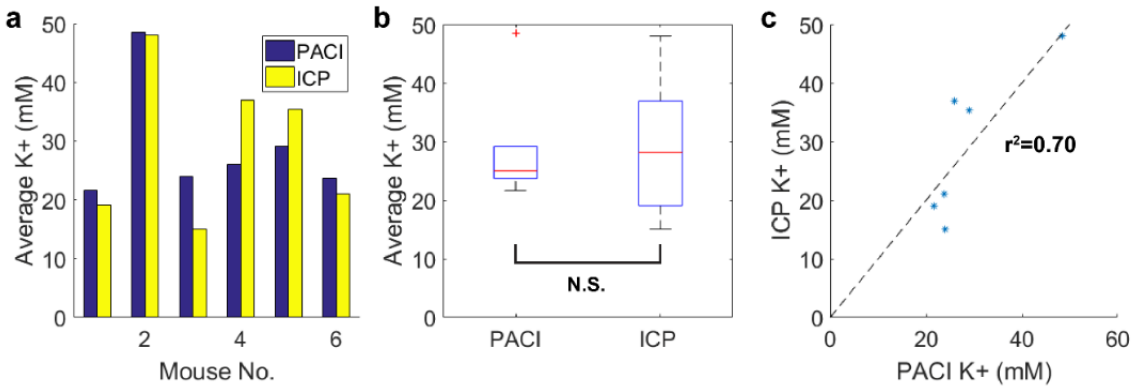

Figure 5.5 Average K^+ measurement in the tumor from PA imaging vs ICP. Average K^+ in the tumor for (a) individual mouse measurements, and (b) across all mouse samples (n=6). 'N.S.' indicates no significance. (c) Correlation analysis between the ICP and the PACI measurements.

To further analyze the capability of our PACI technology for detecting spatial information within the tumor, we analyzed the K^+ distribution within the tumor core and the periphery. As it has been reported that the necrotic core was the cause of the elevated K^+ in the tumor, we wanted to identify if there was a difference in the K^+ concentration within the tumor core (where the necrotic cores are expected), as compared to the peripheral regions of the tumor. Based on this, we would expect to see a higher K^+ concentration in the tumor core as opposed to the periphery. The results of our analysis are shown in Figure 5.6, where an example of the determined regions of interest are shown in Figure 5.6a. The cores were demarcated by taking a region of approximately 40% of the entire demarcated tumor, centered around the estimated geometric center of the tumor. Here, we noted that there was an increase in the measured K^+ concentration in the tumor core for almost all the tumors (Figure 5.6b), although this increase was small (3mM or 10%

higher). These observations suggest that elevated K^+ within tumors may not be uniform, and that this spatial difference can potentially be detected via PACI.

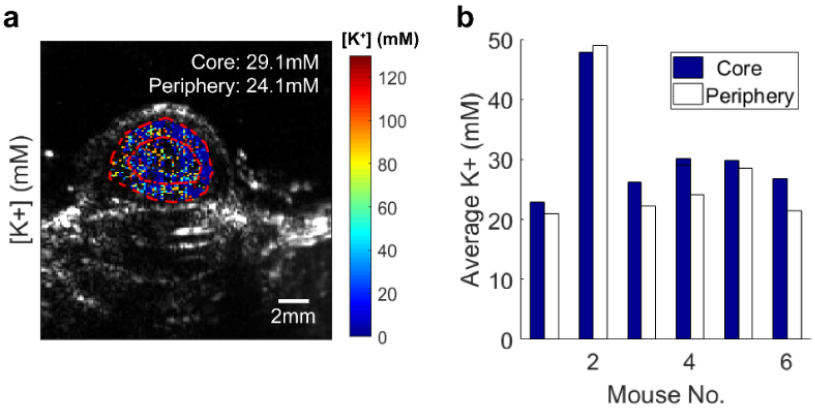

Figure 5.6 Further analysis of the measured K^+ within the tumor core vs the tumor periphery. (a) An overlaid PA and ultrasound image showing the regions of interest of the core and the periphery, outlined in red. (b) Measured K^+ concentrations for each mouse for the tumor core and the tumor periphery.

5.6 Discussion

In this study, we demonstrate the ability of PACI to measure the K^+ concentration in a tumor *in vivo*, and show the elevated K^+ concentration in the tumor compared to the muscle tissue. These results were verified using ICP-MS with good correlation between the two independent measurement techniques (r^2=0.70). While Eil *et al*. have demonstrated that TME hyperkalemia induces elevated intracellular K^+, it remains unknown at what K^+ threshold this suppressive effect manifests itself. The ability to measure K^+ concentrations *in vivo* could provide an essential tool to the field of immunology, with studies no longer having to rely on *in vitro* measurements of K^+ at single time points with no spatial resolution. Additionally, an example of the spatial distribution of the TME hyperkalemia, as measured by our PACI technique, have been provided here. While the observed tumor K^+ heterogeneity was small, this may not be the case at a

different time point of the tumor's development, especially at long times and large tumors. PACI of K^+ is ideally suited for characterizing these physiological phenomena, allowing for quantitative and spatial measurements of K^+ in an *in vivo* mouse tumor, and potentially in a patient's tumor.

There are still improvements that can be made with the K^+ measurement. Regarding the discrepancies seen in Figure 5.3, besides instrument calibration errors (UV-Vis spectrophotometer, ICP-MS), the PACI errors are mainly attributed to inaccuracies in the multi-wavelength unmixing technique, due to the wavelength-dependent light fluence attenuation in the sample, namely the "rainbow effect", and the wavelength-dependent laser energy output. While the latter is mostly corrected for by monitoring the laser energy through the partial reflector in the setup, the former is significantly more challenging to correct. A significant amount of research has been dedicated to this area, where methods to model the light fluence distribution in a tissue sample are being studied [25,26,113]. Without this wavelength-dependent light fluence correction, quantitative PA imaging is usually limited to surface/subcutaneous tumors. In a previous study, we have shown good accuracy within 6 mm depth from the tumor surface [16]. Besides light fluence modelling, increasing the number of wavelengths used in the imaging and multi-wavelength unmixing can also improve the accuracy of the measurements [23,27,28]. The latter method, however, has its own drawbacks in that the imaging time will be significantly increased, depending on the number of wavelengths desired.

Additionally, there are some concerns regarding the toxicity of the current formulation of the SDKNP. While not having significant toxicity within 2 hours, prolonged exposure does cause significant cell death in an MTT study (Figure 5.10 in Appendix 3). This toxicity is

largely attributable to the use of valinomycin as the K^+ ionophore. The toxicity of the SDKNP is the reason behind the use of a local injection rather than a targeted intravenous injection approach in this study. However, there are adjustments that can be made to the nanoparticle matrix to allow for substitution with a less toxic ionophore, such as BME-44. Notably, the Pluronic polymer is highly biocompatible and in wide medical use [114]. That being said, the strength of using these ionophore-based optical sensors is the relative ease at which sensors for other materials can be developed. For example, substituting valinomycin for a sodium ionophore allows for the development of a PA sodium sensor with relative ease. Additional substitution of ionophores and plasticizers would allow for sensing multivalent cations, such as magnesium, calcium, or transition metal ions, though non-trivial adjustments would be required, especially as the physiological concentrations of these species are much lower than that of K^+.

5.7 Conclusion

Despite its ubiquitous and abundant presence in the body, our ability to analyze K^+ concentration *in vivo* remains largely limited to the one-dimensional results gathered from electrodes. Here, we extended our previous work on PACI of tissue oxygenation and pH to include K^+. The effort utilized an exogenous contrast agent whose change in optical absorption spectrum allows for PA probing of the K^+ concentration. Our technique was verified *in vitro* and then implemented *in vivo* for measuring the concentration and characterizing the spatial distribution of K^+ within the TME. We compared the here described PACI measurement results to those initially used to describe tumor *hyperkalemia* and found good agreement between them. In summary, this work represents the first *in vivo* PA measurement of K^+ and a robust expansion of PACI.

5.8 Appendix

5.8.1 Solvatochromic Dye Characterization

The solvatochromic dye utilized by the nanosensor is synthesized in house using a protocol developed by Eric Bakker's group [109]. We report here the mass spectrum of the final product (Bakker: 559.5, Kopelman: 559.4).

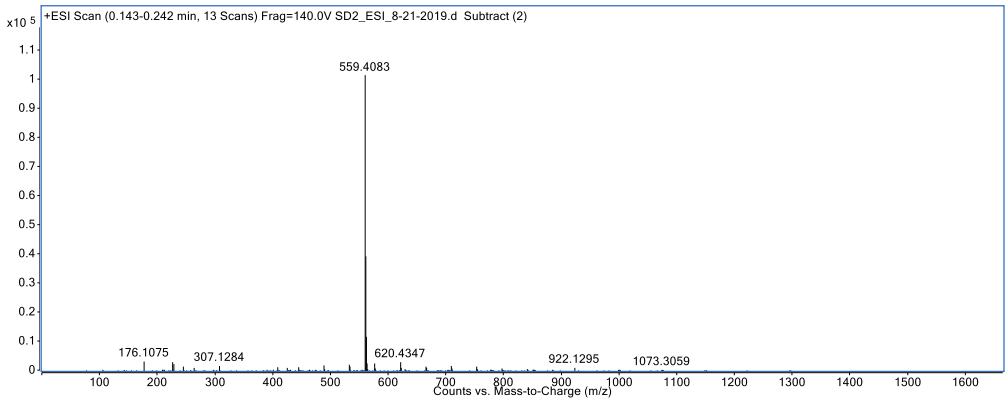

Figure 5.7 Mass spectrum of the synthesized and purified dye using the protocol described in the methods section. Measurements were made using positive ion electronspray mass spectrometry and performed by the University of Michigan's mass spectrometry core. The reported mass of the dye was 559.5Da; we measured a mass of 559.4Da.

5.8.2 Solvatochromic Dye, Potassium-sensing Nanoparticle (SDKNP) Characterization

SDKNP size was evaluated using both *Dynamic Light Scattering* (Figure 8) and *Transmission Electron Microscopy* (Figure 9). DLS measurements are seen in Figure 8, where we observed an average nanosensor diameter of **90nm** with a *polydispersity index* (PDI) of **0.107**. *Zeta potential* (ζ) measurements indicated that the SDKNP is highly stable, with a ζ of **-69.0mV**.

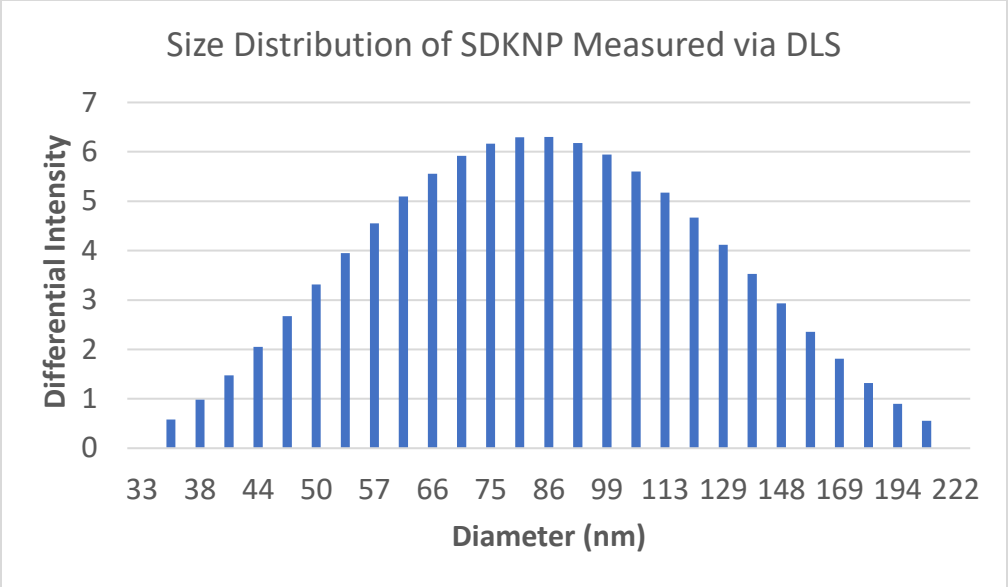

Figure 5.8 Dynamic Light Scattering measurements of SDKNP diameter. The average nanosensor size is 90nm, with a PDI of 0.107.

TEM measurements of nanoparticle diameter yielded an average diameter of 45nm. DLS values are often larger than those measured by TEM, and the discrepancies are attributed to variations in particle swelling as a result in changes of water content during sample preparation.

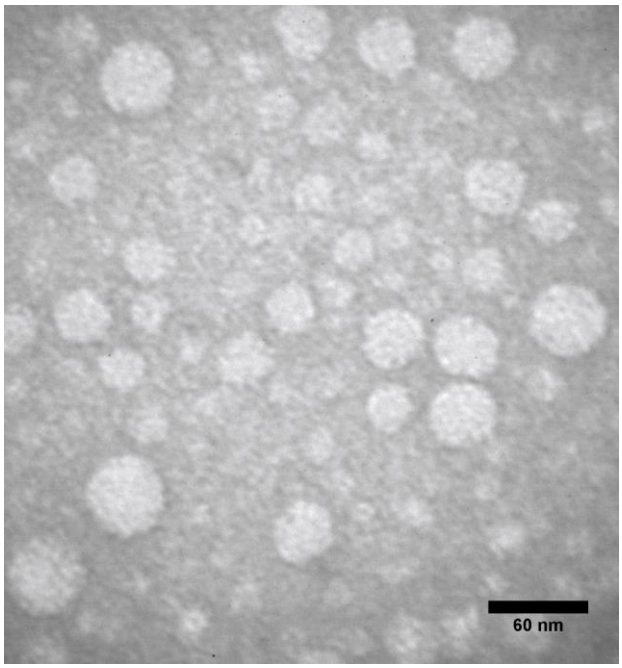

Figure 5.9 TEM images of the SDKNP taken at 5mg/mL in water. An average diameter of approximately 50nm is observed.

5.8.3 SDKNP Toxicity

An MTT assay, using SDKNP at 1 mg/mL, found that the toxicity of the nanosensor increased overtime, though little toxicity was observed in the first two hours (Figure 10). The increase in toxicity is likely attributable to degradation of the micelle and subsequent release of valinomycin, whose toxic properties are well known.

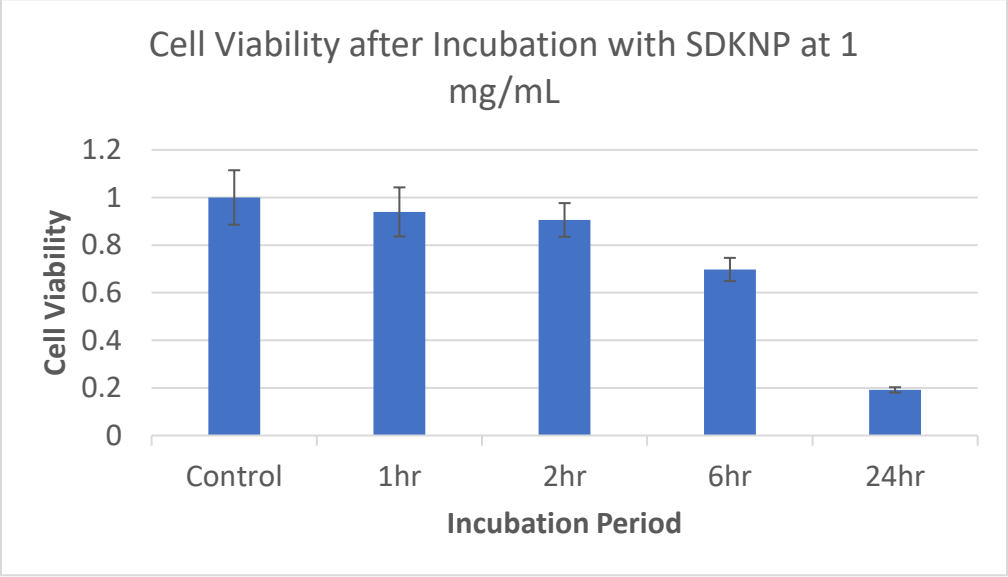

Figure 5.10 Results of an MTT assay evaluating the toxicity of the SDKNP. We observe limited toxicity over the first two hours of incubation, but prolonged exposure results in significant cell death. Error bars represent the standard deviation of 4 measurements.

CHAPTER 6

Conclusion and Future Work

The work in this thesis has demonstrated some of the applications of nanoparticle-enabled PA imaging especially in the field of *in vivo* cancer imaging. While certainly broad in their potential applications, the work in this thesis has focused on the role of nanoparticles for contrast enhancement and molecular imaging in *in vivo* cancer models using PA imaging.

Chapter 3 demonstrated an application for PA contrast enhancement using phosphorescence capable contrast agents that relies on the transient triplet differential signal from these contrast agents. Here, the potential use of the TTD technology was demonstrated for contrast enhancement in cancer detection. In addition, the study also briefly mentions the current use of this technology in oxygenation measurements *in vivo*. However, this technology is not limited to use as a tool in these two areas but has potential widespread uses in any application that uses these contrast agents. For example, methylene blue (the contrast agent used in this study), is a commonly used contrast agent in sentinel lymph node detection [115,116], and as a photosensitizing agent in photodynamic therapy [36,117,118]. In the former case, most PA imaging approaches to sentinel lymph node detection rely on single wavelength imaging, meaning that PA imaging is conducted at the wavelength of the absorption peak of methylene blue. As demonstrated in this study, this approach results in an up to 10x lower detection sensitivity compared to the TTD

method. Hence, using the TTD method for detection of sentinel lymph nodes using methylene blue could further improve its efficacy. In the latter case of PDT, the TTD method could help to identify and localize the presence of the methylene blue agent in the tumor. By first conducting TTD imaging before PDT treatment, peak accumulation of the methylene blue in the tumor can be identified before treatment, potentially allowing for a superior treatment outcome. As such, future work could involve exploring the use of the TTD method in improving both improving the sentinel lymph node detection and PDT treatment technologies. In addition, the development of new and novel TTD contrast agents can be developed as well. Factors such as the triplet state lifetime, intersystem crossing quantum yield, and pump/probe laser wavelengths are all important factors that can be explored and considered in the development and discovery of novel TTD agents.

Chapter 4 demonstrated the use of a repurposed FDA-approved drug called clofazimine for prostate cancer detection using PA imaging. The field of drug repurposing is an important one as researchers and companies seek to use well-studied drugs with known side-effects and apply them in areas outside of their initial intended use. This process can potentially save millions of dollars and years of time as much of the work of characterizing the drug has already been completed [119]. In this study, we used a nanoparticle formulation of clofazimine and showed that an intravenous injection of these nanoparticles will result in a much larger accumulation in cancerous prostates compared to normal prostates. Being a strongly pigmented nanoparticle, clofazimine generates a strong PA signal and can be used to distinguish cancerous prostates from normal prostates, at least in an *ex vivo* imaging setting. Future work would include testing this method *in vivo*. One of the main challenges that comes with *in vivo* imaging of prostate cancer is the relatively deep

imaging depth of the prostate (> 5cm). Currently, methods to bypass this imaging depth are being developed. An example of this is the use of a minimally invasive photoacoustic needle probe, that can be inserted during needle biopsy, which is a commonly performed technique for prostate cancer diagnosis. It was also previously mentioned in Chapter 4 that clofazimine specifically accumulates in macrophages, making its accumulation in tumor associated macrophages a possible tool for extending this drug for use as a contrast agent in other cancer models as well. Furthermore, it could also potentially be used to study inflammatory responses, or other responses that involve macrophage action in the body.

Chapter 5 demonstrates the use of photoacoustic chemical imaging for quantitative *in vivo* potassium imaging in the tumor microenvironment. In this study, we demonstrate the capability of PA imaging, together with a K^+ nanosensor, to quantitatively measure the K^+ concentration in the tumor microenvironment of a mouse tumor. Combined with our previous research involving pH and O_2, this can potentially allow for tri-chemical imaging of the tumor microenvironment. These three chemical parameters (pH, O_2, and K^+) are critical in cancer research due to their corresponding importance in chemo-, radio-, and immuno- therapies. These chemicals parameters have been shown to directly affect the treatment response of a tumor to these three main cancer treatments. For instance, it is well known that the less oxygen in the TME, the less effective are all radio-therapies, as all of them are based on singlet O2 and ROS formation [120-122]. It has also been shown that hypoxia can inhibit the effectiveness of certain chemo-therapeutic drugs including vincristine [123,124], melphalan [125], methotrexate [126], and cisplatin [127]. Furthermore, O2 has also been shown to affect cells of both the innate and adaptive immune system as they

are sensitive to environmental oxygen, leading to likely effects on immuno-therapy response [128-131]. Tumor acidosis, on the other hand, is well known to affect the delivery and effectiveness of a large number of chemo-therapy drugs, including paclitaxel, mitoxantrone, vincristine, and vinblastine, which all display decreased cellular uptake in the acidic TME [132-134]. In addition, it has also been shown that acidosis may negatively affect both radio-therapy [135,136] and immuno-therapy [137,138]. Lastly, K+ has been shown to have a suppressive effect on T-cell therapy, as was discussed in Chapter 5 [101,139]. Future work would involve using our photoacoustic chemical imaging technology to study the spatial distribution and concentration of these three chemical properties *in vivo*, and subsequently using it to predict and correlate the cancer treatment response of the tumor to these chemical parameters.

In summary, nanoparticle-enabled in vivo photoacoustic molecular imaging of cancer is a valuable tool that can empower cancer researchers in not only areas such as cancer detection, but also for better understanding the tumor microenvironment and predicting the outcome of a cancer treatment. Compared to other nanoparticle-enabled imaging technologies that allow for *in vivo* analysis of tumors, PA imaging has the benefit of the vast amounts of research that has gone into the generation and development of optical reporters, leading to a large library of available sensors that could be fashioned into nanoparticles that can be used to probe for specific molecular information in the body. As such, I believe that the work that I have done in this thesis has only scratched the surface that is possible in this field, with many more exciting and valuable developments that are possible and that will come in the future.

BIBLIOGRAPHY

1 Morgounova, E., Shao, Q., Hackel, B. J., Thomas, D. D. & Ashkenazi, S. Photoacoustic lifetime contrast between methylene blue monomers and selfquenched dimers as a model for duallabeled activatable probes. *Journal of Biomedical Optics* **18**, doi:10.1117/1.JBO.18.5.056004 (2013).

2 Steven, L. J. Optical properties of biological tissues: a review. *Physics in Medicine & Biology* **58**, R37 (2013).

3 Xu, M. & Wang, L. V. Photoacoustic imaging in biomedicine. *Review of Scientific Instruments* **77** (2006).

4 Beard, P. Biomedical photoacoustic imaging. *Interface Focus* **1**, 602-631, doi:10.1098/rsfs.2011.0028 (2011).

5 Wang, L. V. & Hu, S. Photoacoustic Tomography: In Vivo Imaging from Organelles to Organs. *Science* **335**, 1458-1462, doi:10.1126/science.1216210 (2012).

6 Wang, X. *et al.* Noninvasive laser-induced photoacoustic tomography for structural and functional in vivo imaging of the brain. *Nat Biotech* **21**, 803-806, doi:http://www.nature.com/nbt/journal/v21/n7/suppinfo/nbt839_S1.html (2003).

7 Hysi, E. *et al.* Photoacoustic signal characterization of cancer treatment response: Correlation with changes in tumor oxygenation. *Photoacoustics* **5**, 25-35, doi:https://doi.org/10.1016/j.pacs.2017.03.003 (2017).

8 Hu, S. & Wang, L. V. Photoacoustic imaging and characterization of the microvasculature. *J Biomed Opt* **15**, 011101, doi:10.1117/1.3281673 (2010).

9 Tzoumas, S. *et al.* Eigenspectra optoacoustic tomography achieves quantitative blood oxygenation imaging deep in tissues. *Nature Communications* **7**, 12121, doi:10.1038/ncomms12121

https://www.nature.com/articles/ncomms12121#supplementary-information (2016).

10 Tang, J., Coleman, J. E., Dai, X. & Jiang, H. Wearable 3-D Photoacoustic Tomography for Functional Brain Imaging in Behaving Rats. **6**, 25470, doi:10.1038/srep25470

https://www.nature.com/articles/srep25470#supplementary-information (2016).

11 Yao, J. *et al.* High-speed label-free functional photoacoustic microscopy of mouse brain in action. *Nature Methods* **12**, 407, doi:10.1038/nmeth.3336

https://www.nature.com/articles/nmeth.3336#supplementary-information (2015).

12 Prasad Pottumarthi, V., Edelman Robert, R. & Epstein Franklin, H. Noninvasive Evaluation of Intrarenal Oxygenation With BOLD MRI. *Circulation* **94**, 3271-3275, doi:10.1161/01.CIR.94.12.3271 (1996).

13 Xu, G. *et al.* Prostate cancer characterization by optical contrast enhanced photoacoustics. *Proc SPIE Int Soc Opt Eng* **9708** (2016).

14 Wu, D., Huang, L., Jiang, M. & Jiang, H. Contrast Agents for Photoacoustic and Thermoacoustic Imaging: A Review. *International Journal of Molecular Sciences* **15**, 23616 (2014).
15 Weber, J., Beard, P. C. & Bohndiek, S. E. Contrast agents for molecular photoacoustic imaging. *Nat Meth* **13**, 639-650, doi:10.1038/nmeth.3929 http://www.nature.com/nmeth/journal/v13/n8/abs/nmeth.3929.html#supplementary-information (2016).
16 Jo, J., Lee, C. H., Kopelman, R. & Wang, X. In vivo quantitative imaging of tumor pH by nanosonophore assisted multispectral photoacoustic imaging. *Nature Communications* **8**, 471, doi:10.1038/s41467-017-00598-1 (2017).
17 Jo, J. *et al.* In Vivo Photoacoustic Lifetime Based Oxygen Imaging with Tumor Targeted G2 Polyacrylamide Nanosonophores. *ACS Nano* **13**, 14024-14032, doi:10.1021/acsnano.9b06326 (2019).
18 Cash, K. J., Li, C., Xia, J., Wang, L. V. & Clark, H. A. Optical Drug Monitoring: Photoacoustic Imaging of Nanosensors to Monitor Therapeutic Lithium in Vivo. *ACS Nano* **9**, 1692-1698, doi:10.1021/nn5064858 (2015).
19 Shao, Q. & Ashkenazi, S. Photoacoustic lifetime imaging for direct *in vivo* tissue oxygen monitoring. *Journal of Biomedical Optics* **20** (2015).
20 Ashkenazi, S., Huang, S. W., Horvath, T., Koo, Y. E. L. & Kopelman, R. 68560D-68560D-68565.
21 Ray, A., Rajian, J. R., Lee, Y.-E. K., Wang, X. & Kopelman, R. Lifetime-based photoacoustic oxygen sensing *in vivo*. *Journal of Biomedical Optics* **17**, doi:10.1117/1.JBO.17.5.057004 (2012).
22 Shao, Q. *et al. In vivo* photoacoustic lifetime imaging of tumor hypoxia in small animals. *Journal of Biomedical Optics* **18** (2013).
23 Arabul, M. U. *et al.* Unmixing multi-spectral photoacoustic sources in human carotid plaques using non-negative independent component analysis. *Photoacoustics* **15**, 100140, doi:https://doi.org/10.1016/j.pacs.2019.100140 (2019).
24 Jurgen Glatz, N. C. D., Andreas Buehler, Daniel Razansky, and Vasilis Ntziachristos. Blind source unmixing in multi-spectral optoacoustic tomography. *Opt. Express* **19**, 3175-3184 (2011).
25 Maslov, K., Zhang, H. F. & Wang, L. V. Effects of wavelength-dependent fluence attenuation on the noninvasive photoacoustic imaging of hemoglobin oxygen saturation in subcutaneous vasculaturein vivo. *Inverse Problems* **23**, S113-S122, doi:10.1088/0266-5611/23/6/s09 (2007).
26 Daoudi, K., Hussain, A., Hondebrink, E. & Steenbergen, W. Correcting photoacoustic signals for fluence variations using acousto-optic modulation. *Opt. Express* **20**, 14117-14129, doi:10.1364/OE.20.014117 (2012).
27 Merčep, E., Deán-Ben, X. L. & Razansky, D. Imaging of blood flow and oxygen state with a multi-segment optoacoustic ultrasound array. *Photoacoustics* **10**, 48-53, doi:https://doi.org/10.1016/j.pacs.2018.04.002 (2018).
28 Luke, G. P., Nam, S. Y. & Emelianov, S. Y. Optical wavelength selection for improved spectroscopic photoacoustic imaging. *Photoacoustics* **1**, 36-42, doi:http://doi.org/10.1016/j.pacs.2013.08.001 (2013).

29 Carmichael, I. & Hug, G. L. Triplet-Triplet Absorption Spectra of Organic Molecules in Condensed Phases. *Journal of Physical Chemistry* **15** (1986).
30 Berera, R., van Grondelle, R. & Kennis, J. T. M. Ultrafast transient absorption spectroscopy: principles and application to photosynthetic systems. *Photosynthesis Research* **101**, 105-118, doi:10.1007/s11120-009-9454-y (2009).
31 Geissbuehler, M. *et al.* Triplet imaging of oxygen consumption during the contraction of a single smooth muscle cell (A7r5). *Biophys J* **98**, 339-349, doi:10.1016/j.bpj.2009.10.006 (2010).
32 Ashkenazi, S., Huang, S.-W., Horvath, T., Koo, Y.-E. L. & Kopelman, R. Photoacoustic probing of fluorophore excited state lifetime with application to oxygen sensing. *Journal of Biomedical Optics* **13** (2008).
33 Ashkenazi, S. Photoacoustic lifetime imaging of dissolved oxygen using methylene blue. *Journal of Biomedical Optics* **15**, doi:10.1117/1.3465548 (2010).
34 Forbrich, A., Shao, P., Shi, W. & Zemp, R. J. Lifetime-weighted photoacoustic imaging. *Journal of Optics* **18** (2016).
35 Geissbuehler, M., Kadlecova, Z., Klok, H. A. & Lasser, T. Assessment of transferrin recycling by Triplet Lifetime Imaging in living cells. *Biomed Opt Express* **3**, 2526-2536, doi:10.1364/BOE.3.002526 (2012).
36 Tang, W., Xu, H., Park, E. J., Philbert, M. A. & Kopelman, R. Encapsulation of methylene blue in polyacrylamide nanoparticle platforms protects its photodynamic effectiveness. *Biochemical and Biophysical Research Communications* **369**, 579-583, doi:http://dx.doi.org/10.1016/j.bbrc.2008.02.066 (2008).
37 Lee, Y.-E. K., Kopelman, R. & Smith, R. Nanoparticle PEBBLE sensors in live cells and in vivo. *Annual review of analytical chemistry (Palo Alto, Calif.)* **2**, 57-76, doi:10.1146/annurev.anchem.1.031207.112823 (2009).
38 Yoon, H. K. *et al.* Nanophotosensitizers Engineered to Generate a Tunable Mix of Reactive Oxygen Species, for Optimizing Photodynamic Therapy, Using a Microfluidic Device. *Chemistry of Materials* **26**, 1592-1600, doi:dx.doi.org/10.1021/cm403505s (2014).
39 Qin, M. *et al.* Methylene blue covalently loaded polyacrylamide nanoparticles for enhanced tumor-targeted photodynamic therapy. *Photochem Photobiol Sci* **10**, 832-841, doi:10.1039/c1pp05022b (2011).
40 Avula, U. M. R. *et al.* Cell-selective arrhythmia ablation for photomodulation of heart rhythm. *Science Translational Medicine* **7**, 311ra172 (2015).
41 Lee, C. H. *et al.* Ion-Selective Nanosensor for Photoacoustic and Fluorescence Imaging of Potassium. *Analytical Chemistry* **89**, 7943-7949, doi:10.1021/acs.analchem.7b00930 (2017).
42 Winer, I. *et al.* F3-Targeted Cisplatin-Hydrogel Nanoparticles as an Effective Therapeutic That Targets Both Murine and Human Ovarian Tumor Endothelial Cells <em>In vivo</em&gt. *Cancer Research* **70**, 8674 (2010).
43 Karamchand, L. *et al.* Modulation of hydrogel nanoparticle intracellular trafficking by multivalent surface engineering with tumor targeting peptide. *Nanoscale* **5**, 10327-10344, doi:10.1039/C3NR00908D (2013).
44 Fang, J., Nakamura, H. & Maeda, H. The EPR effect: Unique features of tumor blood vessels for drug delivery, factors involved, and limitations and

augmentation of the effect. *Advanced Drug Delivery Reviews* **63**, 136-151, doi:http://dx.doi.org/10.1016/j.addr.2010.04.009 (2011).
45 Kim, S., Chen, Y.-S., Luke, G. P. & Emelianov, S. Y. In vivo three-dimensional spectroscopic photoacoustic imaging for monitoring nanoparticle delivery. *Biomedical Optics Express* **2**, 2540-2550, doi:10.1364/BOE.2.002540 (2011).
46 Paproski, R. J., Heinmiller, A., Wachowicz, K. & Zemp, R. J. Multi-wavelength photoacoustic imaging of inducible tyrosinase reporter gene expression in xenograft tumors. *Sci Rep* **4**, 5329, doi:10.1038/srep05329 (2014).
47 Durduran, T. *et al.* Bulk optical properties of healthy female breast tissue. *Physics in Medicine & Biology* **47**, 2847 (2002).
48 Tseng, S.-H., Bargo, P., Durkin, A. & Kollias, N. Chromophore concentrations, absorption and scattering properties of human skin in-vivo. *Opt. Express* **17**, 14599-14617 (2009).
49 Sandell, J. L. & Zhu, T. C. A review of in-vivo optical properties of human tissues and its impact on PDT. *Journal of Biophotonics* **4**, 773-787 (2011).
50 Wen, X. *et al.* Fluorescence Dynamics in BSA-Protected Au25 Nanoclusters. *The Journal of Physical Chemistry C* **116**, 19032-19038, doi:10.1021/jp305902w (2012).
51 U.S. Cancer Statistics Working Group. U.S. Cancer Statistics Data Visualizations Tool, based on November 2017 submission data (1999-2015). (U.S. Department of Health and Human Services, 2018).
52 American Cancer Society. What Tests Can Detect Prostate Cancer Early? (2016). <https://www.cancer.org/cancer/prostate-cancer/early-detection/tests.html>.
53 Connolly, D. *et al.* Daily, monthly and seasonal variation in PSA levels and the association with weather parameters. *Prostate Cancer And Prostatic Diseases* **14**, 58, doi:10.1038/pcan.2010.37 (2010).
54 Eastham, J. A., Riedel, E., Scardino, P. T. & et al. Variation of serum prostate-specific antigen levels: An evaluation of year-to-year fluctuations. *JAMA* **289**, 2695-2700, doi:10.1001/jama.289.20.2695 (2003).
55 American Cancer Society. Tests for Prostate Cancer. (2017). <https://www.cancer.org/cancer/prostate-cancer/detection-diagnosis-staging/how-diagnosed.html>.
56 Hricak, H., Choyke, P. L., Eberhardt, S. C., Leibel, S. A. & Scardino, P. T. Imaging Prostate Cancer: A Multidisciplinary Perspective. *Radiology* **243**, 28-53, doi:10.1148/radiol.2431030580 (2007).
57 Fink, K. G. *et al.* Prostate cancer detection with two sets of ten-core compared with two sets of sextant biopsies. *Urology* **58**, 735-739, doi:https://doi.org/10.1016/S0090-4295(01)01352-8 (2001).
58 Applewhite Jeffrey, C., Matlaga Brian, R. & McCullough David, L. Results of the 5 Region Prostate Biopsy Method: The Repeat Biopsy Population. *Journal of Urology* **168**, 500-503, doi:10.1016/S0022-5347(05)64667-8 (2002).
59 Norberg, M. *et al.* The sextant protocol for ultrasound-guided core biopsies of the prostate underestimates the presence of cancer. *Urology* **50**, 562-566, doi:10.1016/S0090-4295(97)00306-3 (1997).

60 Epstein, J. I., Walsh, P. C., Sauvageot, J. & Ballentine Carter, H. USE OF REPEAT SEXTANT AND TRANSITION ZONE BIOPSIES FOR ASSESSING EXTENT OF PROSTATE CANCER. *The Journal of Urology* **158**, 1886-1890, doi:https://doi.org/10.1016/S0022-5347(01)64159-4 (1997).
61 Rabbani, F., Stroumbakis, N., Kava, B. R., Cookson, M. S. & Fair, W. R. INCIDENCE AND CLINICAL SIGNIFICANCE OF FALSE-NEGATIVE SEXTANT PROSTATE BIOPSIES. *The Journal of Urology* **159**, 1247-1250, doi:https://doi.org/10.1016/S0022-5347(01)63574-2 (1998).
62 Stroumbakis, N., Cookson, M. S., Reuter, V. E. & Fair, W. R. Clinical significance of repeat sextant biopsies in prostate cancer patients. *Urology* **49**, 113-118, doi:https://doi.org/10.1016/S0090-4295(97)00178-7 (1997).
63 Serefoglu, E. C. *et al.* How reliable is 12-core prostate biopsy procedure in the detection of prostate cancer? *Canadian Urological Association Journal* **7**, E293 (2013).
64 Ghai, S. & Haider, M. A. Multiparametric-MRI in diagnosis of prostate cancer. *Indian journal of urology : IJU : journal of the Urological Society of India* **31**, 194-201, doi:10.4103/0970-1591.159606 (2015).
65 Siddiqui, M. M. *et al.* Magnetic resonance imaging/ultrasound-fusion biopsy significantly upgrades prostate cancer versus systematic 12-core transrectal ultrasound biopsy. *European urology* **64**, 713-719, doi:10.1016/j.eururo.2013.05.059 (2013).
66 Alonzi, R., Padhani, A. R. & Allen, C. Dynamic contrast enhanced MRI in prostate cancer. *European Journal of Radiology* **63**, 335-350, doi:https://doi.org/10.1016/j.ejrad.2007.06.028 (2007).
67 Haider, M. A. *et al.* Combined T2-Weighted and Diffusion-Weighted MRI for Localization of Prostate Cancer. *American Journal of Roentgenology* **189**, 323-328, doi:10.2214/AJR.07.2211 (2007).
68 Huang, S. *et al.* Interstitial assessment of aggressive prostate cancer by physio-chemical photoacoustics: An ex vivo study with intact human prostates. *Medical Physics* **45**, 4125-4132, doi:10.1002/mp.13061 (2018).
69 Murashov, M. D. *et al.* Synthesis and Characterization of a Biomimetic Formulation of Clofazimine Hydrochloride Microcrystals for Parenteral Administration. *Pharmaceutics* **10**, doi:10.3390/pharmaceutics10040238 (2018).
70 Hurwitz, A. A., Foster, B. A., Allison, J. P., Greenberg, N. M. & Kwon, E. D. The TRAMP Mouse as a Model for Prostate Cancer. *Current Protocols in Immunology* **45**, 20.25.21-20.25.23, doi:10.1002/0471142735.im2005s45 (2001).
71 Cholo, M. C., Steel, H. C., Fourie, P. B., Germishuizen, W. A. & Anderson, R. Clofazimine: current status and future prospects. *J Antimicrob Chemother* **67**, 290-298, doi:10.1093/jac/dkr444 (2012).
72 Barry, V. C. *et al.* A new series of phenazines (rimino-compounds) with high antituberculosis activity. *Nature* **179**, 1013-1015 (1957).
73 World Health Organization. *Leprosy Report*, <http://www.who.int/mediacentre/factsheets/fs101/en> (2014).
74 Arbiser, J. L. & Moschella, S. L. Clofazimine: a review of its medical uses and mechanisms of action. *J Am Acad Dermatol* **32**, 241-247 (1995).

75 Tyagi, S. *et al.* Clofazimine shortens the duration of the first-line treatment regimen for experimental chemotherapy of tuberculosis. *Proc Natl Acad Sci U S A* **112**, 869-874, doi:10.1073/pnas.1416951112 (2015).
76 Lechartier, B. & Cole, S. T. Mode of Action of Clofazimine and Combination Therapy with Benzothiazinones against Mycobacterium tuberculosis. *Antimicrob Agents Chemother* **59**, 4457-4463, doi:10.1128/AAC.00395-15 (2015).
77 Williams, K. *et al.* Sterilizing activities of novel combinations lacking first- and second-line drugs in a murine model of tuberculosis. *Antimicrob Agents Chemother* **56**, 3114-3120, doi:10.1128/AAC.00384-12 (2012).
78 Dooley, K. E. *et al.* World Health Organization group 5 drugs for the treatment of drug-resistant tuberculosis: unclear efficacy or untapped potential? *J Infect Dis* **207**, 1352-1358, doi:10.1093/infdis/jis460 (2013).
79 Gopal, M., Padayatchi, N., Metcalfe, J. Z. & O'Donnell, M. R. Systematic review of clofazimine for the treatment of drug-resistant tuberculosis. *Int J Tuberc Lung Dis* **17**, 1001-1007, doi:10.5588/ijtld.12.0144 (2013).
80 Sukpanichnant, S. *et al.* Clofazimine-induced crystal-storing histiocytosis producing chronic abdominal pain in a leprosy patient. *Am J Surg Pathol* **24**, 129-135 (2000).
81 Belaube, P., Devaux, J., Pizzi, M., Boutboul, R. & Privat, Y. Small bowel deposition of crystals associated with the use of clofazimine (Lamprene) in the treatment of prurigo nodularis. *Int J Lepr Other Mycobact Dis* **51**, 328-330 (1983).
82 Baik, J., Stringer, K. A., Mane, G. & Rosania, G. R. Multiscale distribution and bioaccumulation analysis of clofazimine reveals a massive immune system-mediated xenobiotic sequestration response. *Antimicrob Agents Chemother* **57**, 1218-1230, doi:10.1128/AAC.01731-12 (2013).
83 Baik, J. & Rosania, G. R. Macrophages sequester clofazimine in an intracellular liquid crystal-like supramolecular organization. *PLoS One* **7**, e47494, doi:10.1371/journal.pone.0047494 (2012).
84 Baik, J. & Rosania, G. R. Molecular imaging of intracellular drug-membrane aggregate formation. *Mol Pharm* **8**, 1742-1749, doi:10.1021/mp200101b (2011).
85 Keswani, R. K. *et al.* Chemical Analysis of Drug Biocrystals: A Role for Counterion Transport Pathways in Intracellular Drug Disposition. *Mol Pharm* **12**, 2528-2536, doi:10.1021/acs.molpharmaceut.5b00032 (2015).
86 Yoon, G. S. *et al.* Clofazimine Biocrystal Accumulation in Macrophages Upregulates Interleukin 1 Receptor Antagonist Production To Induce a Systemic Anti-Inflammatory State. *Antimicrob Agents Chemother* **60**, 3470-3479, doi:10.1128/AAC.00265-16 (2016).
87 Yoon, G. S. *et al.* Phagocytosed Clofazimine Biocrystals Can Modulate Innate Immune Signaling by Inhibiting TNFalpha and Boosting IL-1RA Secretion. *Mol Pharm* **12**, 2517-2527, doi:10.1021/acs.molpharmaceut.5b00035 (2015).
88 Noy, R. & Pollard, J. W. Tumor-associated macrophages: from mechanisms to therapy. *Immunity* **41**, 49-61, doi:10.1016/j.immuni.2014.06.010 (2014).
89 Maolake, A. *et al.* Tumor-associated macrophages promote prostate cancer migration through activation of the CCL22-CCR4 axis. *Oncotarget* **8**, 9739-9751, doi:10.18632/oncotarget.14185 (2016).

90 Murashov, M. D. *et al.* The Physicochemical Basis of Clofazimine-Induced Skin Pigmentation. *J Invest Dermatol* **138**, 697-703, doi:10.1016/j.jid.2017.09.031 (2017).
91 Keswani, R. K. *et al.* Repositioning Clofazimine as a Macrophage-Targeting Photoacoustic Contrast Agent. **6**, 23528, doi:10.1038/srep23528

https://www.nature.com/articles/srep23528#supplementary-information (2016).
92 Rzeczycki, P. *et al.* Detecting ordered small molecule drug aggregates in live macrophages: a multi-parameter microscope image data acquisition and analysis strategy. *Biomed Opt Express* **8**, 860-872, doi:10.1364/BOE.8.000860 (2017).
93 Zhang, H. *et al.* Interstitial photoacoustic spectral analysis: instrumentation and validation. *Biomedical optics express* **8**, 1689-1697, doi:10.1364/BOE.8.001689 (2017).
94 Xu, G. *et al.* in *SPIE BiOS* Vol. 10494 (SPIE, 2018).
95 Piras, D., Grijsen, C., Schutte, P., Steenbergen, W. & Manohar, S. 4 (SPIE).
96 Sigel, A., Sigel, H., & Sigel R. K. *Interrelations between essential metal ions and human diseases*. 1 edn, (Springer).
97 Stein, W. D. The Sodium Pump in the Evolution of Animal Cells. *Philosophical Transactions: Biological Sciences* **349**, 263-269 (1995).
98 Dibrova, D. V., Galperin, M. Y., Koonin, E. V. & Mulkidjanian, A. Y. Ancient Systems of Sodium/Potassium Homeostasis as Predecessors of Membrane Bioenergetics. *Biochemistry (Mosc)* **80**, 495-516, doi:10.1134/S0006297915050016 (2015).
99 Bortner, C. D., F. M. Hughes, and J. A. Cidlowski. A Primary Role for K and Na Efflux in the Activation of Apoptosis. *Journal of Biological Chemistry* **272**, 32436-32442 (1997).
100 Mellman, I., Coukos, G. & Dranoff, G. Cancer immunotherapy comes of age. *Nature* **480**, 480, doi:10.1038/nature10673 (2011).
101 Eil, R. *et al.* Ionic immune suppression within the tumour microenvironment limits T cell effector function. *Nature* **537**, 539-543, doi:10.1038/nature19364 (2016).
102 Vodnala, S. K. *et al.* T cell stemness and dysfunction in tumors are triggered by a common mechanism. *Science* **363**, eaau0135, doi:10.1126/science.aau0135 (2019).
103 Elabyad, I. A., Kalayciyan, R., Shanbhag, N. C. & Schad, L. R. First In Vivo Potassium-39 (39K) MRI at 9.4 T Using Conventional Copper Radio Frequency Surface Coil Cooled to 77 K. *IEEE Transactions on Biomedical Engineering* **61**, 334-345, doi:10.1109/TBME.2013.2294277 (2014).
104 Augath, M., Patrick Heiler, Stefan Kirsch, and Lothar R. Schad. In vivo 39K, 23Na and 1H MR imaging using a triple resonant RF coil setup. *Journal of Magnetic Resonance* **200**, 134-136 (2009).
105 Umathum, R., Rösler, M. B. & Nagel, A. M. In Vivo 39K MR Imaging of Human Muscle and Brain. *Radiology* **269**, 569-576, doi:10.1148/radiol.13130757 (2013).
106 Wiig, H., Aukland, K. & Tenstad, O. Isolation of interstitial fluid from rat mammary tumors by a centrifugation method. *American Journal of Physiology - Heart and Circulatory Physiology* **284**, H416 (2003).
107 Xu, M. & Wang, L. Photoacoustic Imaging in Biomedicine. *Review of Scientific Instruments* **77** (2006).

108 Wang, L. V. Multiscale photoacoustic microscopy and computed tomography. *Nat Photon* **3**, 503-509 (2009).
109 Xie, X., Szilagyi, I., Zhai, J., Wang, L. & Bakker, E. Ion-Selective Optical Nanosensors Based on Solvatochromic Dyes of Different Lipophilicity: From Bulk Partitioning to Interfacial Accumulation. *ACS Sensors* **1**, 516-520, doi:10.1021/acssensors.6b00006 (2016).
110 Shortreed, M., Bakker, E. & Kopelman, R. Miniature Sodium-Selective Ion-Exchange Optode with Fluorescent pH Chromoionophores and Tunable Dynamic Range. *Analytical Chemistry* **68**, 2656-2662, doi:10.1021/ac960035a (1996).
111 Barker, S. L. R., Thorsrud, B. A. & Kopelman, R. Nitrite- and Chloride-Selective Fluorescent Nano-Optodes and in Vitro Application to Rat Conceptuses. *Analytical Chemistry* **70**, 100-104, doi:10.1021/ac970912s (1998).
112 Brasuel, M. G., Miller, T. J., Kopelman, R. & Philbert, M. A. Liquid polymer nano-PEBBLEs for Cl- analysis and biological applications. *Analyst* **128**, 1262-1267, doi:10.1039/B305254K (2003).
113 Bauer, A., Nothdurft, R., Culver, J., Erpelding, T. & Wang, L. Quantitative photoacoustic imaging: correcting for heterogeneous light fluence distributions using diffuse optical tomography. *Journal of Biomedical Optics* **16**, 096016 (2011).
114 Pitto-Barry, A. & Barry, N. P. E. Pluronic® block-copolymers in medicine: from chemical and biological versatility to rationalisation and clinical advances. *Polymer Chemistry* **5**, 3291-3297, doi:10.1039/C4PY00039K (2014).
115 Song, K. H., Stein, E. W., Margenthaler, J. A. & Wang, L. V. Noninvasive photoacoustic identification of sentinel lymph nodes containing methylene blue in vivo in a rat model. *Journal of biomedical optics* **13**, 054033-054033, doi:10.1117/1.2976427 (2008).
116 Garcia-Uribe, A. *et al.* Dual-Modality Photoacoustic and Ultrasound Imaging System for Noninvasive Sentinel Lymph Node Detection in Patients with Breast Cancer. *Scientific Reports* **5**, 15748, doi:10.1038/srep15748 (2015).
117 Hah, H. J. *et al.* Methylene Blue-Conjugated Hydrogel Nanoparticles and Tumor-Cell Targeted Photodynamic Therapy. *Macromolecular Bioscience* **11**, 90-99, doi:10.1002/mabi.201000231 (2011).
118 Tardivoa, J. P. *et al.* Methylene blue in photodynamic therapy: From basic mechanisms to clinical applications. *Photodiagnosis and Photodynamic Therapy* **2**, 175-191 (2005).
119 Pushpakom, S. *et al.* Drug repurposing: progress, challenges and recommendations. *Nature Reviews Drug Discovery* **18**, 41-58, doi:10.1038/nrd.2018.168 (2019).
120 Rockwell, S., Dobrucki, I. T., Kim, E. Y., Marrison, S. T. & Vu, V. T. Hypoxia and radiation therapy: past history, ongoing research, and future promise. *Curr Mol Med* **9**, 442-458 (2009).
121 Harrison, L. B., Chadha, M., Hill, R. J., Hu, K. & Shasha, D. Impact of tumor hypoxia and anemia on radiation therapy outcomes. *Oncologist* **7**, 492-508, doi:10.1634/theoncologist.7-6-492 (2002).

122 Horsman, M. R., Mortensen, L. S., Petersen, J. B., Busk, M. & Overgaard, J. Imaging hypoxia to improve radiotherapy outcome. *Nat Rev Clin Oncol* **9**, 674-687, doi:10.1038/nrclinonc.2012.171 (2012).
123 Teicher, B. A., Lazo, J. S. & Sartorelli, A. C. Classification of Antineoplastic Agents by their Selective Toxicities toward Oxygenated and Hypoxic Tumor Cells. *Cancer Research* **41**, 73 (1981).
124 Teicher, B. A., Holden, S. A., Al-Achi, A. & Herman, T. S. Classification of Antineoplastic Treatments by Their Differential Toxicity toward Putative Oxygenated and Hypoxic Tumor Subpopulations in Vivo in the FSaIIC Murine Fibrosarcoma. *Cancer Research* **50**, 3339 (1990).
125 Strese, S., Fryknäs, M., Larsson, R. & Gullbo, J. Effects of hypoxia on human cancer cell line chemosensitivity. *BMC Cancer* **13**, 331-331, doi:10.1186/1471-2407-13-331 (2013).
126 Wouters, A., Pauwels, B., Lardon, F. & Vermorken, J. B. Review: Implications of In Vitro Research on the Effect of Radiotherapy and Chemotherapy Under Hypoxic Conditions. *The Oncologist* **12**, 690-712 (2007).
127 Baker, A. F. *et al.* Identification of Thioredoxin-Interacting Protein 1 as a Hypoxia-Inducible Factor 1α-Induced Gene in Pancreatic Cancer. *Pancreas* **36** (2008).
128 Graham, K. & Unger, E. Overcoming tumor hypoxia as a barrier to radiotherapy, chemotherapy and immunotherapy in cancer treatment. *International journal of nanomedicine* **13**, 6049-6058, doi:10.2147/IJN.S140462 (2018).
129 Leone, R. D., Horton, M. R. & Powell, J. D. Something in the air: hyperoxic conditioning of the tumor microenvironment for enhanced immunotherapy. *Cancer Cell* **27**, 435-436, doi:10.1016/j.ccell.2015.03.014 (2015).
130 Sitkovsky, M. V. *et al.* Hostile, hypoxia-A2-adenosinergic tumor biology as the next barrier to overcome for tumor immunologists. *Cancer Immunol Res* **2**, 598-605, doi:10.1158/2326-6066.CIR-14-0075 (2014).
131 Hatfield, S. M. & Sitkovsky, M. A2A adenosine receptor antagonists to weaken the hypoxia-HIF-1α driven immunosuppression and improve immunotherapies of cancer. *Curr Opin Pharmacol* **29**, 90-96, doi:10.1016/j.coph.2016.06.009 (2016).
132 Tredan, O., Galmarini, C. M., Patel, K. & Tannock, I. F. Drug resistance and the solid tumor microenvironment. *J Natl Cancer Inst* **99**, 1441-1454, doi:10.1093/jnci/djm135 (2007).
133 Tannock, I. F. & Rotin, D. Acid pH in tumors and its potential for therapeutic exploitation. *Cancer Res* **49**, 4373-4384 (1989).
134 Gerweck, L. E., Vijayappa, S. & Kozin, S. Tumor pH controls the in vivo efficacy of weak acid and base chemotherapeutics. *Mol Cancer Ther* **5**, 1275-1279, doi:10.1158/1535-7163.MCT-06-0024 (2006).
135 Tannock, I. F. & Rotin, D. Acid pH in Tumors and Its Potential for Therapeutic Exploitation. *Cancer Research* **49**, 4373 (1989).
136 Wike-Hooley, J. L., Haveman, J. & Reinhold, H. S. The relevance of tumour pH to the treatment of malignant disease. *Radiotherapy and Oncology* **2**, 343-366, doi:https://doi.org/10.1016/S0167-8140(84)80077-8 (1984).
137 Pilon-Thomas, S. *et al.* Neutralization of Tumor Acidity Improves Antitumor Responses to Immunotherapy. *Cancer research* **76**, 1381-1390, doi:10.1158/0008-5472.CAN-15-1743 (2016).

138 Huber, V. *et al.* Cancer acidity: An ultimate frontier of tumor immune escape and a novel target of immunomodulation. *Seminars in Cancer Biology* **43**, 74-89, doi:https://doi.org/10.1016/j.semcancer.2017.03.001 (2017).
139 Vodnala, S. K. *et al.* T cell stemness and dysfunction in tumors are triggered by a common mechanism. *Science* **363**, doi:10.1126/science.aau0135 (2019).